An Experimental Determination of the Number of Gluons in a Proton using Deep Inelastic Scattering Data from the H1 Detector.

Miguel Gregori

Department of Physics, Queen Mary University of London.

A thesis submitted in accordance with the regulations for the degree of Doctor of Philosophy in the University of London.

Abstract

This thesis uses positron-proton Deep Inelastic Scattering (DIS) data from the H1 detector at the HERA collider (Hamburg). The data were analysed to study the differences between collisions in which the parton entering the hard interaction is a quark and those in which the parton is a gluon. Primarily, these differences provide a means for constraining the Parton Density Functions (PDFs). However, the analysis is taken further, and a determination of the number of gluons in the proton at the energies selected is provided, subject to some significant assumptions which will be discussed.

Contents

Chapter 1

Introduction

The analysis presented follows from earlier work on the fragmentation function. Large discrepancies were found in the low energy regime between the fragmentation function from the positron-proton (ep) data sample [1, 2] and that from earlier positron-electron (e^+e^-) experiments [3]. Since quark fragmentation universality is a sensible assumption and here taken to be correct, these differences were attributed to the different conditions of the two types of experiments. Namely, the possibility of an incident gluon and the initial state, leading order Quantum Chromo-Dynamics (QCD) processes, both present in ep interactions, but not in e^+e^-. These processes were then identified as a means to estimate the proportions of quarks and gluons in the proton.

The second and third chapters discuss the general physics and hardware aspects of the analysis. In chapter 2 an introduction to the physics background of DIS is presented, including discussions on the Quark Parton Model (QPM), Quantum Chromodynamics, and the Monte Carlo models used in this thesis. Chapter 3 describes the HERA collider and H1 detector, with

an extra section about the calibration of the SpaCal calorimeter, in which the author was involved.

The rest of the thesis describes the analysis itself, starting with chapter 4, in which the selection of the data analysed is discussed. A study of trigger efficiency is also included in this chapter. Chapter 5 contains discussions on the quality of the data sample and its modelling, and also describes the process of acceptance corrections based on Monte Carlo simulations. In chapter 6, an introduction to the Breit frame of reference in the QPM scheme is given, together with a discussion on how the leading order QCD processes mentioned above change the event topologies. A study of the systematic uncertainties that arise mainly from the measurement uncertainties themselves is included in chapter 7. Finally, chapters 8 and 9 present the results for the fraction of gluon initiated events and the number of gluons in the proton respectively, and in the last chapter the conclusions of the analysis are given.

Chapter 2

Physics Background

2.1 Deep Inelastic Scattering

When a beam of electrons (or positrons) and a beam of protons are directed towards each other, they will interact by exchanging gauge bosons. If the boson wavelength is of the order of the proton's physical size ($\sim 10^{-15}$ m), it will "see" the nucleon as a point particle and elastic scattering will take place, as described by quantum physics. The term elastic means that, although the particles will be deflected, no energy is absorbed and their intrinsic properties will remain the same, being the same particles they were before the collision. However, if the wavelength of the gauge boson is much shorter (higher momentum transfer or virtuality), it will be able to resolve the internal structure of the proton and scatter (elastically) off one of the quarks inside it, knocking it out of the nucleon and, as the theory of the strong force (QCD) describes, producing a jet of hadrons. This reaction is known as an inelastic scatter, in which the final state particles are different from those in the initial state. An illustration of DIS using real H1 data is shown in figure 2.1. The central peak in the figure represents the jet of

particles coming from the struck quark fragmentation. The cut-off at $\theta = 0$ corresponds to the beam-pipe. If there were detectors in this region another peak would be seen coming from the fragmentation of the proton remnant. The other peak at $\phi = \pi$ corresponds of course to the scattered electrons. The gluonic string between the struck quark and the proton remnant (which also produces hadrons) can also be seen.

There are two different processes that can take place, each involving different types of bosons: neutral current and charged current. In Neutral Current (NC) processes, $ep \to eX$, the exchanged bosons are the photon (γ) for an electromagnetic interaction and the Z^0 for a weak interaction, plus the quantum mechanical interference of the two. At momentum transfers smaller than the mass of the Z^0 the cross section is dominated by the single photon exchange (Born cross section), as the weak process is suppressed by a factor of the Z^0 boson mass squared, M_Z^2 ($\sim 90^2$ GeV^2), in the force propagator. In the Charged Current (CC) process, $ep \to \nu X$, the exchanged particles are the weak W^+ and W^- bosons, plus their interference. Again, these weak interactions are suppressed by a factor of M_W^2 ($\sim 80^2$ GeV^2) entering the gauge boson propagator.

The phase space studied in this thesis covers a four momentum transfer range of $12 < Q^2 < 150$ GeV^2. Thus the influence of weak interactions is negligible.

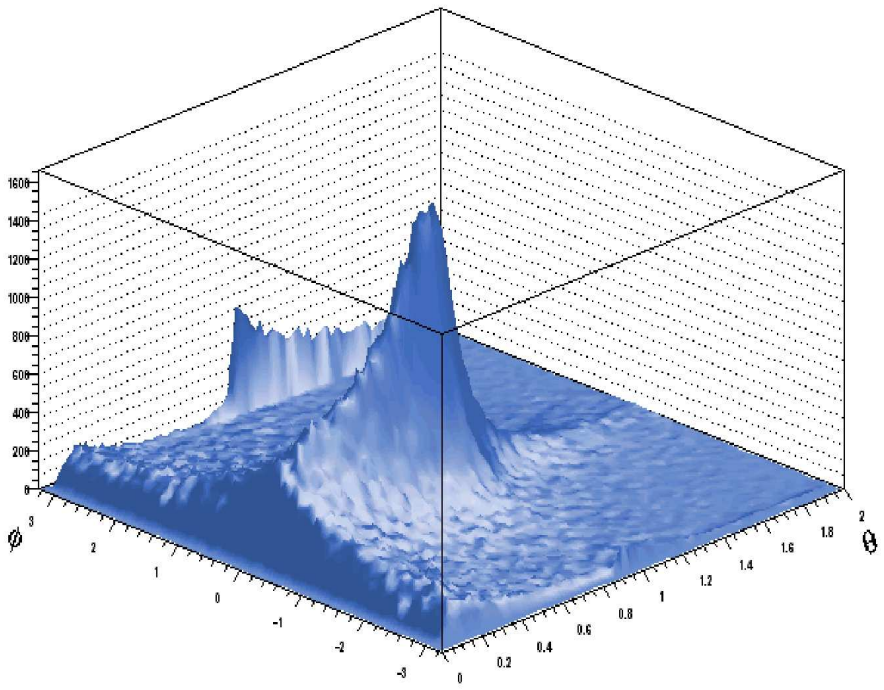

Figure 2.1: Illustration of electron-proton DIS collisions using real H1 data. For the axes labels, $\theta = \theta_t/\theta_q$, and $\phi = \phi_t - \phi_q$, where θ_t and ϕ_t are the polar and azimuthal angles of the tracks measured in the detector, and θ_q and ϕ_q are those predicted for a "real" struck quark (see equation 4.1). The vertical axis is a measure of the number of tracks.

2.2 DIS Kinematics

A diagram describing an electron-proton DIS collision is shown in figure 2.2. Its kinematics are described by two independent, Lorentz invariant quantities. The four momentum transfer square, Q^2 is

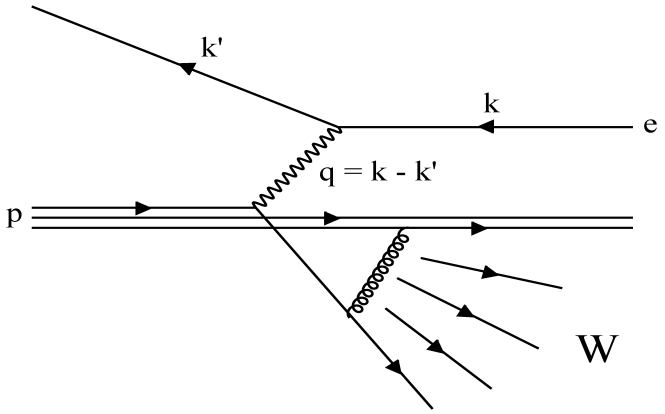

Figure 2.2: Electron-proton DIS collision. Shown are the four momentum of the incoming proton, p, the incoming (outgoing) electron, k (k'), the invariant mass of the hadronic system, W, and the momentum transfer, q.

$$Q^2 = -q^2 = -(k - k')^2 \tag{2.1}$$

were k (k') is the four momentum of the incoming (outgoing) lepton.

The second variable, known as Bjorken x (x_{Bj})[1], is defined as

$$x = \frac{Q^2}{2p(k - k')} \tag{2.2}$$

and corresponds, in the naïve Quark Parton Model (see section 2.4), to the fraction of the proton momentum carried by the struck parton. Therefore, x is a dimensionless variable in the range $\langle 0, 1 \rangle$.

The fraction of the energy transferred from the electron to the vector boson in the proton's rest frame, known as inelasticity, y, is defined as

[1]Throughout this thesis (and most of the literature) x_{Bj} is referred to as just x.

$$y = \frac{p(k-k')}{pk} \tag{2.3}$$

where p is the momentum of the incoming proton. The inelasticity is also dimensionless and limited to the range $\langle 0, 1 \rangle$.

These variables are related by the formula

$$Q^2 = Sxy \tag{2.4}$$

Where the ep centre of mass energy squared, S, is defined as

$$S = (k+p)^2. \tag{2.5}$$

Since S is a fixed quantity at HERA, two of the three variables, Q^2, y, and x, are independent. Also, neglecting the proton and electron masses, S can be written as

$$S \approx 4E_e E_p \tag{2.6}$$

where E_e (E_p) is the energy of the incoming electron (proton) beam.

Finally, another convenient Lorentz invariant variable is the total hadronic final state mass squared (or invariant mass of the boson-proton system), W, defined as

$$W^2 = (q+p)^2 \tag{2.7}$$

which gives the relation

$$W^2 = \frac{1-x}{x}Q^2 + M_p^2 \tag{2.8}$$

the latter term of which (proton mass squared) is negligible, especially at small x.

2.3 DIS Cross Section

The inclusive, neutral current DIS cross section for *ep* collisions is calculated from the tensor product

$$\sigma \sim L_{\mu\nu} W^{\mu\nu} \tag{2.9}$$

where $L_{\mu\nu}$ is the leptonic tensor well known from the theory of Quantum Electro-Dinamics (QED) [4]. Due to the proton structure, the hadronic tensor $W^{\mu\nu}$ cannot be calculated from first principles, and it is therefore expressed in terms of experimentally determined structure functions. The inclusive, double differential Neutral Current DIS cross section [5] is expressed as

$$\frac{d^2\sigma}{dxdQ^2} = \frac{2\pi\alpha^2}{Q^4 x} Y_+ \left[F_2(x,Q^2) - \frac{y^2}{Y_+} F_L(x,Q^2) \right] \tag{2.10}$$

where $Y_+ = 1 + (1-y)^2$ accounts for the spin of the incoming particles (or the angular distributions of the outgoing ones). $F_L(x,Q^2)$ and $F_2(x,Q^2)$ are known as the proton structure functions [6, 7]. The longitudinal structure function F_L is proportional to the absorption cross section of longitudinally polarised virtual photons, whereas the structure function F_2 contains contributions from both transversally and longitudinally polarised virtual photons.

These structure functions are defined as

$$F_2(x,Q^2) = \frac{Q^2}{4\pi^2\alpha}(\sigma_T(x,Q^2) + \sigma_L(x,Q^2)) \tag{2.11}$$

$$F_L(x,Q^2) = \frac{Q^2}{4\pi^2\alpha}\sigma_L(x,Q^2) \tag{2.12}$$

The ratio of the longitudinal cross section to the transverse cross section is

$$R(x,Q^2) = \frac{\sigma_L(x,Q^2)}{\sigma_T(x,Q^2)} = \frac{F_L(x,Q^2)}{F_2(x,Q^2) - F_L(x,Q^2)} \tag{2.13}$$

Since cross sections are always positive, it can be seen from equations 2.11 and 2.12 that

$$0 \leq F_L(x,Q^2) \leq F_2(x,Q^2). \tag{2.14}$$

The term in brackets in equation 2.10 is referred to as the reduced cross section,

$$\sigma_r = F_2(x,Q^2) - \frac{y^2}{Y_+}F_L(x,Q^2) \tag{2.15}$$

and it is proportional to F_2 for most of the phase space accessible in HERA. The F_L contribution is only significant at very high values of inelasticity due to the kinematic term y^2/Y_+. Also, the ratio of F_L to F_2 gives us information about the spin of the partons and their charge assignments [8].

2.4 The Quark Parton Model

The differential cross section for an elastic scattering between two point-like particles with the same charge as the electron can be written as

$$\frac{d\sigma}{dQ^2} = \frac{2\pi\alpha^2}{Q^4} Y_+ \tag{2.16}$$

where the α term at each vertex already contains a factor e^2, e being the charge of the electron. If any of the particles had a different charge by a factor of e_i there would be an additional factor of e_i^2 in the formula for the cross section.

If one of the "particles" in the interaction consists a collection of other, more fundamental particles, each sharing a fraction x of its momentum, and the probability of finding one of these component particles with a momentum fraction x in the interval $x \to x + dx$ is $f(x)dx$, the above formula becomes

$$\frac{d\sigma}{dxdQ^2} = \frac{2\pi\alpha^2}{Q^4} Y_+ f(x). \tag{2.17}$$

Note that in this expression Q is the same momentum transfer (the difference of the four momenta of the incoming and outgoing electrons), but the transfer is now to a constituent particle and not to the composite one.

Late in the 1960s Richard Feynman developed a model of the proton in which the inelastic electron-proton scattering was represented as an elastic scattering of the electron off point-like constituents within the proton, which he called partons [9]. In any frame of reference in which the partons transverse components of the momentum are much smaller than the longitudinal ones, such as the proton infinite momentum frame, these transverse

components can be neglected ($p \approx p_L$). Thus, the momentum of a parton can be defined as ϵp, where p is the momentum of the incoming proton, and ϵ a number in the range $\langle 0, 1 \rangle$ (a fraction). If we neglect the masses of the particles, then ϵ coincides with Bjorken x as introduced in the previous section. The expression 2.17 is then correct in this more general situation.

Since in a deep inelastic collision the longitudinal momenta of the particles need to be very large, the transverse components can safely be neglected for cross section calculations. The DIS cross sections can then be written as the incoherent sum of cross sections for elastic scattering of the gauge bosons off individual partons. Thus, considering deep inelastic scattering at high momentum transfers (much greater than the proton mass, $Q^2 \gg M_p^2$), and neglecting the $F_L(x, Q^2)$ contribution, the double differential cross section is

$$\frac{d^2\sigma}{dxdQ^2} = \frac{2\pi\alpha^2}{Q^4} \frac{Y_+ F_2(x, Q^2)}{x}. \tag{2.18}$$

Comparing this with equation 2.17 it is found that

$$F_2(x, Q^2) = xf(x) \tag{2.19}$$

Richard Feynman wrote the expression $F_2(x, Q^2)/x$ in terms of different parton densities $d_i(x)$, these being the probabilities of finding a parton i with momentum fraction x and fraction of electronic charge e_i within the proton. Thus,

$$\frac{F_2(x)}{x} = \sum_i e_i^2 d_i(x) \tag{2.20}$$

Similarly, if we then write $q_i(x)$ $\overline{q}_i(x)$ as the parton densities for quarks and anti-quarks respectively, we get

$$F_2(x) = \sum_i e_i^2 x[q_i(x) + \overline{q}_i(x)]. \tag{2.21}$$

Note that this means that the proton structure function is independent of the scale (Q^2) in the framework of the quark parton model, and is determined as the sum of quark densities within the proton weighted by their momentum fractions and by the square of the corresponding electric charges.

Also in the QPM framework, because of helicity and momentum conservation (and neglecting the transverse momenta of partons), longitudinally polarised photons cannot be absorbed by spin 1/2 partons, meaning that the longitudinal structure function F_L is predicted to be zero.

Another prediction of the model is that the integral over all momenta carried by charged partons within the proton must be unity,

$$\sum_i \int_0^1 x(q_i(x) + \overline{q}_i(x)) = 1, \tag{2.22}$$

with all quark species entering the summation. It was later found that the quarks themselves carry only around half of the proton momentum, implying that another electrically neutral parton species, later identified as gluons, exists within the proton, carrying the other half of its momentum.

2.5 Quantum Chromodynamics

After a SLAC-MIT collaboration experiment [10] it was found that the structure function does in fact depend logarithmically on Q^2. Scaling was found

to be violated at very low and very high values of x. It was just an opportune coincidence that the experiment which set the development of the QPM covered a phase space with x values close to 0.2, where scaling happens to be exact. These scaling violations, as well as some details of the quantum numbers of hadrons which appeared to violate the Pauli exclusion principle, plus the fact that the quarks were found to carry only half of the proton momentum, led to the development of QCD [11] as the theory of strong interactions.

2.5.1 The Running Coupling Constant

The quantum theory of electromagnetism, or Quantum Electro-Dynamics (QED), describes how the electromagnetic coupling α_{EM} varies depending on the distance an interaction is looked at. Employing a low momentum probe (long distance), the coupling looks weaker than when using a higher momentum probe. It is somewhat similar as to having an electric charge in a dielectric medium: in QED a charged particle is constantly emitting photons, which create the electric field, and these in turn are constantly producing virtual e^+e^- pair loops which act like the dielectric molecules, resulting in a vacuum polarisation that shields the bare charge of the particle. This phenomenon is known as screening.

QCD introduces a new type of charge, the colour charge, which has three degrees of freedom (red, green and blue), carried by all quarks. In the same way as QED, where the electromagnetic force is mediated by photons, in QCD the strong force is mediated by electrically neutral gauge bosons, the gluons, which, as quarks, share a fraction of the proton's momentum. The difference is that, unlike QED, QCD is a non-Abelian theory, in which the gluon carries a colour charge and can therefore couple to other gluons as

well as to itself. This implies that in QCD only neutral (colourless) objects can occur, in contrast to QED where free charged particles can exist.

The theoretical description of DIS within the QCD framework was long troubled, as the QPM assumption of quasi-free partons inside nucleons implied that the coupling strength of the interaction was very small at high momentum transfers (short distances), but very large at low momentum transfers (long distances), since no free quarks have been observed. Within QCD these phenomena are known as asymptotic freedom and quark confinement respectively, both arising from the non-Abelian nature of the theory. This results in additional diagrams in the perturbation series, such as three or four gluon vertexes, which in turn result in an anti-screening effect.

In first order QCD, the strong coupling α_s can be written as [12]

$$\alpha_s(\mu_r^2) = \frac{4\pi}{\beta_1 \ln(\mu_r^2/\Lambda_{\rm QCD}^2)} \tag{2.23}$$

where μ_r is a mass scale, known as the renormalisation scale, above which the virtual loops in the force propagator are absorbed into the coupling. These loops are known as ultraviolet (high energy) divergences. They would give rise to infinities in the perturbation expansion if a renormalisation scale were not used. The scaling factor Λ_{QCD} is of the order of 100-300 MeV, and depends on the number of active flavours, n_f, and $\beta_1 = (11 \times n_c - 2n_f)/12\pi$, where $n_c = 3$ is the number of colours. The term $-2n_f/12\pi$ is due to fermion loops and leads to screening effects as in QED. The dominating term $33/12\pi$ gives rise to the anti-screening due to gluon self interactions. Therefore the coupling falls with increasing μ_r.

QCD is asymptotically free for μ_r^2 or $Q^2 \to \infty$, which is the reason why partons confined in nucleons can be regarded as quasi-free as postulated

in the naïve Quark Parton Model. This property is characteristic of non-Abelian gauge theories. For $Q^2 \to 0$, the coupling diverges giving rise to the confinement of quarks and gluons inside hadrons. Confinement is not yet really understood, since the increase of the coupling prohibits the use of perturbation theory in the region below $Q^2 \approx 1$ GeV^2. However, a simple qualitative explanation is that the energy needed to separate two quarks a distance greater than a hadron size would be large enough for a quark-antiquark pair to be produced, and these would bind with the original quarks to produce colourless objects.

Since the parameter Λ_{QCD} depends on the number of active quark flavours, it has become customary to treat the value of the coupling α_s at an energy equivalent to the mass of the Z^0 boson ($\alpha_s(Z^0)$) as the fundamental parameter in the so-called $\overline{MS}$ (modified Minimal Subtraction) renormalisation and factorisation scheme [13].

2.5.2 Factorisation

In quantum chromodynamics cross-section infinites also arise from gluon radiation off quark lines at very low angles. These infrared (low energy) divergences are due to the peculiar behaviour of the strong coupling α_s, and are therefore absent in QED.

Because these divergences belong to the $soft$ (low momentum transfer, large distance) region of QCD they are not perturbatively tractable. However, they can be renormalised in a similar way as the ultraviolet divergences mentioned above. This is done by introducing a factorisation scale μ_f^2. For momentum transfers above this scale, $Q^2 > \mu_f^2$, α_s is taken to be small and perturbation theory is applicable. This is the $hard$ (high momentum

transfer, short distance) region of QCD.

Processes in the soft region ($Q^2 < \mu_f^2$) are absorbed in the renormalised parton density functions, which now depend on the factorisation scale, $f(x) \rightarrow f(x, \mu_f^2)$. The separation of hard and soft processes is known as factorisation, as it is presumed to be interaction independent.

2.5.3 F_2 in Leading Order QCD

In Next to Leading Order (NLO) DIS, i.e., Leading Order (LO) QCD, the relation between the observable structure function F_2 and the parton distributions f_i takes the form [14]

$$F_2(x, Q^2) = \sum_q e_q^2 x f_q(x, Q^2) + \alpha_s(Q^2) \sum_{i=q,g} x \int_x^1 \frac{dz}{z} c_i(z) f_i\Big(\frac{x}{z}, Q^2\Big) \quad (2.24)$$

where the first term is the leading order QED "tree diagram" (0^{th} order QCD) introduced above. The second term represents the leading order QCD processes. These are initial and final state Compton QCD (CQCD) and boson gluon fusion (BGF). In CQCD a gluon is radiated from the initial (ICQCD) or final (FCQCD) state struck quark, whereas in BGF an incident gluon splits into a $q\overline{q}$ pair, one of these being struck by the boson (see figure 6.17). This is the reason for integrating from x, the momentum of the particle that interacts with the gauge boson, to one, as this particle can only come from others with higher momenta.

Within the framework of QCD, these splittings are the cause of the scaling violations observed at low and high x [19, 20] values in the proton structure function (see figure 2.3). This can be viewed in two equivalent ways. One is

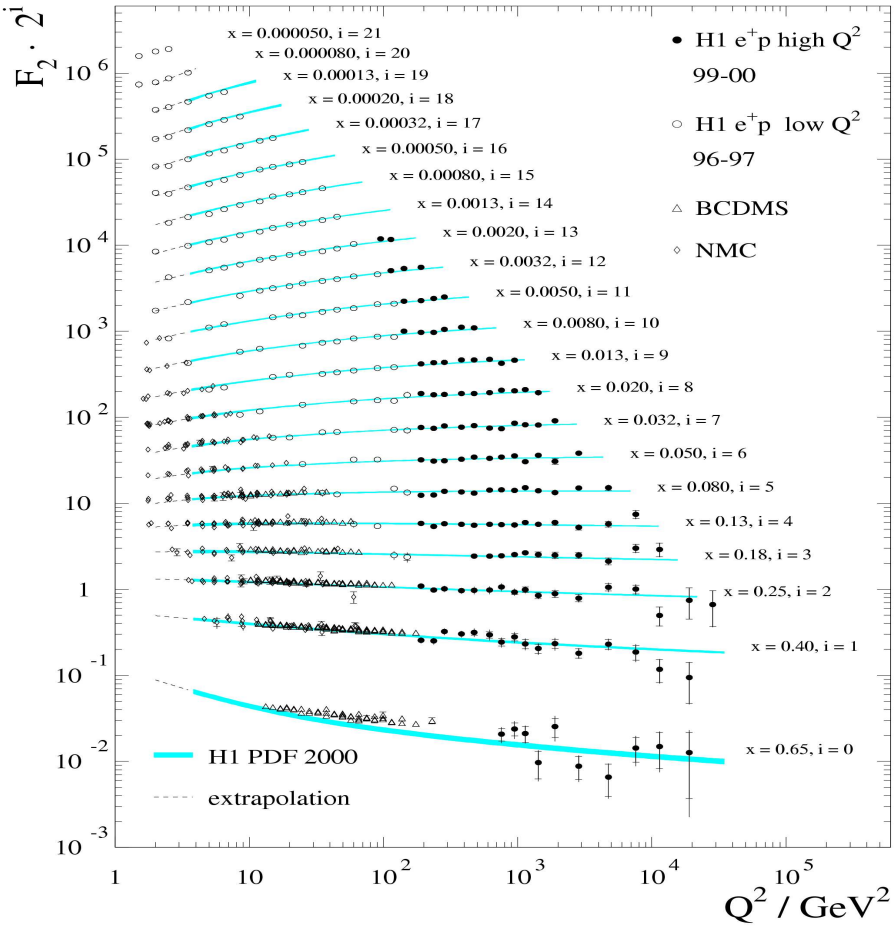

Figure 2.3: The F_2 proton structure function from (H1) high Q^2 e^+p data taken in the years 1999 and 2000 [15], along with (H1) low Q^2 e^+p data taken in the years 1996 and 1997 [16], and results from the fixed target experiments BCDMS [17] and NMC [18]. Also shown are the predictions from the H1 2000 PDF (error bands). The dashed lines are the extrapolations of the fit to $Q^2 < Q^2_{min}$.

to say that inside the proton the partons are always undergoing these QCD splittings allowed by Heisenberg uncertainty principle. This results in many partons sharing a small fraction of the proton momentum (low x), but at low Q^2 the probe is not energetic enough to resolve two low x partons coming from such QCD splittings, and "sees" them as one high x parton instead. At large enough values of Q^2 the high momentum probe can resolve the two low x partons [2].

The other way of looking at the same phenomenon is to say that the protons really consist of three valence quarks and the exchanged gluons between them, and that the energy absorbed from the collision with the electron excites these partons off their mass shell causing them to split, with a higher collision energy resulting in more splittings. These two views are equivalent, and they both result in an increase (decrease) in the number of low (high) momentum partons at large Q^2, which is the essential cause of the rise of F_2 at low x and its fall at high x.

2.6 Monte Carlo Simulations

Monte Carlo (MC) programs are used for two different purposes. The first is to correct the data taken by the H1 detector to the generated level, i.e., to correct for detector acceptance and QED radiation. The second is to get the model to predict the different results from the theory calculations it contains (kinematic distributions, PDFs, etc.). Furthermore, they also allow to select different initial state configurations, something not possible with real data. In this thesis the Monte Carlo programs were used to split

[2] This is equivalent to saying that the two partons go into the PDF as two separate particles when the factorisation scale (Q^2) is large (high resolution), and as one particle when the factorisation scale is small (low resolution).

one sample of generated events into two subsamples: one with all the quark induced events, the other with all the gluon induced events (see chapter 7).

Monte Carlo event generators of *ep* scattering consist of four main parts. First, the implementation of parton density functions of the proton, such as CTEQ [21] or MRS [22]. Second, the calculation of the Matrix Element (ME) of the hard subprocess between the exchanged vector-boson and the proton, to leading order or next to leading order QCD. Third, a parton cascade model of higher order parton emissions approximating perturbative QCD, such as the parton showers or the colour dipole model. Fourth, a model of the non-perturbative hadronisation process, such as the Lund string model. Descriptions of these models are given in the next sections.

The event generator DJANGOH13 used in this thesis simulates deep inelastic *ep* collisions including both QED and QCD radiation effects. DJANGOH contains the Monte Carlo program HERACLES [23] and an interface of HERACLES to LEPTO [24]. HERACLES simulates neutral current and charged current *ep* interactions, using parameterisations of structure functions or parton density functions, with radiative corrections. Emission of a single photon from the lepton line, self energy corrections and the complete set of one loop weak corrections can be included. LEPTO is based on Leading Order (LO) electroweak cross sections, including lepton polarisation, first order QCD matrix elements, the parton showers fragmentation model and the Lund string hadronisation model, as implemented in the program JETSET [25]. The colour dipole model of fragmentation, as implemented in the simulation program ARIADNE [26], was used to generate another set of events in order to compare the results from different parton cascade models and to study any differences they may display. Detailed studies about these generators concerning HERA *ep* interactions can be found in [27, 28].

These parton cascade models together with the hadronisation models, such as the Lund string form what is known as fragmentation. Fragmentation can be studied apart from the hard subprocess, allowing for the comparison of the fragmentation of the struck quark coming from ep interactions and of quarks created from the vacuum in e^+e^- collisions in order to test the assumption of quark fragmentation universality. The next section describes the fragmentation models of the Monte Carlo programs used in this thesis.

2.6.1 Parton Cascade Models

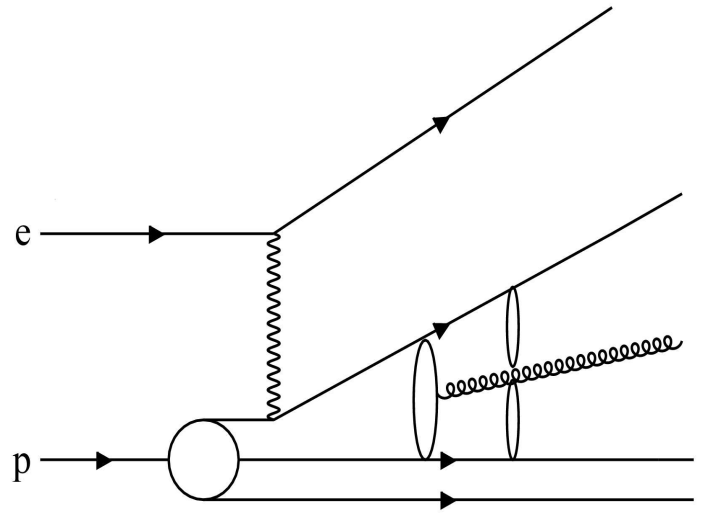

Figure 2.4: The colour dipole model for an ep DIS interaction. The colour dipole formed by the struck quark and proton remnant emits a gluon and two new dipoles are formed. These will emit gluons themselves, forming more new dipoles and so on.

The Colour Dipole Model

In the Colour Dipole Model (CDM) [29, 30], it is assumed that QCD radiation can be described by the colour dipole formed by the struck quark and the proton remnant in DIS (or by the dipoles formed by $q\bar{q}$ pairs in e^+e^-). So, instead of treating the quarks as independent sources of gluons, each pair of coloured objects is treated itself as a colour dipole emitting a gluon, which results in two new dipoles. These two dipoles radiate gluons themselves, resulting in four new dipoles and so on. In this model the emission of a gluon from a dipole is treated as being independent of other dipoles, but the effect of the radiation pattern from the dipoles, which takes into account interference, is included. This means that gluon coherence, which leads to a suppression of soft gluon emission at wide angles, is more realistically modelled in CDM than in other parton cascade models. Another requirement of the model is the successive decrease of emitted partons transverse momenta (k_t): $k_t(1) > k_t(2) > k_t(3)...$

Since in CDM emitted gluons come from colour dipoles only, there is no distinction between initial and final state gluon radiation, or in other words, all radiation is assumed to take place in the final state, which is the case in e^+e^- collisions. Electrons are treated as point-like, but in DIS the proton remnant has to be treated as an extended object. A suppression of small energy radiation from this extended object is applied, thus reducing the phase space available for radiation in the region of the target. A diagram illustrating the colour dipoles in an ep DIS collision is shown in figure 2.4.

The Parton Shower Model

In the Parton Shower (PS) model the parton cascade is described by the splitting of partons. A parent parton splits into two daughters, each splitting into two new daughters and so on. The splittings are governed by leading log Q^2 DGLAP splitting functions [31]. The possible splittings are quark to quark-gluon ($q \to qg$), gluon to quark-antiquark pair ($g \to q\overline{q}$) and gluon to two gluons ($g \to gg$). Unlike the colour dipole model, the parton showers model allows for initial and final state showers. The (first) initial state parton splits into two virtual (i.e. off-mass-shell) daughters, one ($P1$) acquiring space-like virtuality ($m^2 < 0$), the other ($P2$) acquiring time-like virtuality ($m^2 > 0$). The one entering the hard interaction with the photon is the space-like ($= transferred$) parton, $P1$, while the time-like ($= decaying$) parton, $P2$, splits into two more time-like daughters, each splitting into two new time-like partons and so the showering occurs. After the hard interaction, the initially space-like parton, $P1$, becomes time-like and goes on to produce a shower in the same way as the parton $P2$. The showering goes on until all partons are essentially on-mass-shell, at which point the hadronisation process starts. A diagram illustrating initial and final state parton showers is shown in figure 2.5.

Gluon coherence, which is approximated by the radiation pattern in the CDM, has to be imposed artificially and much more crudely in the PS model. This is done by "angular ordering", which restricts successive gluon emissions to decreasingly smaller angles. The model also imposes that the transverse momenta of emitted partons be highly ordered: $k_t(1) \gg k_t(2) \gg k_t(3)...$

The shower is terminated by an infrared cut off in transverse momentum, k_{t0},

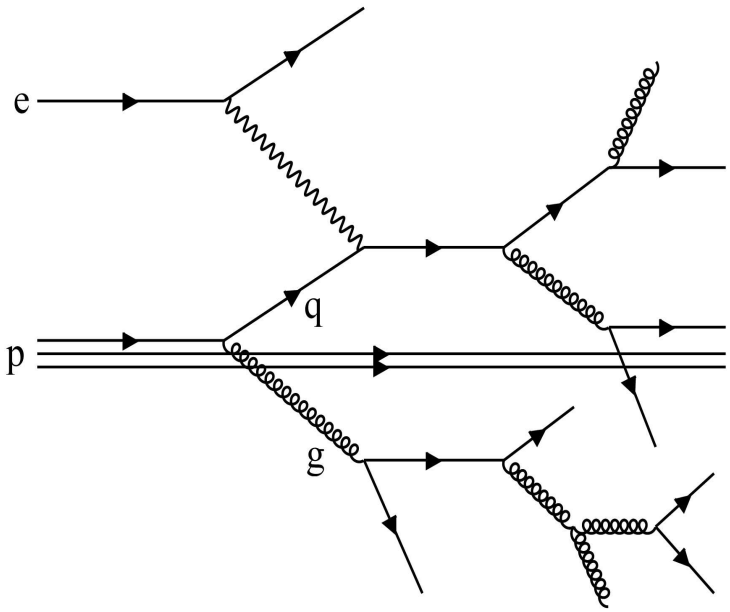

Figure 2.5: Schematic view of initial and final state parton showers in an electron-quark interaction.

below which perturbative QCD cannot be used and hadronisation models must be used. This cut off is chosen low enough to ensure that transverse momenta below it correspond to very small angles, or in other words, that the partons are essentially on-mass-shell, as mentioned above.

2.6.2 The Lund String Hadronisation Model

Hadronisation is used in the non-perturbative QCD regime, where the phenomenological parton cascades models cannot be applied due to the fact that they are not infrared safe. The Lund string hadronisation model [32] is based on the dynamics of gluonic strings which are formed due to gluon self interactions when two coloured objects are pulled apart. The coloured objects lose kinetic energy which transforms into string potential energy. When the string energy gets large enough a quark-antiquark pair is created

and so the string is split into two at a random point, then into four and so on, until the resulting partons combine to form the jet of colourless, real hadrons which are picked up in the detector. The Lund string model considers each string segment separately and thus decaying independently of other segments. The process of hadronisation as modelled with gluonic strings is shown Schematically in figure 2.6.

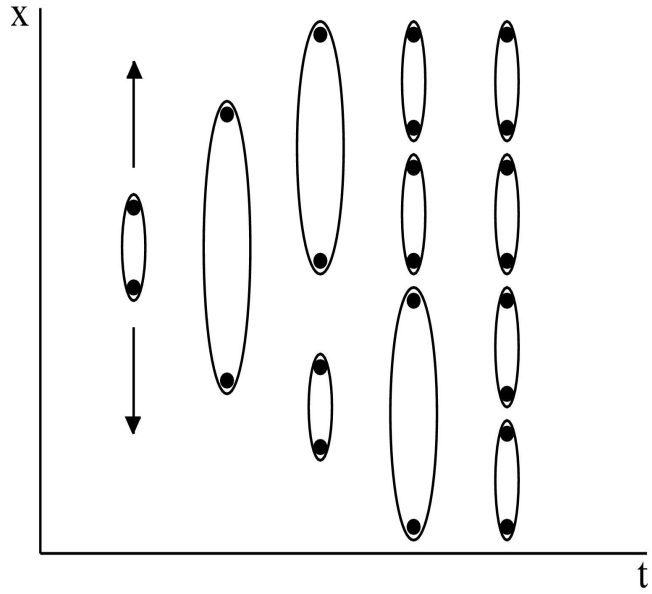

Figure 2.6: Schematic view of the Lund string hadronisation model from two coloured objects that are pulled apart.

Chapter 3

Apparatus

3.1 The HERA Collider

The Hadron Electron Ring Accelerator (HERA) consists of two separate storage rings of about 6.3 km circumference in a single tunnel at 10-25 m below ground. Since Fall 1998 protons and electrons have been accelerated to 920 GeV (previously 820) and 27.6 GeV respectively. This results in a centre-of-mass energy of $\sqrt{s} \approx \sqrt{4E_p E_e} \approx 318$ GeV.

The proton injection starts with negative hydrogen ions from the 50 MeV Proton Linac, followed by electron stripping and then acceleration in the proton synchrotron DESY III to 7.5 GeV. From there the protons are transferred via PETRA, where they are accelerated to an energy of 40 GeV, to the HERA proton storage ring. The electrons or positrons[1] are pre-accelerated first in a linear accelerator, LINAC I (220 MeV) or LINAC II (450 MeV) and at DESY II to 7.5GeV. The particles are then accelerated in PETRA to an energy of 14 GeV and then injected into the HERA electron storage

[1] HERA can run with both electrons or positrons. Both will be referred to as electrons in this thesis.

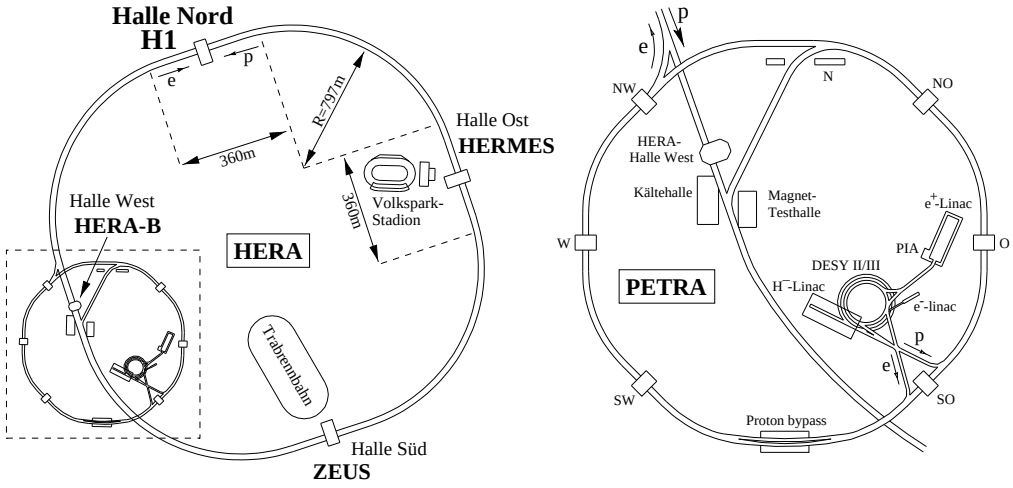

Figure 3.1: The HERA collider (left) and its pre-accelerators (right).

ring. The HERA collider is depicted in figure 3.1.

Once injected into HERA the two beams circulate in opposite directions. The electron machine is operated with normal conducting magnets whereas the proton one uses superconducting magnets. At two interaction points the particle beams are directed against each other and collisions between the protons and electrons take place. The reaction products are measured by the large general purpose detectors H1 and ZEUS. Additionally there are two fixed target experiments: HERA-B and HERMES. In the HERA-B experiment proton-nucleon scattering is investigated by inserting wire targets of various materials in the proton beam tail. The HERMES experiment studies the spin structure of nucleons by colliding longitudinally polarised electrons on various gaseous targets of polarised atoms.

Protons and electrons are stored in approximately 175 bunches of $10^{10} - 10^{11}$ particles each, leading to typical currents of 90 mA for protons and 35 mA for electrons. The bunch crossing rate at the interaction points is around

10.4 MHz or a bunch crossing every 96 ns. An average value for the specific luminosity of $0.6{\cdot}10^{30}\mathrm{cm}^{-2}\mathrm{sec}^{-1}\mathrm{mA}^{-2}$ is reached. Unmatched proton and electron "pilot" bunches are also injected for luminosity studies.

3.2 The H1 Detector

The H1 detector is situated in the northern part of the HERA ring (figure 3.1), and was designed as an almost hermetic general purpose detector to measure cross sections and final states for a broad spectrum of ep reactions. The H1 coordinate system is defined as a right-handed system with origin at the nominal interaction point. The positive z-axis points towards the proton beam direction of motion, referred to as the forward direction. The positive y-axis points in the upward direction and the positive x-axis to the centre of the collider. Polar angles θ are measured from the positive z direction and azimuthal angles ϕ from the positive x direction. A complete description of the H1 detector can be found in [33].

The detector is cylindrically symmetric around the beam axis. Because of the imbalance in the energies of the colliding beams the ep centre-of-mass system is moving along the proton beam direction relative to the laboratory frame of reference. This results in a collimation of the final state particles in the forward direction, so H1 was designed with an enhanced instrumentation in this region. The detector is depicted in figure 3.2 with a list of its components. A more detailed side view of the detector is shown in figure 3.3

To identify neutral current, $ep \to eX$, or charged current, $ep \to \nu X$, reactions it is necessary to identify the scattered lepton amongst the rest of the event and to measure its momentum. Electrons can be directly detected with tracking devices and are very easy to identify with high granularity

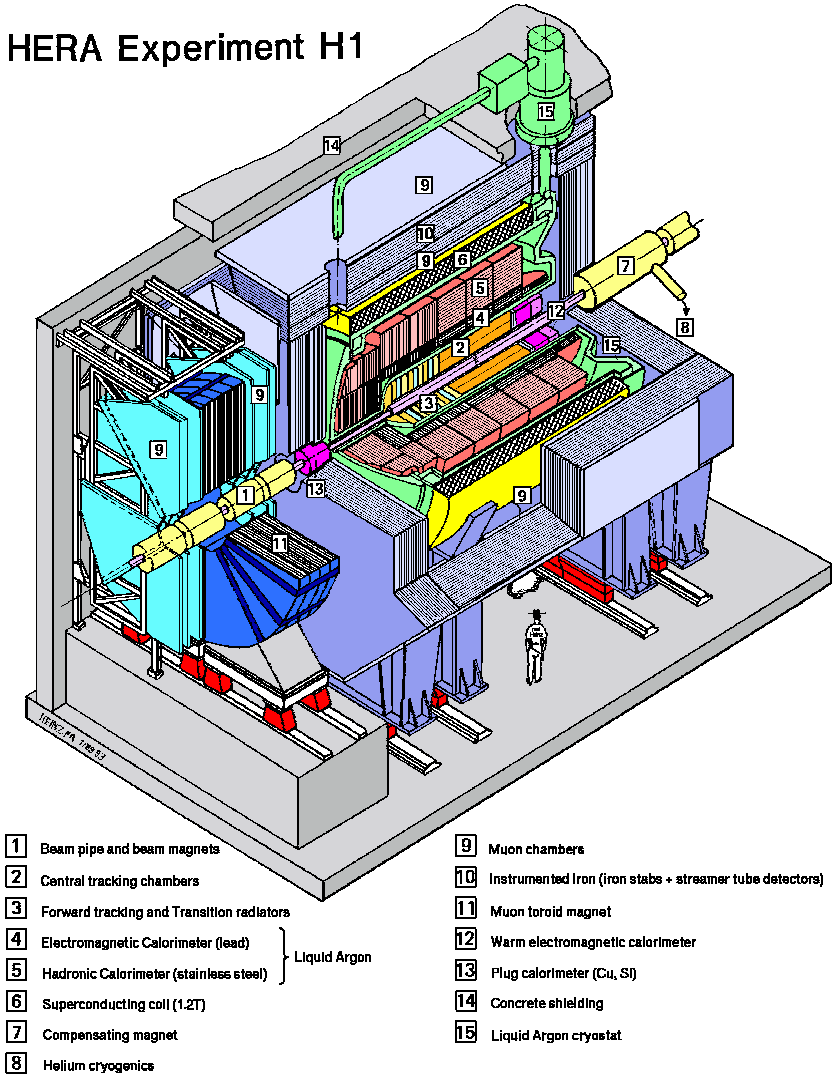

Figure 3.2: The H1 detector with its components.

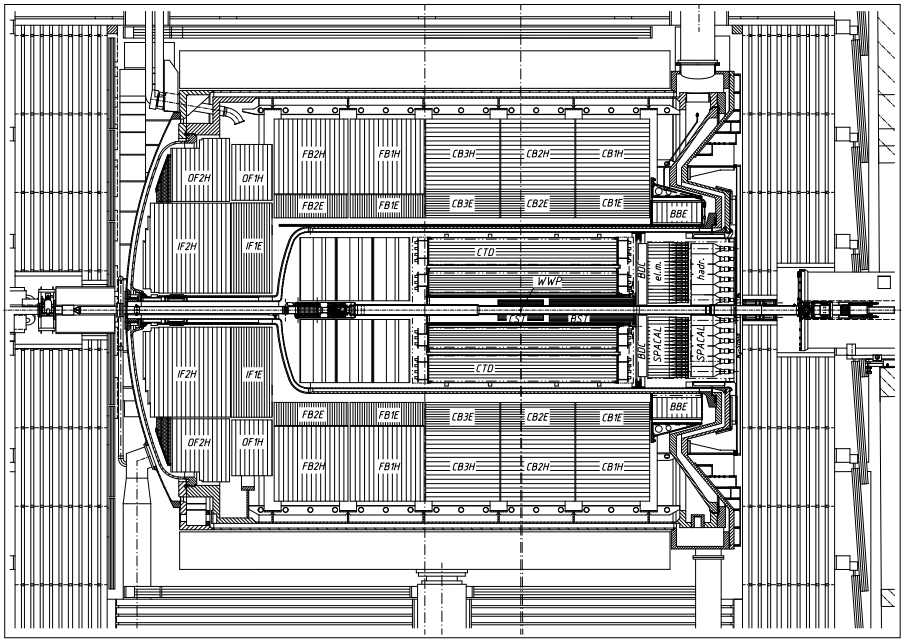

Figure 3.3: Detailed side view of the H1 detector.

calorimetry. Neutrinos however, are too weakly interacting for any general purpose apparatus to be able to detect them, but their presence can be inferred and their momenta and energies reconstructed from the missing energy in the calorimeters.

In an *ep* deep inelastic collision many hadrons are produced, mainly pions. In the optimal situation all these particles are identified and their four momenta measured by the detector. Momenta and particle identification of long-lived, charged particles can be achieved in a drift chamber by measuring tracks and their differential energy loss dE/dx. But trackers have two disadvantages: they are unable to detect neutral particles and their momentum resolution decreases for increasing momenta. Both issues are addressed when the tracker information is complemented by electromagnetic and hadronic calorimetry.

To calculate the cross section for a given process from an observed number of events it is necessary to determine the luminosity at the interaction point. This is best done by measuring the event rate from a reference reaction with a well known cross section. The Bethe-Heitler process [34], $ep \to ep\gamma$, is the reference reaction for HERA.

Most of the reactions within the H1 acceptance come from background processes. The main source of background comes from collisions between protons from the beam and nucleons from molecules of the remaining gas in the evacuated beam pipe (beam-gas interactions), and also between off-momentum protons from the beam and the actual beam pipe (beam-wall interactions). The rate of these background processes is about 10^4 times higher than the rate of genuine ep collisions, so H1 uses a multi-level trigger system to reject background and record only the information from the physics processes one wishes to study.

3.2.1 The Time of Flight System

The Time of Flight system (ToF) [35] consists of several scintillators placed in the end caps of the return yoke and in the forward region close to the beam pipe. The SpaCal calorimeter also contributes to the time of flight information. The role of this system is to reject background coming from beam-wall and beam-gas interactions taking place outside of the detector and almost coincident with the beam. Particles from such processes have a different time of arrival than those returning from the interaction point. The information from the scintillators combined with the information from the HERA clock, which is based on the bunch crossing frequency of the beams, provide an accurate estimate of particle flight times. Background events are rejected according to this estimate.

3.2.2 The Luminosity System

The luminosity is a defined as the observed number of events of a given process divided by the cross section for that process, having therefore dimensions of inverse area. The above mentioned Bethe-Heitler process is used as a reference to determine the luminosity taking into account the detector acceptance. Events coming from BH processes are detected by the coincidence of a photon and an electron in the luminosity system [36]. A general view of the system is shown in figure 3.4. It consists of two electromagnetic calorimeters: the Electron Tagger (ET), which contains 49 square cells with a total area of 154×154 mm^2 and an angular acceptance of approximately 5 mrad, and the Photon Detector (PD), which contains 25 square cells and has an area of 100×100 mm^2 and an angular acceptance of about 0.45 mrad.

Scattered electrons with energies between 10 and 20 GeV are deflected by the beam optics, then pass an exit window situated at z = -27.3 m and hit the electron tagger. Photons exit the proton beam pipe through a window situated at z = -92.3 m, where the beam pipe bends upwards, and hit the photon detector.

3.2.3 The Triggering System

The H1 trigger system is used to have a fast separation of the background events from the interesting physics reactions one wishes to study, and it is divided into four levels. Within 2.3 μs, the Level 1 (L1) trigger [37] makes a decision on whether to accept or not an event using information provided by the different Level 1 Trigger Elements (L1 TEs). The Central Trigger Logic (CTL) combines these into 128 sub-triggers (STs). Since not all sub-detectors can provide the required information fast enough for the

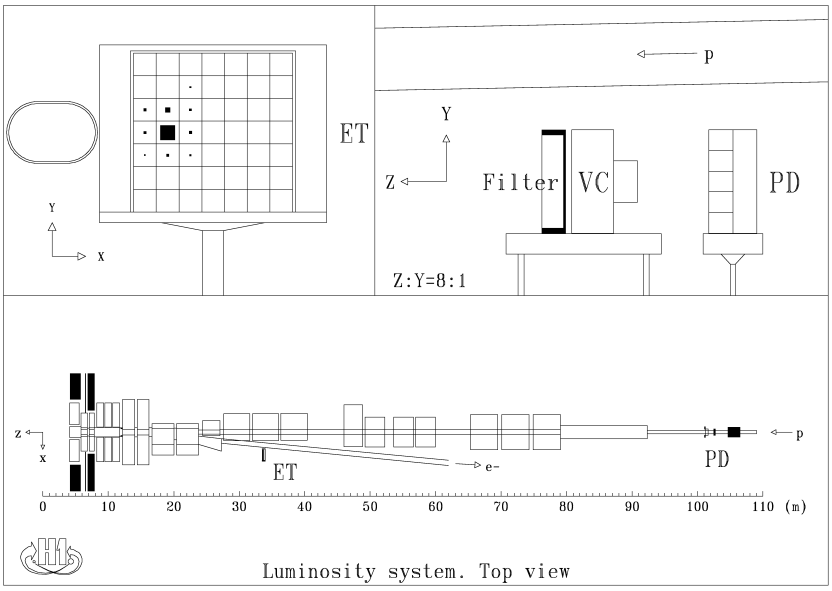

Figure 3.4: Luminosity system.

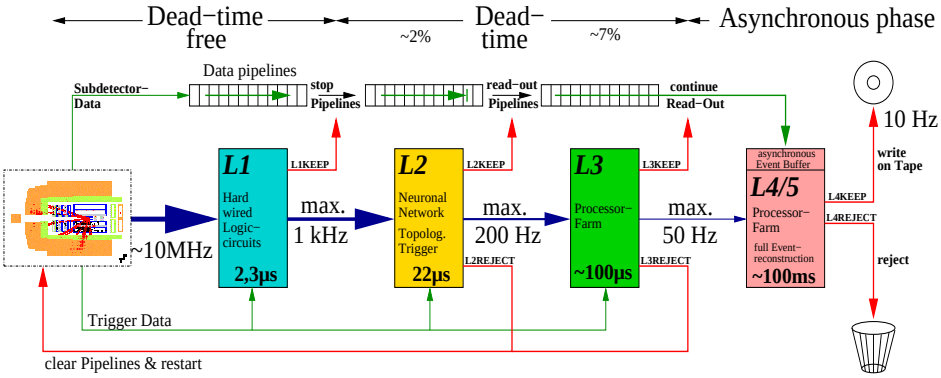

Figure 3.5: The trigger system in H1. Displayed here is the never implemented trigger level 3. The actual output of the second level is therefore 50 Hz.

L1 trigger to make a decision within the time scale of each bunch crossing, this information is put into pipelines where it is kept until all sub-detectors have provided their trigger elements. After 2 μs (or 24 bunch crossings), the trigger elements are linked logically and the L1 decision is made. If any sub-trigger condition is fulfilled by an event, the pipeline is stopped and the signal is passed to the second trigger level.

The trigger Level 2 (L2) makes a more complex decision than the L1 and takes 20 μs. It uses two independent trigger systems: topological triggers [38] and neural networks [39], both providing a decision in the form of L2 sub-triggers. A list of L1 sub-triggers is assigned to each L2 sub-trigger, which need to fire in coincidence, thus validating the L1 sub-triggers. A possible third level trigger has never been implemented.

On Level 4 all the information from the detector is available, and it is stored in a buffer with enough capacity for 30 events. These are processed off-line in parallel by PowerPC computers and thus the processing time does not contribute to the dead-time of the detector. These PowerPCs reconstruct the events and recalculate the decisions of the previous levels. The events are classified according to their physics properties and written into Data Storage Tapes (DST). Unclassified events are rejected except for 1 in every 100, which is kept for monitoring purposes. The trigger system is shown in figure 3.5. There are also some random triggers in H1 for monitoring purposes.

3.2.4 Tracking in H1

The H1 tracking system is used for track reconstruction, momentum measurement, particle identification and vertex determination. It covers a wide

range of polar angles, approximately between 5^o and 178^o, and the complete range of azimuthal angles. A superconducting solenoid encloses both the tracking and calorimetry systems and produces a uniform magnetic field of 1.15 T parallel to the beam axis.

The interaction point is surrounded by the Central Silicon Tracker (CST) [40], a vertex detector consisting of two layers of semi-conductor strip detectors. It covers a polar angle range between 30^o and 150^o, and provides track measurement in two projections by having perpendicular readout strips on both sides of the detector. It provides hit resolutions of 12 μm in $r - \phi$ and 25 μm in z. In the backward region a second vertex detector, the Backward Silicon Tracker (BST) [41], covers a polar angle range between 162^o and 176^o. The CST and the BST considerably improve track reconstruction and allow determination of secondary vertices close to the primary vertex due to their high spatial resolution.

These silicon trackers are themselves surrounded by the Central Track Detector (CTD), see figure 3.6, whose main components are two cylindrical drift chambers, the Central Jet Chambers 1 and 2 (CJC1 and CJC2) [42], with wires parallel to the beam axis. Their design followed closely that of the jet chambers of the JADE experiment at PETRA [43]. The CJC1 and CJC2 cover a z range of $-1.5\text{m} < z < 2.0\text{m}$, and measure transverse momenta of charged particles with a resolution of $\delta p_t/p_t < 0.01 \cdot p_t/\text{GeV}$. Particle identification is provided by measuring the particle-specific energy loss dE/dx. The CJC1 is surrounded by two drift chambers, one next to the inner side of the CJC1, the Central Inner Z chamber (CIZ), and one next to the outer side, the Central Outer Z chamber (COZ), whose wires are perpendicular to the beam axis and thus provide an improved measurement of the z coordinate of the interaction vertex, with a resolution of approximately 300

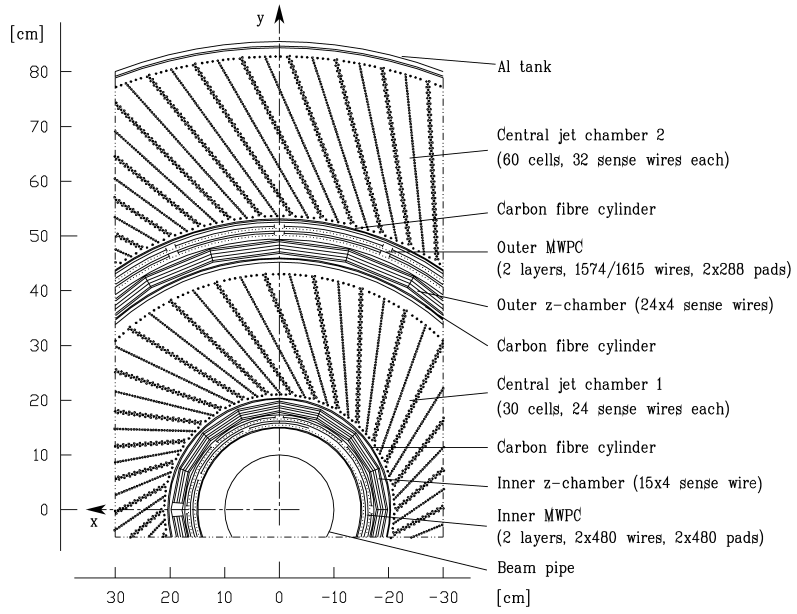

Figure 3.6: Front view of the central tracking system in the H1 detector.

μm. Next to the z chambers there are two multi-wire proportional chambers, the Central Inner Proportional chamber (CIP), next to CIZ, and the Central Outer Proportional chamber (COP), next to COZ. These provide a fast trigger signal due to their good timing resolution, and also due to the good vertex resolution in the z direction.

In the forward direction the Forward Track Detector (FTD) [44] provides track Reconstruction. It covers a polar angle range between 5^o and 25^o and consists of three identical super-modules placed around the z axis. Each super-module includes three different orientations of planar wire drift chambers which provide a good θ measurement, a multi-wire proportional chamber for fast triggering, a transition radiation detector and a radial wire drift chamber which provides a good $r-\phi$ measurement. A side view of the whole tracking system of H1 is shown in figure 3.7.

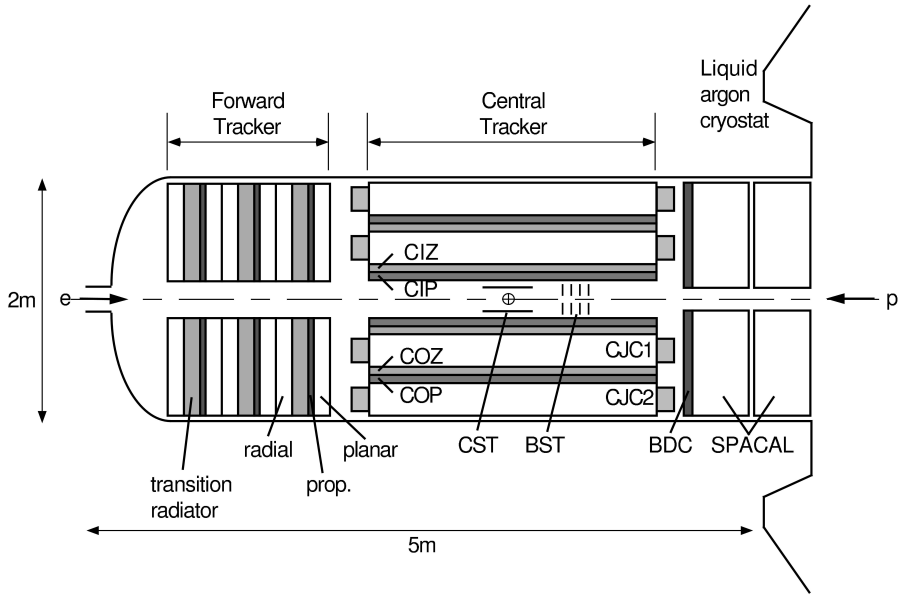

Figure 3.7: Side view of the tracking system in the H1 detector.

In the central region, the instrumented iron yoke is used for muon track detection (see figure 3.2). It consists of limited streamer tubes embedded in the iron yoke of the solenoid. A forward muon system is situated after the return yoke and covers a polar angle range between 3^o and 17^o. It comprises six drift chambers, three on each side of the muon toroid magnet. The chambers are divided in two groups, one group of four for polar angle measurement, and one group of two for azimuthal angle measurement.

3.2.5 Calorimetry in H1

Calorimetry in H1 provides a measurement of the energies of the final state particles and is constituted of five sub-components: The Liquid Argon Calorimeter (LAr), the Spaghetti calorimeter (SpaCal), the tail catcher, the plug calorimeters and the VLQ calorimeter. The relevant calorimeters for

this analysis are the LAr and SpaCal and thus will be the ones described here. A detailed description of the other three is given in [33].

The Liquid Argon Calorimeter

The LAr calorimeter [45] covers a polar angle range between 4^o and 154^o and has a full azimuthal coverage. It is divided into two sections: the inner components of the calorimeter are used to measure electromagnetic showers and the outer ones are used for hadronic showers. The depth of the electromagnetic section corresponds to 20-30 radiation lengths X_0 (scaling variable for the probability of occurrence of Bremsstrahlung pair production), depending on the polar angle of the energy cluster. The hadronic section corresponds to 4.5-8 hadronic interaction lengths λ_0 (mean free path of a particle before undergoing a non-elastic interaction). In total the LAr calorimeter comprises 45000 cells. This ensures an extremely good spatial resolution of the energy deposited and hence accurate separate corrections for electromagnetic and hadronic energy deposits. Each cell consists of absorber plates supplemented by high voltage and readout electrodes. Liquid argon is used as sampling material between absorber plates. The absorber material is lead for the electromagnetic section and stainless steel for the hadronic one.

The LAr calorimeter is built out of eight wheels in the longitudinal direction, with each wheel divided into eight octants in the transverse plane (see figure 3.8). The wheels, from back to front, are as follows: the Backward Barrel Electromagnetic calorimeter (BBE), the three Central Barrel calorimeter modules (CB1, CB2 and CB3), the two Forward Barrel calorimeter modules (FB1 and FB2) and the Outer and Inner Forward calorimeters (OF and IF). The BBE wheel is for electromagnetic shower measurement only, and

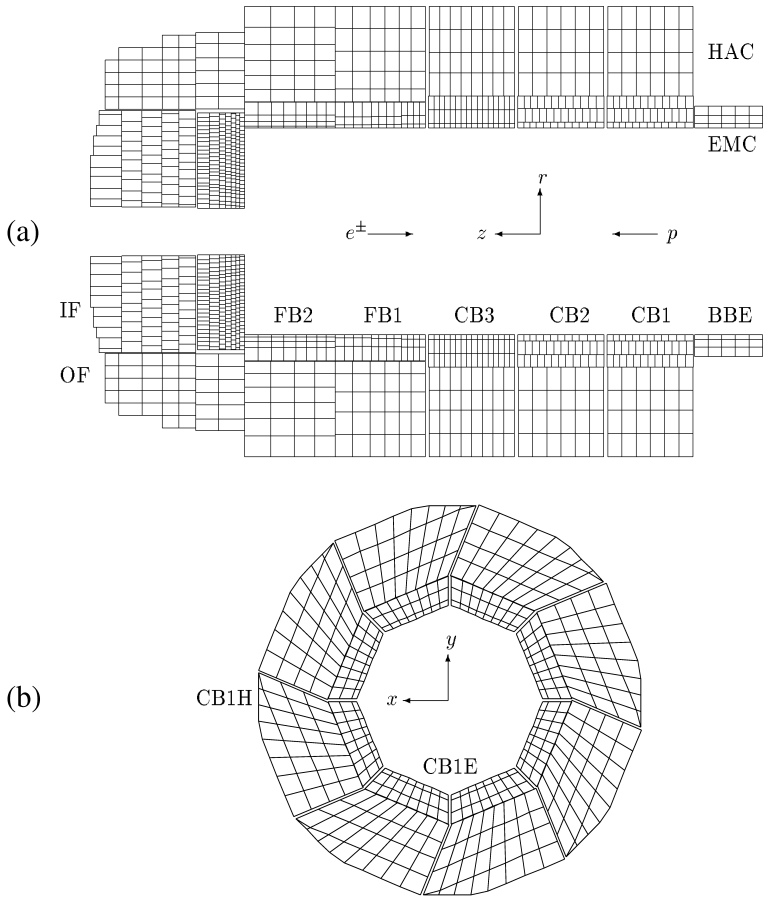

Figure 3.8: The liquid argon calorimeter; (a) is the side view showing the barrels and cell arrangement for the electromagnetic and hadronic sections. (b) is the front view showing the octants. Note the tilted cell arrangement for the hadronic section.

the OF wheel for hadronic showers only. The rest of the wheels comprise both electromagnetic and hadronic sections. Regions between modules are problematic due to high energy losses. The gaps between wheels are called z-cracks, and the ones between octants are called ϕ-cracks.

In the present analysis the LAr calorimeter is used primarily to measure the energies of the hadrons from the jets that are produced in deep inelastic scattering reactions, leaving the scattered electron energy measurement to the SpaCal.

The Spaghetti Calorimeter (SpaCal)

The SpaCal [46] is used for picking up scattered electrons at low angles (low Q^2). Like the liquid argon calorimeter, it also contains electromagnetic and hadronic sections. It is situated in the backward region of the H1 detector (see figure 3.3), with the inner electro-magnetic face at ~ -1.5 m from the middle point of the CTD, and a radial coverage which goes from 5.7 to 80 cm. This corresponds to angles from the interaction point approximately between 175° and 150°. The electro-magnetic part of the SpaCal consists of 1192 cells with an active volume of $4.05 \times 4.05 \times 25$ cm^3 each. A transverse view of the electromagnetic section of the SpaCal is given in figure 3.9.

Each cell is made of alternating lead plates and scintillating fibres with diameter of 0.5 mm. As in the LAr electromagnetic calorimeter, when an electron interacts with a lead plate from one of the cells it will lose energy by radiating energetic photons. Some of these photons will create electron-positron pairs, which in turn can emit more photons. This is the process known as electro-magnetic showering.

Here, the scintillation photons from the electrons are converted into elec-

(a) (b)

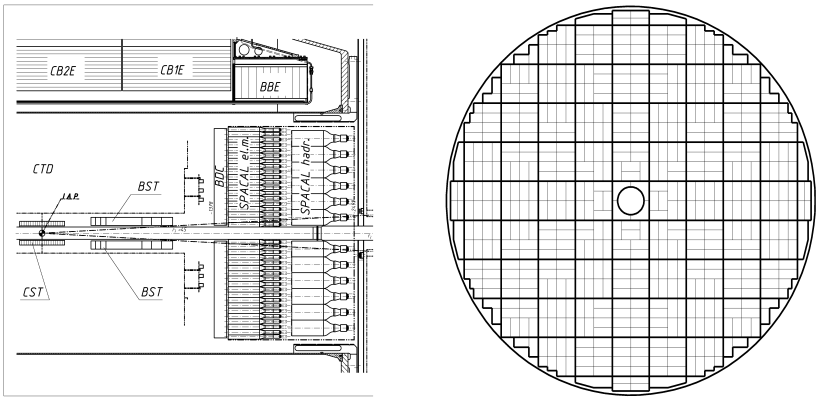

Figure 3.9: The SpaCal calorimeter; (a) is the side view which shows the electromagnetic and hadronic sections as well as some of the other components of H1. (b) is the front view (from the centre of H1) showing the cell arrangement for the electromagnetic section.

trical signals by photo-multiplier tubes (PMT). The active length of the electro-magnetic part of the SpaCal is 25 cm, corresponding to $27.47X_0$, and $1\lambda_0$). The angular coverage of the calorimeter is $153^o < \theta < 177.8^o$, corresponding to a momentum transfer squared (Q^2) range approximately from 4 to 100 GeV^2.

The main source of background in SpaCal comes from synchrotron radiation. In the process of accelerating electrons close to the speed of light in the HERA collider, they lose energy due to the magnetic fields keeping them in orbit and focusing them on the interaction point. This energy is in the form of energetic photons (X rays) known as synchrotron radiation. In principle protons also radiate in this way, but electrons suffer most from this loss, first because they are very light particles, and second because it is the electron beam that is directed towards the proton beam, being therefore subject to huge forces by the bending magnets close to the detector. It is in

these regions where the biggest source of synchrotron radiation occurs, and although there are strategically placed collimators to absorb this radiation, the beam-pipe area can not be protected. Some of the synchrotron radiation escapes the collimators, and falls in the SpaCal central region ($R_{SpaCal} <$ 16 cm), causing large background. Because of this the center of the SpaCal is known as the "hot-spot" region, and it is excluded in many analyses by applying a central box cut.

The use of photo-multipliers and an electronic chain with low noise level permits very low trigger thresholds and a reliable reconstruction of small energy deposits. The PMTs provide a time resolution of approximately 1 ns allowing a huge reduction of the background on the trigger level. The time of flight difference between signal and background is $\sim$ 6 ns.

The hadronic section of the SpaCal consists of 136 cells of $12 \times 12 \times 25$ cm^3 providing a hadronic interaction length. The fibres are of the same type as in the electro-magnetic part but have a larger, 1 mm diameter.

3.3 Energy Calibration of the SpaCal Electromagnetic Section

First the SpaCal must be correctly aligned with respect to the central jet chamber. Once this is achieved with the highest possible precision the energy calibration can start.

At fixed centre of mass energy at HERA, there are two free kinematic variables to be determined, but four can actually be measured, being these the energies and angles of both the scattered electron and the hadronic system. Therefore, taking into account conservation of energy and momentum,

there is redundancy in the kinematic reconstruction. There are four different methods of reconstruction: The electron method, the hadron method, the double angle method and the sigma method (and also the hybrid electron-sigma method). Detailed studies of the various kinematic reconstruction methods at HERA can be found in [47, 48].

The double angle method (see chapter 5) deals only with the electron and hadronic system angles and ignores their energies. The method is very precise (highest resolution) in the kinematic peak region, around 27.5 GeV, which is the energy of the electron beam, and for reasons of phase space that of the vast majority of deep inelastic scattered electrons. This method is insensitive to the energy scale. Only angles are measured and used to calculate variables x and Q^2. From them the energy of the scattered electron is calculated. Because of this the double angle method was chosen for the calibration of the SpaCal using only kinematic peak (electron) data.

The calibration of the SpaCal can be expressed as a minimisation of the functional:

$$S(\Delta g_{ic}) = \sum_{ev}(E_{da}^{ev} - \sum_{ic} E_{ic}^{ev}(1 + \Delta g_{ic}))^2 \rightarrow min. \qquad (3.1)$$

where Σ_{ev} is a summation over all selected events, Σ_{ic} is a summation over all cells included in the electron cluster, E_{da} is the double angle (true) energy, and Δg_{ic} is the correction to the amplification gain factor of the cell ic to be determined. However, many technical problems arise when trying to solve a system of 1192 equations with 1192 unknown variables, so another iterative procedure was chosen. In this procedure, the event mis-calibration (or event pull) is introduced for each event:

$$\delta_{ev} = 1 - \frac{\sum_{ic} E_{ic}^{ev}(1 + \Delta^{it} g_{ic})}{E_{da}^{ev}} = 1 - \frac{E_{cluster}^{ev}}{E_{da}^{ev}} \tag{3.2}$$

where it denotes an iteration number, with $\Delta^1 g_{ic} = 0$. The relative contribution of a cell j to the event pull is given by the fraction of energy deposited in it:

$$w_j^{ev} = \frac{E_j^{ev}(1 + \Delta^{it} g_j)}{E_{cluster}^{ev}}. \tag{3.3}$$

Finally, the weighted pull average over all events was calculated and the correction of all cell amplification gain factors was obtained:

$$\Delta^{it+1} g_j = \Delta^{it} g_j + \overline{\delta_{ev} w_j^{ev}}. \tag{3.4}$$

The iterative procedure was continued until $max_j|\overline{\delta_{ev} w_j^{ev}}| < 0.002$ (normally after three or four iterations).

Later the calibration has to be checked for lower and higher energies using other methods [49, 50, 51].

The H1 object oriented (H1OO) data storage model contains three hierarchical layers. The layer containing all reconstruction information is called ODS (Object Data Storage, $\sim$ 15 kB/evt.). It is the most complete layer from which the other two are created. The micro-ODS (μODS, $\sim$ 1.5 kB/evt.) contains limited information about the particles involved in every event and the HAT (H1 Analysis Tag, $\sim$ 0.5 kB/evt.) contains the event tag, which is the more general event information (Q^2, x, etc...).

Currently some of the information required for the calibration (energy clusters in SpaCal, Bacward Drift Chamber (BDC) [52] information and four-

vectors from the liquid Argon calorimeter) is neither in the HAT nor μODS, but in the ODS. Because ODS are big files and the information mentioned above is only a small part of these, a "user tree" was created. This is an additional USER data file ($\sim$ 1.2 kB/evt.) that contains only this information. Once the tree was built the HAT, μODS and USER files were used in conjunction to carry out the calibration of the SpaCal calorimeter.

3.3.1 Other Corrections

Three additional corrections were applied:

1. Inbox correction: Up to 1% difference between the energy measurement if the impact point was at the centre or at a corner of the hottest cell in the cluster. It is corrected for as a function of the distances between the impact point and the centre of the hottest cell in x and y.

2. Crack correction: 2% variations in energy due to cracks between supermodules. It is corrected for as a function of

$$r = max(|X_{SpaCal}||Y_{SpaCal}|). \tag{3.5}$$

3. Radius correction: Up to 1% energy variation at some radiuses (may be related to dead material in front of backward detectors). It is corrected for as a function of

$$R = \sqrt{X^2_{SpaCal} + Y^2_{SpaCal}}. \tag{3.6}$$

3.3.2 Results of the Calibration

The data sample taken in the year 2000 was used for this analysis. In order to get a clean sample of DIS events in which the scattered electron energy is inside the kinematic peak region, the following selection was applied:

For the cluster radius in the electromagnetic SpaCal (spread across several cells),

$$R_{cluster} < 4 \text{ cm}$$

ensures that the cluster is from the scattered electron. In photo-production events (see section 4.1.2), the electron goes down the beam pipe and sometimes a π^0 from the hadronic final state can fake its signal. The neutral pion decays mainly into two photons whose energies are usually collected in the SpaCal as one cluster. This clusters are wider than those from the scattered electron in DIS events, since there are two incident particles. Electron clusters radii are usually shorter than 4 cm.

For the cluster energy,

$$0.6E_{cluster} < E_{hottest}$$

requires that at least 60% of the energy of the cluster goes into one "hottest" cell (i.e., containing most of the energy of the cluster). This is to ensure that the cluster is compact, i.e., that it comes from the electron. Hadronic clusters formed by more than one particle do not have this small, well defined hot centre in a cluster. Also,

$$20 < E_{cluster} < 32 \text{ GeV}$$

ensures the electron is in the kinematic peak region, only these events are used for calibration with the double angle method.

For the backward drift chamber digitalisation hits (for θ_e determination by track fits),

$$2 < BDChits < 30$$

ensures there is a real track (so the cluster is not from a photon). To be able to fit a track, at least two hits are needed. If there were too many hits however, any arbitrary track could be fitted through them, which is the reason for the upper limit 30.

For the hadronic angle,

$$15^{\circ} < \gamma < 80^{\circ}$$

is used for kinematic peak selection.

And for the longitudinal position of the primary vertex,

$$|z_{vtx}| - 2.5 < 30 \text{ cm}$$

cuts down beam-gas interactions.

Finally, the SpaCal central box,

$$-16 < x < 9 \text{ cm and } -9 < y < 16 \text{ cm}.$$

was excluded to avoid the "hot-spot" region of the SpaCal (see section 3.2.5).

Five programmes were used to get the results of the calibration. The first one applies the selection, calculates the calibration constants for each cell and puts them in a text file. It then calculates the average of the constants for cells at the same distance from the centre to finally plot these averages as a function of SpaCal radius in a one dimensional histogram. The second, third and fourth programmes calculate the in-box, crack and radial corrections

respectively, calculating again the average for each radii, and put the results into text files again. The final programme applies all the corrections to to give the final calibration histogram. Figures 3.10 and 3.11 show the output of the first and last programmes respectively (i.e. before and after the calibration).

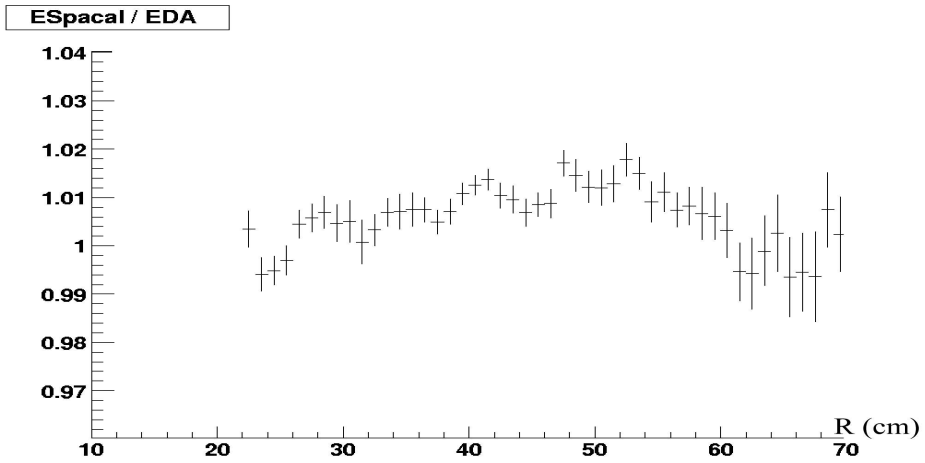

Figure 3.10: Ratio of the electron energy measured by the electromagnetic SpaCal to the electron energy as calculated from the double angle method, as a function of SpaCal radius, before the calibration of the SpaCal calorimeter. For some radii the difference between the two energies could be as high as 2%. This difference is a clear function of radius.

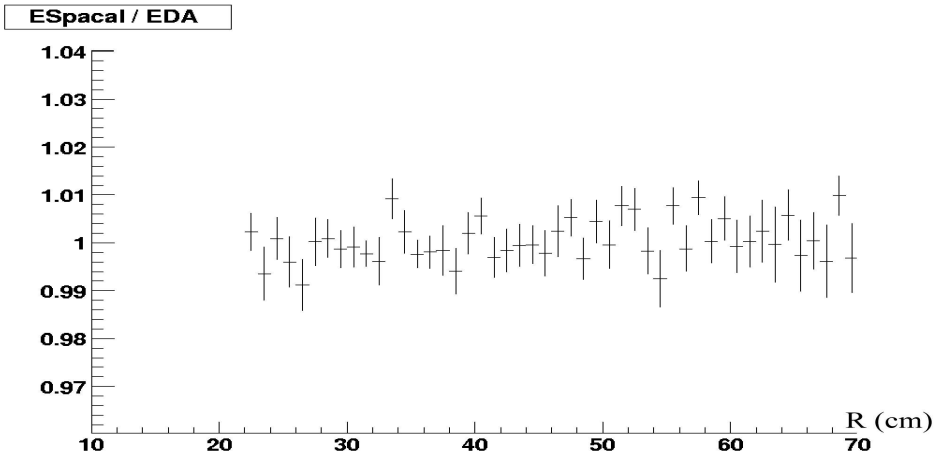

Figure 3.11: Ratio of the electron energy measured by the electromagnetic SpaCal to the electron energy as calculated from the double angle method, as a function of SpaCal radius after the calibration of the SpaCal calorimeter. The difference between the two energies is within 1%.

Chapter 4

Event Selection and Trigger Efficiency Studies

4.1 DIS Event Selection

Neutral current DIS positron data taken with the H1 detector in the year 2000 were used for this analysis. The majority of the total data taken is background coming from beam-gas, beam-wall, cosmic ray and photo-production events [53]. The following selection was applied in order to exclude these processes and get a pure sample of DIS events as inclusive as possible, and with minimum QED radiation effects in order to reduce the reliance on the correction mechanism.

4.1.1 Hardware Requirements

1. High Voltage Selection:

- $CJC1$, $CJC2$, LAr, $SpaCal$, CIP/COP, CIZ and BDC

  This selection ensures that all major sub-detectors, quoted above (see section 3.2), had the high voltage on when an event was recorded.

2. Trigger Selection:

- $S0$; (Sub-trigger 0).

  The sub-trigger $S0$ covers the most phase space for low momentum transfer. It will be discussed in more detail in the next section.

3. The central box cut from section 3.3.2 was also applied in the selection.

4.1.2 Physics Requirements

1. DIS Selection:

- Central Vertex; $-35 < z_{vtx} < 35$ cm.

  These cut is mainly to reject beam related background.

- $35 < E - p_z < 70$ GeV.

  For photo-production events rejection. In such events the incident electron emits a real photon (Bremsstrahlung) and continues down the beam pipe. There is a very high probability, especially at lower Q^2 values, for the photon to interact with the proton as a meson (mainly ρ). In some fraction of such events a π^0 can be produced from the $p\rho$ reaction. This pion decays mainly into two photons which, due to the

low mass of the meson, are almost collinear, easily faking the electron cluster in the calorimeters.

Because of energy and momentum conservation DIS events peak at an $E - p_z$ of 55 GeV (twice the energy of the incoming electron beam). In photo-production events however the electron exits down the beam-pipe and therefore its energy is not measured.

- $0.05 < y_h < 0.75$ and $|y_h - y_i|/y_h < 0.5$.

  Where y_i is the value of inelasticity as calculated from the reconstruction method chosen (electron or double angle), and y_h is the inelasticity as calculated from the hadron method (see section 5.1). This reduces QED radiation effects, which tend to be large for values of y close to zero or one.

  Since QED radiation affects the scattered electron energy and angle, the electron method for kinematic reconstruction, which is used in this thesis, is not very reliable in these regions of phase space. This is the reason for the selecting with y_h and requiring that y_i is within 50%.

2. **Low Q^2 Selection** (see section 6):

   - $12 < Q^2 < 150$ GeV^2.

     The desired range for this analysis. In this Q^2 region of phase space the scattered electrons are within the acceptance of the SpaCal calorimeter.

   - SpaCal electron, $E_e > 14$ GeV.

     At higher Q^2 values this helps to further remove photo-production events, where a low energy pion from the hadronic final state can fake a scattered electron signal.

- $150^{o} < \theta_e < 175^{o}$.

  Further ensures that the scattered electron falls into the SpaCal calorimeter.

- $30^{o} < \theta_q < 150^{o}$. Where,

$$\theta_q = 2\frac{180}{\pi}\arcsin\sqrt{\frac{Q^2}{4E_p x(\frac{Q^2}{4E_p x} + E_p x - \frac{Q^2}{4E_e})}} \tag{4.1}$$

is the scattering angle that a real quark would have, as calculated from the kinematics of the event assuming a QPM interaction [54]. This value is close enough to the scattering angle of the virtual struck quark to ensure that the hadronic products from the collision are well within the acceptance of the CTD and do not go into the transition regions between this detector and the forward and backward devices, thus not being recorded. This cut could actually be done in terms of apparatus dimensions, but doing it this way allows theorists to easily reproduce some results from the collisions just from the kinematics.

A phase-space diagram displaying the selected data is shown in figure 4.1. The diagram contains lines representing each of the selection cuts.

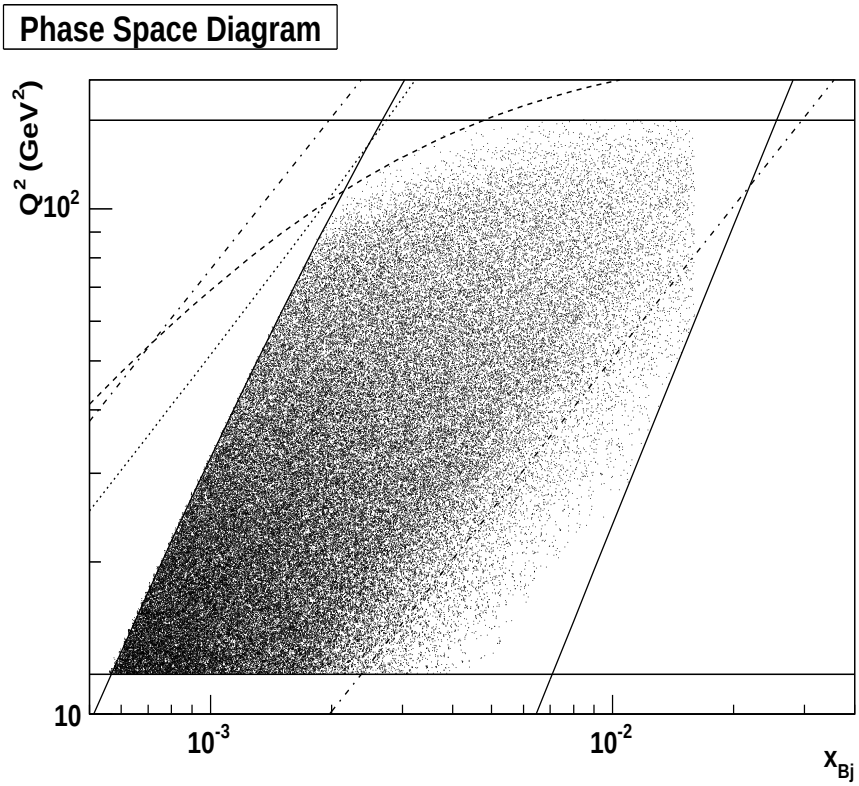

Figure 4.1: Phase space scatter plot showing the events values of Q^2 and x. Also shown are the cuts used for the analysis. The dotted line corresponds to $E_e = 14$ GeV, the dashed line is $\theta_e = 150^o$, the tilted solid lines are $\theta_q = 150^o$ (left) and $\theta_q = 30^o$ (right), and the dotted-dashed lines are $y = 0.7$ (left) and $y = 0.1$ (right). The data files used had a preselection to reject events with x values higher than 0.016.

4.2 Trigger Studies

4.2.1 Introduction

Different low momentum transfer trigger combinations were studied for the presented analysis. The trigger efficiencies for these combinations were calculated, and the number of events that passed each of them was recorded in order to get the best possible balance between efficiency and statistics. The efficiency of the triggers as a function of different kinematic variables was studied to try to identify any bias there might be. The same data selection described above was also used for these studies to provide a definition of clean physics events.

4.2.2 Sub-triggers studied

$S0$ was the first sub-trigger used. It is the one that covers the most phase space for low Q data, as its only requirement is that there be an electron in the SpaCal with recorded energy above 6 GeV, and does not have any track requirements thus being completely unbiased. An "*ORed*" combination of liquid argon, high Q^2, hadronic final state sub-triggers was chosen as a monitor for determining the efficiency of the electron based $S0$ trigger:

$$\text{LAr monitor: } S64, S66, S67, S75, S76, S77$$

This monitor selection is a collection of the following requirements:

- Event T0. This associates events with bunch crossings on the HERA clock.
- At least one high p_t track ($p_t > 500$ MeV/c).

- Transverse energy in LAr above 7.2 GeV.
- Energy in forward region above 7.5 GeV.
- Missing transverse energy above 3.8 GeV.
- High threshold LAr electron trigger ($E > 11$ GeV).

Using these as a monitor the efficiency of $S0$ was calculated to be:

$$\varepsilon_{S0} = \frac{N(Mon\&Trig)}{N(Mon)} = (99.6 \pm 0.02)\%.$$

with the error calculated from the binomial expression $\sqrt{Np(1-p)}$, where N is the total number of events and p the probability for an event to pass the trigger.

Despite the LAr monitor not being 100% efficient, this is the actual $S0$ efficiency, since whatever inefficiencies the subtriggers have are random.

This efficiency is shown in figure 4.2 as a function of the variables z_{vtx}, Q^2 (calculated with the electron method), E_e, and distance of the electron cluster from the centre of the SpaCal calorimeter ($x = y = 0$), R_{SpaCal}. The drawback is that, since $S0$ covers so much phase space, there is not enough bandwidth to record all events that pass the sub-trigger requirement, and therefore a variable prescale of up to 5 has to be applied to it (with a prescale of 5, only one in every five events is recorded). The high $S0$ prescale resulted in only 200 000 physics events available for the analysis. This number is good enough for an inclusive analysis, but for analyses of identified particles (K^0, Λ^0 etc...) it would be better to have more events.

Because it is unbiased and highly efficient, $S0$ was used as the monitor for the other SpaCal triggers under study.

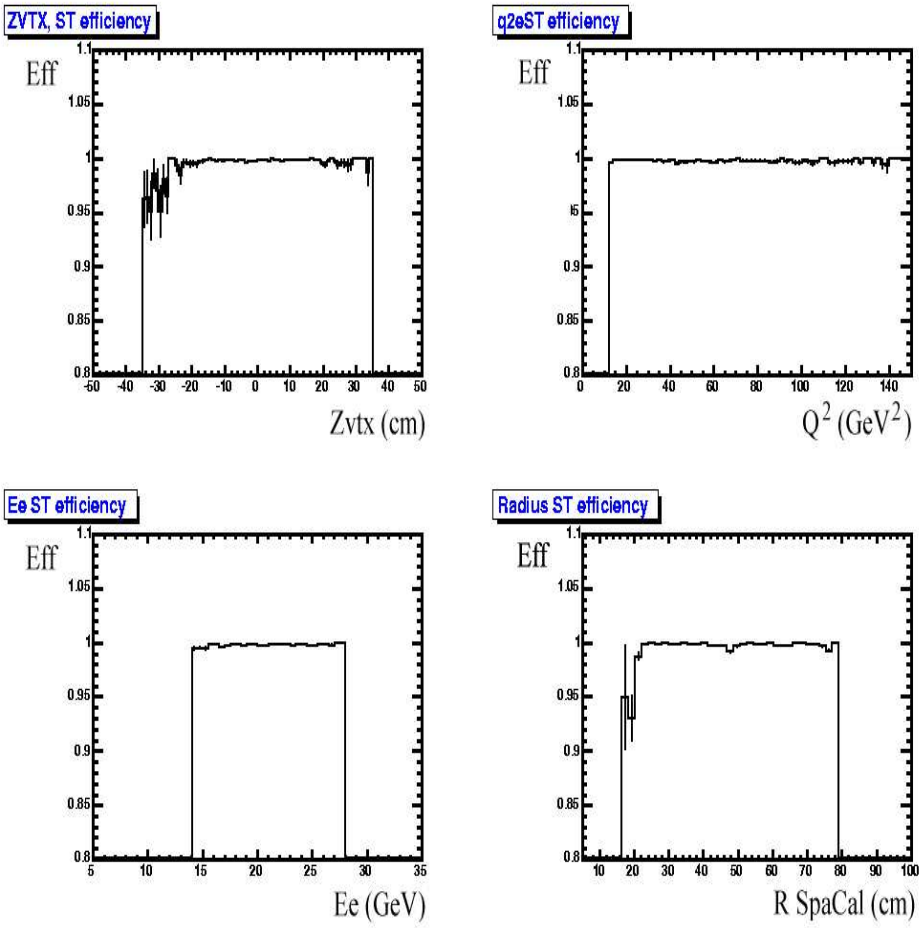

Figure 4.2: Efficiency of $S0$ as a function of z_{vtx} (cm), Q^2 (GeV^2), E_e (GeV) and R_{SpaCal} (cm). Note the suppressed zero. The efficiency drop seen at low Q^2, negative z_{vtx} and low R_{SpaCal} are correlated and represent the loss of low angle events due to detector acceptance.

S3: This trigger is a subset of $S0$, with the same level 1 requirement but also requiring the total energy in the SpaCal electro-magnetic section greater than 12 GeV, inside the time of flight window. An additional level 2 requirement is also implemented in $S3$: $R_{SpaCal} > 30$ cm.

In the same way as with $S0$:

$$\varepsilon = \frac{N(Mon\&Trig)}{N(Mon)} = (97.4 \pm 0.03)\%,$$

but since $S3$ is a subset of $S0$, the efficiency above is actually for the extra requirements of $S3$. To get the total efficiency of $S3$ the above efficiency is multiplied by the $S0$ efficiency, thus giving

$$\varepsilon_{S3} = 0.974 \times 0.996 = 0.970 = (97.0 \pm 0.04)\%.$$

with the errors added in quadrature.

This efficiency is shown in figure 4.3 as a function of z_{vtx}, Q^2, E_e, R_{SpaCal}.

There were more than twice the statistics available when using $S3$ than when using $S0$. The reason for this is that, although it has tighter physics requirements, $S3$ has no prescale, meaning that no events passing this subtrigger are rejected. The problem is the relatively low (97%) efficiency, especially at low scattered electron energies.

$S3||S61$: To try to improve the efficiency, $S3$ was "$ORed$" with $S61$, which has the same level 1 requirement as $S0$, but also some track requirements. These are that there be a significant central peak in the z_{vtx} distribution, at least one high momentum track candidate ($p_t > 500$ MeV/c), and high multiplicity (background) rejection. Again $S0$ was used as a monitor, giving:

$$\varepsilon = (99.3 \pm 0.02)\%.$$

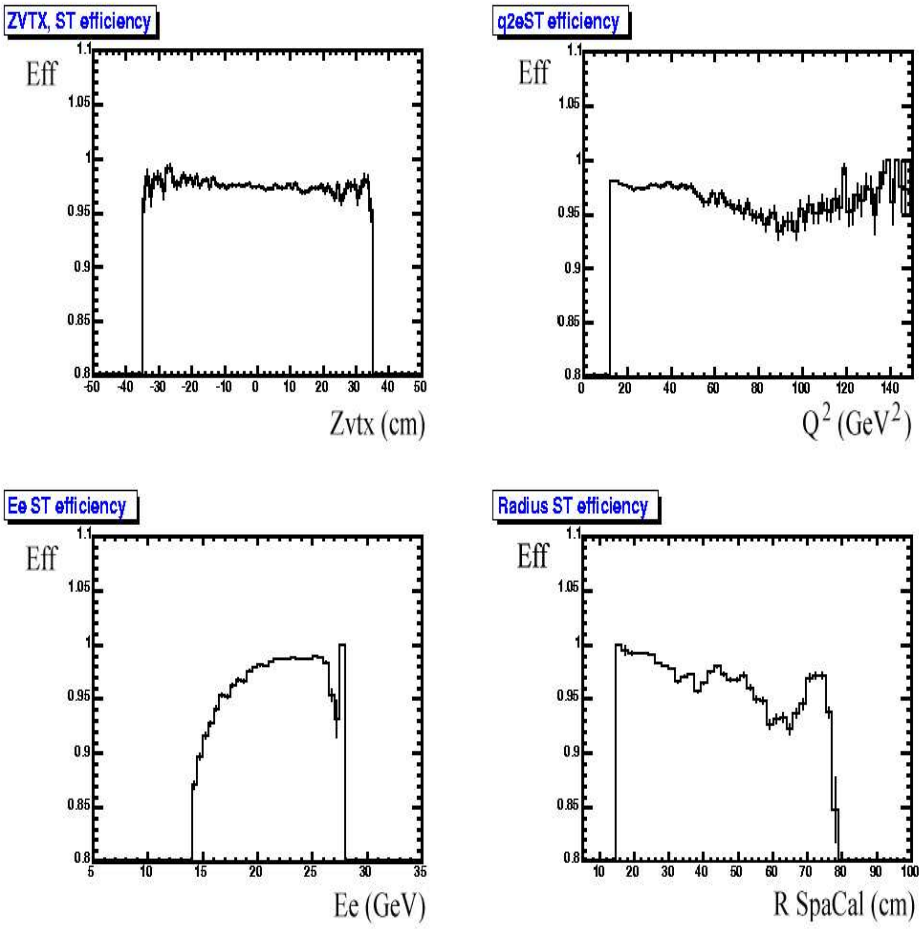

Figure 4.3: Efficiency of $S3$ as a function of z_{vtx} (cm), Q^2 (GeV^2), E_e (GeV) and R_{SpaCal} (cm). Note the suppressed zero. The drop in efficiency for high Q^2, large radius and high electron energy is due to bad cells in SpaCal. After removing those cell and applying a time cut ($7 < \Delta t < 18$ ns) the efficiency of $S3$ increases considerably (not shown).

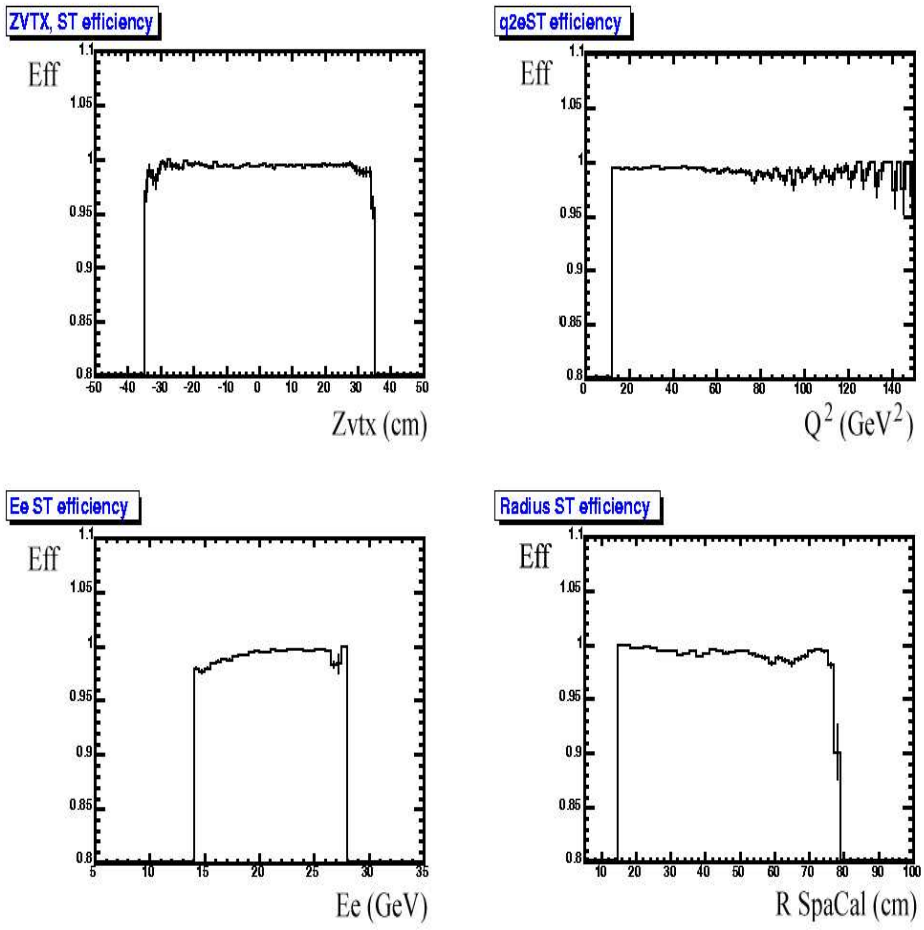

Figure 4.4: Efficiency of $S3||S61$ as a function of z_{vtx} (cm), Q^2 (GeV^2), E_e (GeV) and R_{SpaCal} (cm). Note the suppressed zero.

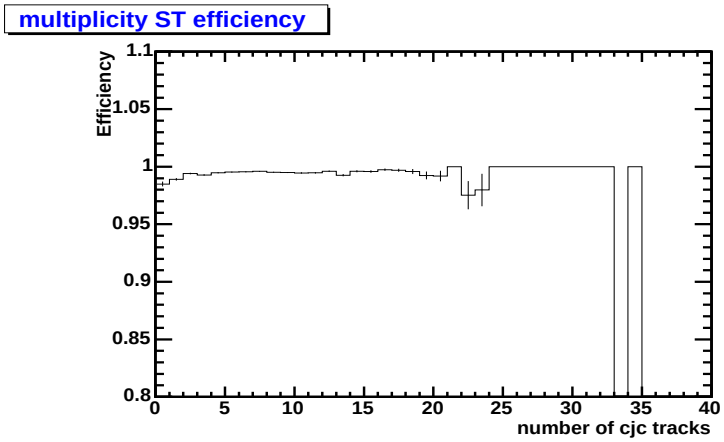

Figure 4.5: Efficiency of $S3||S61$ as a function of the number of CJC tracks Note the suppressed zero.

In the same way as $S3$, this is the efficiency of the "OR" of the $S3$ and $S61$ requirements not present in $S0$, so it has to be multiplied by the $S0$ efficiency, giving

$$\varepsilon_{S3||S61} = 0.993 \times 0.996 = 0.989 = (98.9 \pm 0.03)\%,$$

which is adequately high. Also, out of the different triggers studied, this combination gives the most number of events (around 50% more than when using $S3$ alone). The drawback is that using $S61$, being a track based trigger, might introduce a bias in the track based analysis.

This efficiency is shown in figure 4.4, again as a function of z_{vtx}, Q^2, E_e, R_{SpaCal}.

Because of the track requirement of $S61$, the efficiency of $S3||S61$ is shown also as a function of the number of CJC tracks in figure 4.5. Note that even with no tracks in the apparatus the OR of these sub-triggers is sufficient to

ensure better than 98% efficiency.

4.2.3 Conclusions

The final decision was to use $S0$ (the one covering most phase space, highly efficient and unbiased) since, although it does not provide as many events as the others due to its high prescale, the accuracy of the final analysis is limited by the systematic uncertainty. $S3||S61$ would have been used if more tracks were needed.

Chapter 5

Data Quality and Corrections

5.1 Data Quality

This section is intended to establish the level of agreement between the H1 data sample and the data provided by the generator DJANGOH13 when passed through the H1 simulation $H1Sim$ [55], to the extent that acceptance corrections can be believed. The simulation uses the GEANT program package [56]. As mentioned earlier, there are various methods that can be used for the reconstruction of the kinematic event variables. For reasons to be given later, the analysis was carried out twice (with the same data set), once using the electron method and once using the double angle method.

The electron method, as the name suggests, uses the information from the scattered electron only, namely the energy, E'_e, and polar angle, θ_e. The method was chosen because it is independent of the hadronic final state, which *is* what is being studied in the analysis, thus eliminating the possi-

bility of any bias. The kinematic variables as calculated from this method are as follows:

$$y_e = 1 - \frac{E'_e}{E_e} sin^2 \frac{\theta_e}{2}, \tag{5.1}$$

$$Q^2_e = 4 E_e E'_e cos^2 \frac{\theta_e}{2}, \tag{5.2}$$

where E_e is the electron beam energy. Q^2_e is always well measured, but the fractional resolution of y_e degrades as $1/y$ because of the dependence on the scattered electron energy. This means that for low y values the hadron method, using information from the hadronic system only, is better, as it gives the best resolution in this phase space region. This is the reason for using both y_e (or y_{da} for the second analysis) and y_h in the selection. The latter is expressed as:

$$y_h = \frac{\sum_h (E - p_z)_h}{2E_e}, \tag{5.3}$$

where the subscript h stands for observed hadrons. Note that $E \approx p_z$ for hadrons that are missed close to the beam pipe. Therefore these hadrons contribute little error.

The double angle method uses the angle of the scattered electron, θ_e, and that of the hadronic system, γ, where

$$cos\gamma = \frac{(\sum_h p_{xh})^2 + (\sum_h p_{yh})^2 - (\sum_h (E - p_z)_h)^2}{(\sum_h p_{xh})^2 + (\sum_h p_{yh})^2 + (\sum_h (E - p_z)_h)^2}. \tag{5.4}$$

The method is therefore insensitive to the energy scale. The existence of large systematic errors coming from the uncertainty of this scale (see sec-

tion 8.1) was the main reason for using the double angle method in a second analysis. The kinematic variables as calculated from the double angle method are as follows:

$$Q^2_{da} = \frac{4E_e^2 sin\gamma(1+cos\theta_e)}{sin\gamma + sin\theta_e - sin(\gamma+\theta_e)}, \tag{5.5}$$

$$x_{da} = \frac{E_e}{E_p} \cdot \frac{sin\gamma + sin\theta_e + sin(\gamma+\theta_e)}{sin\gamma + sin\theta_e - sin(\gamma+\theta_e)}, \tag{5.6}$$

where E_p is the incoming proton beam energy.

The following figures correspond to the data quality histograms for the analysis carried out with the electron method. For the histogram labels, N is used for the total number of events in the sample, n for the number of events in a given bin, and $n^{\pm}$ for charged tracks, simply referred to as tracks. Comments on the level of agreement between the H1 data (points) and the Monte Carlo (histograms) samples are made after all figures are presented.

From the electron side, the scattered electron polar (θ_e) and azimuthal (ϕ_e) angles distributions are shown in figure 5.1. As expected, in the vast majority of events the electron is scattered at low angles[1] (low Q^2), and the azimuthal distribution is flat. The scattered electron energy and the radius of its cluster in the SpaCal calorimeter are shown in figure 5.2. The high energies correspond to low Q^2 events, and the short radii correspond to small scattering angles.

From the hadron side, the distributions for the variables $E - p_z$ and z_{vtx} are shown in figure 5.3. Due to energy and momentum conservation, $E - p_z$ peaks at twice the electron beam energy. A reweight on the z-vertex

[1] Due to the H1 coordinate system, low electron scattering angles correspond to large values of θ_e

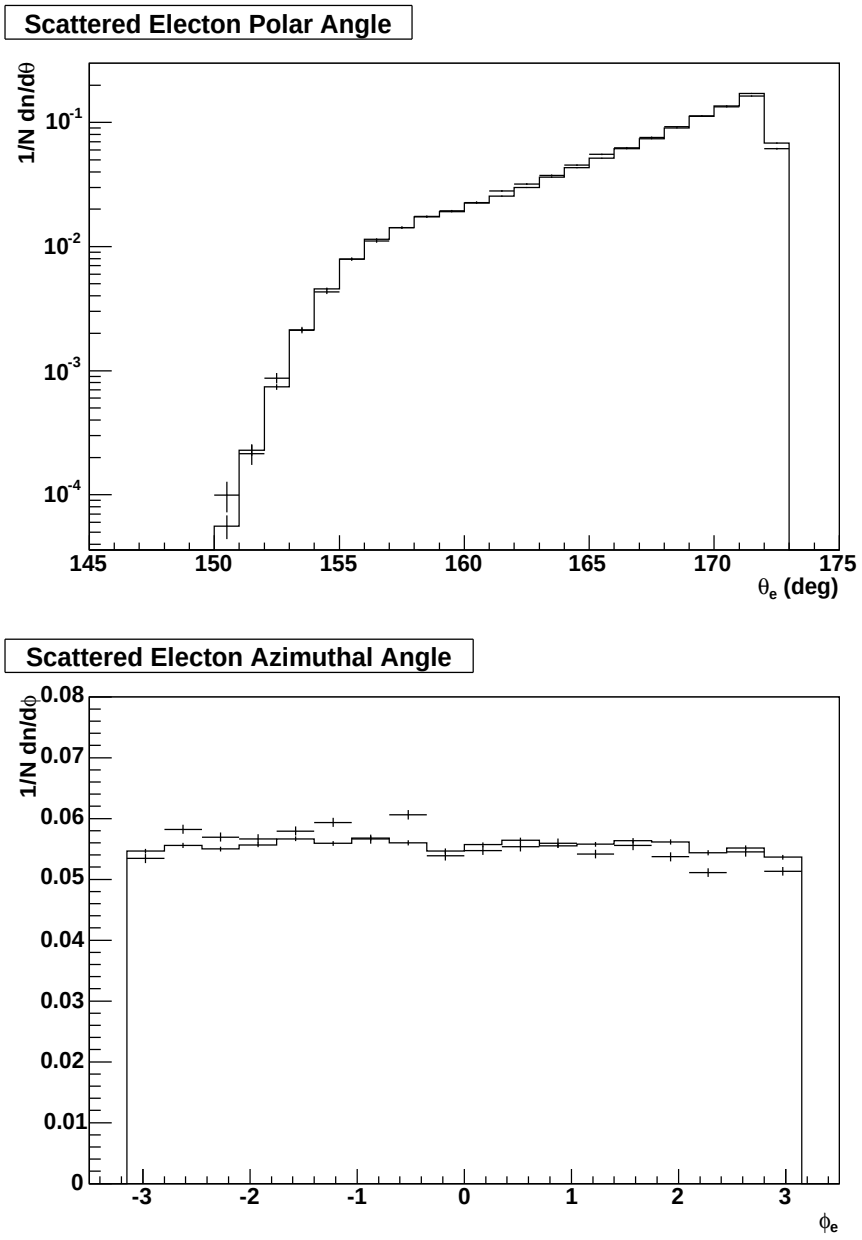

Figure 5.1: Distributions for the scattered electron polar and azimuthal angles (electron method). Note the suppressed zero in the electron polar angle distribution.

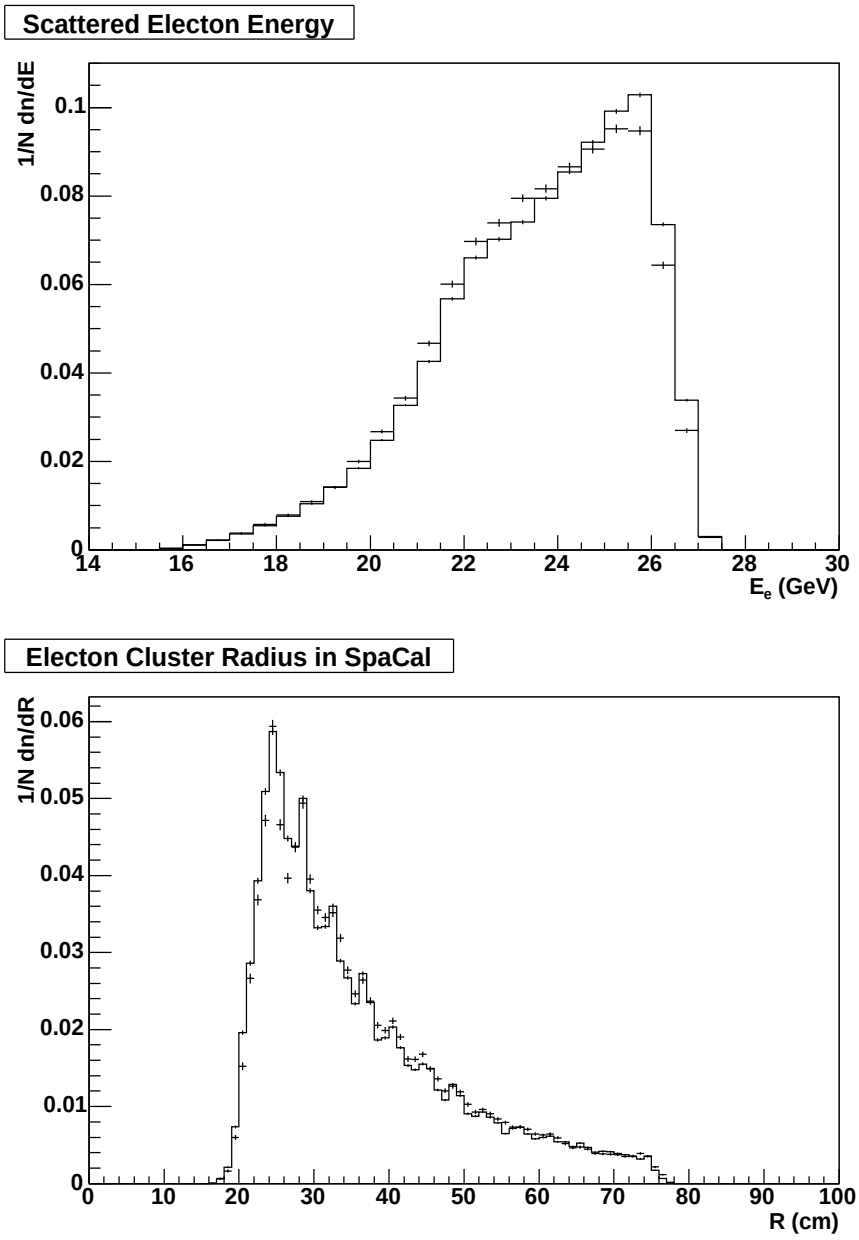

Figure 5.2: Distributions of the scattered electron energy and the radius of its cluster in the SpaCal calorimeter (electron method). Note the suppressed zero in the energy distribution.

distribution was applied to the reconstructed Monte Carlo. This was done by fitting a gaussian to the data distribution, getting from it the mean and standard deviation, and imposing this function on the Monte Carlo. This is necessary, since the calorimeters assume all events come from a vertex at $z = 0$, and any differences between the z-vertex in the data and that in the Monte Carlo will produce differences in the measured quantities. The distributions for the variables p_t balance (defined as the ratio of the transverse momentum of the summed hadrons to that of the electron) and θ_q, as calculated in equation 4.1, are shown in figure 5.4. The balance in transverse momentum peaks at a value slightly below 1, as on the hadronic side there are some undetected (low energy) muons and neutrinos. In the histogram for θ_q it can be seen that in most events the scattered quark goes into the backward region of the detector. This is because, even though the data selected is in the low momentum transfer region of the phase space, this also corresponds to very low x Bjorken, i.e., low quark momentum.

For the kinematics, the variables Q^2 and x are shown in figure 5.5. The $1/Q^4$ behaviour of the cross section can be seen in the Q^2 distribution. The inelasticity is shown in figure 5.6. From the relation in equation 2.4 it can be seen that the Q^2 distribution peaking at minimum values means the x and y distributions also peaking at the lowest values.

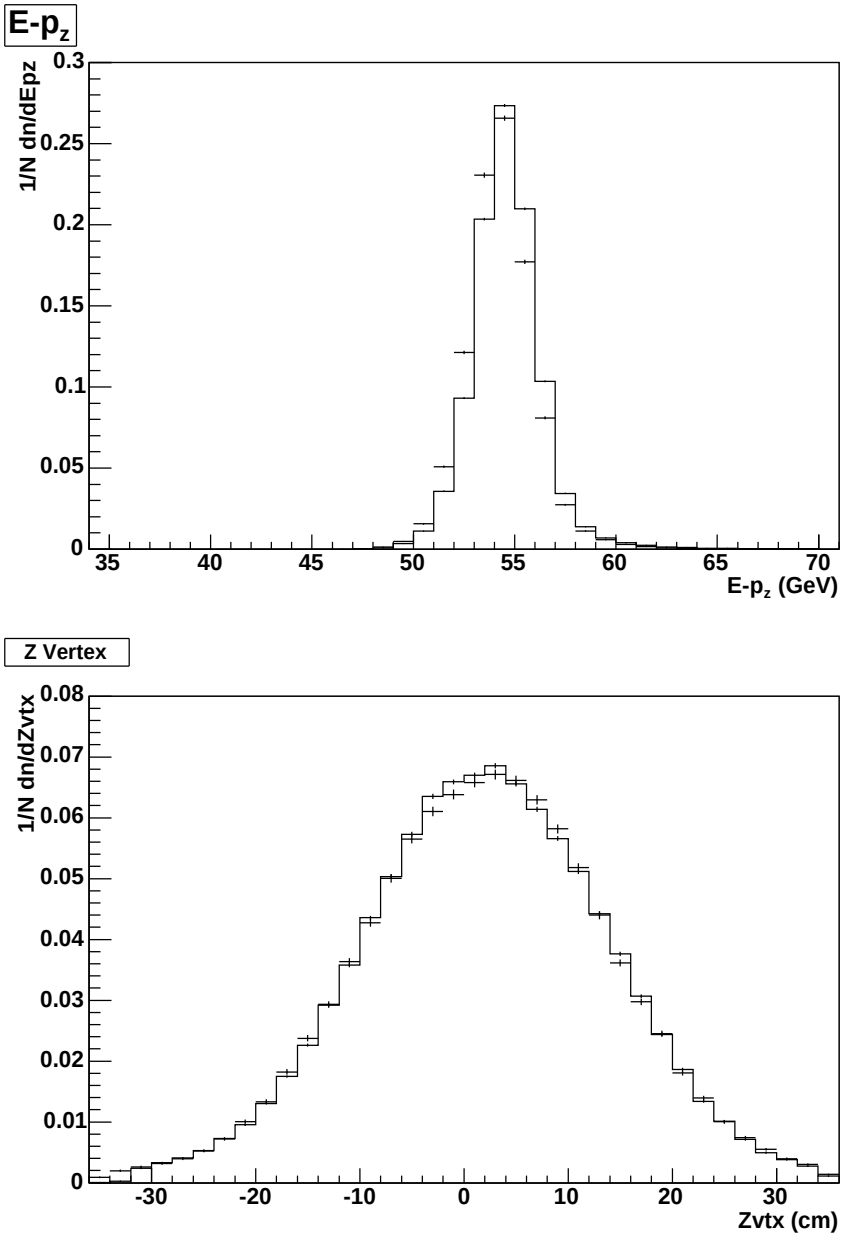

Figure 5.3: The distributions of variables $E - p_z$ and $z - vertex$ (electron method).

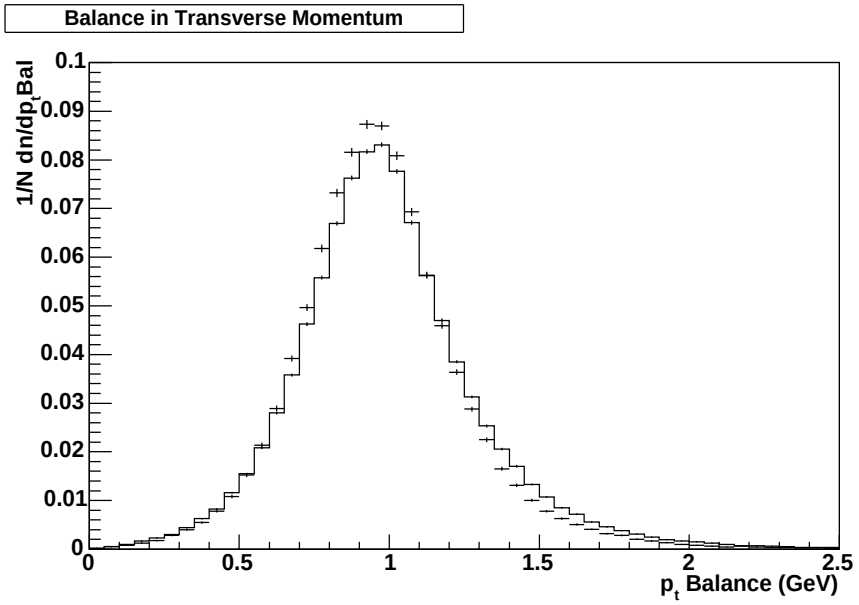

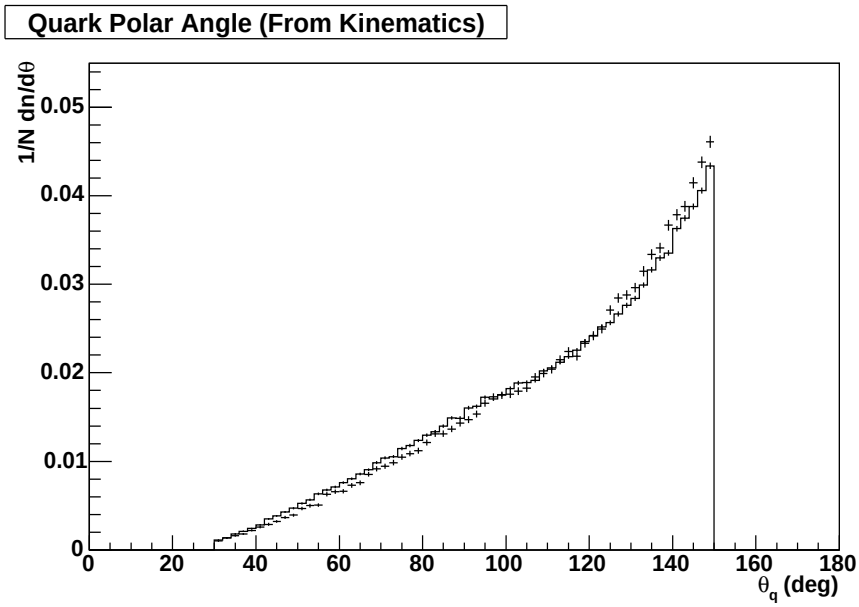

Figure 5.4: The distributions of variables p_t balance and θ_q (electron method).

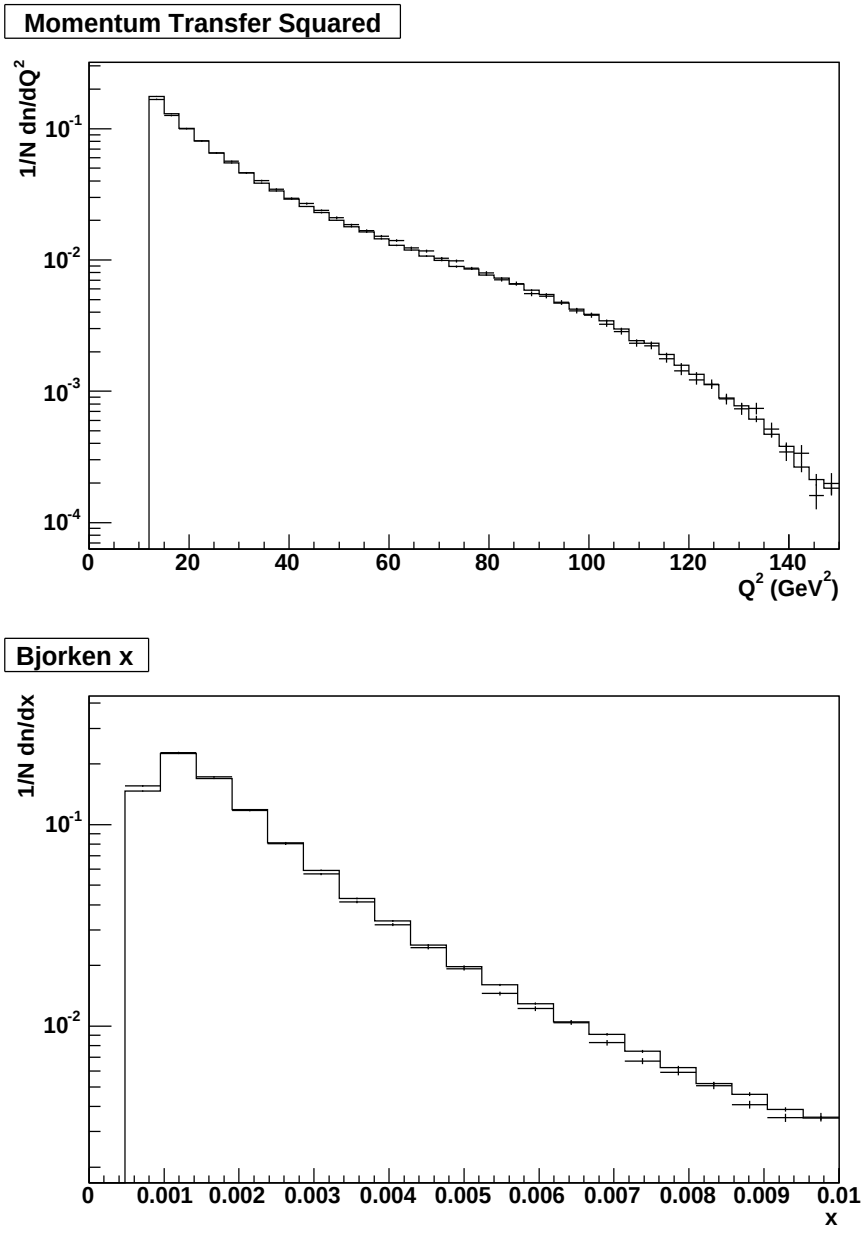

Figure 5.5: The distributions of variables Q^2 and x, as reconstructed with the electron method.

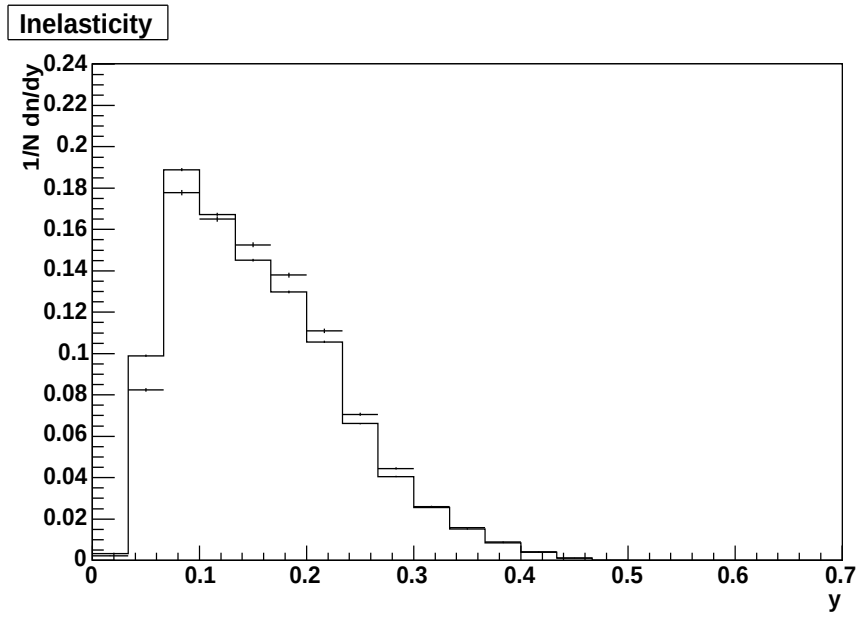

Figure 5.6: Inelasticity distribution as reconstructed with the electron method.

The distribution of the total charged track multiplicity, $n^{\pm}$ is shown in figure 5.7. Most events display a low multiplicity, as might be expected at low momentum transfers. The polar and azimuthal angle distributions for the tracks are shown in figure 5.8, where it can be seen that the majority of tracks go in the forward direction. These are the tracks related to the proton remnant. The tracks going into the backward region are mostly the ones related to the struck quark. As expected, the tracks are evenly distributed in azimuth. The energy and transverse momentum distributions of the tracks can be seen in figure 5.9. Most of the tracks have low energy and have a small transverse component of momentum, as they are mostly forward tracks. The distributions for track length and distance of closest approach to the primary vertex are shown in figure 5.10. These distributions

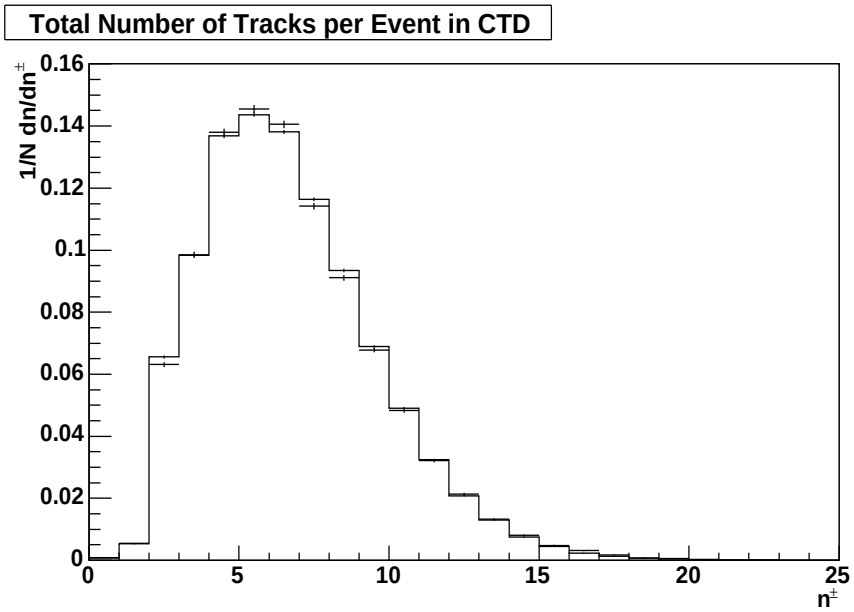

Figure 5.7: Charged track multiplicity distribution.

are somewhat different than the rest, since they are related to measurement efficiency and not to the underlying physics of DIS.

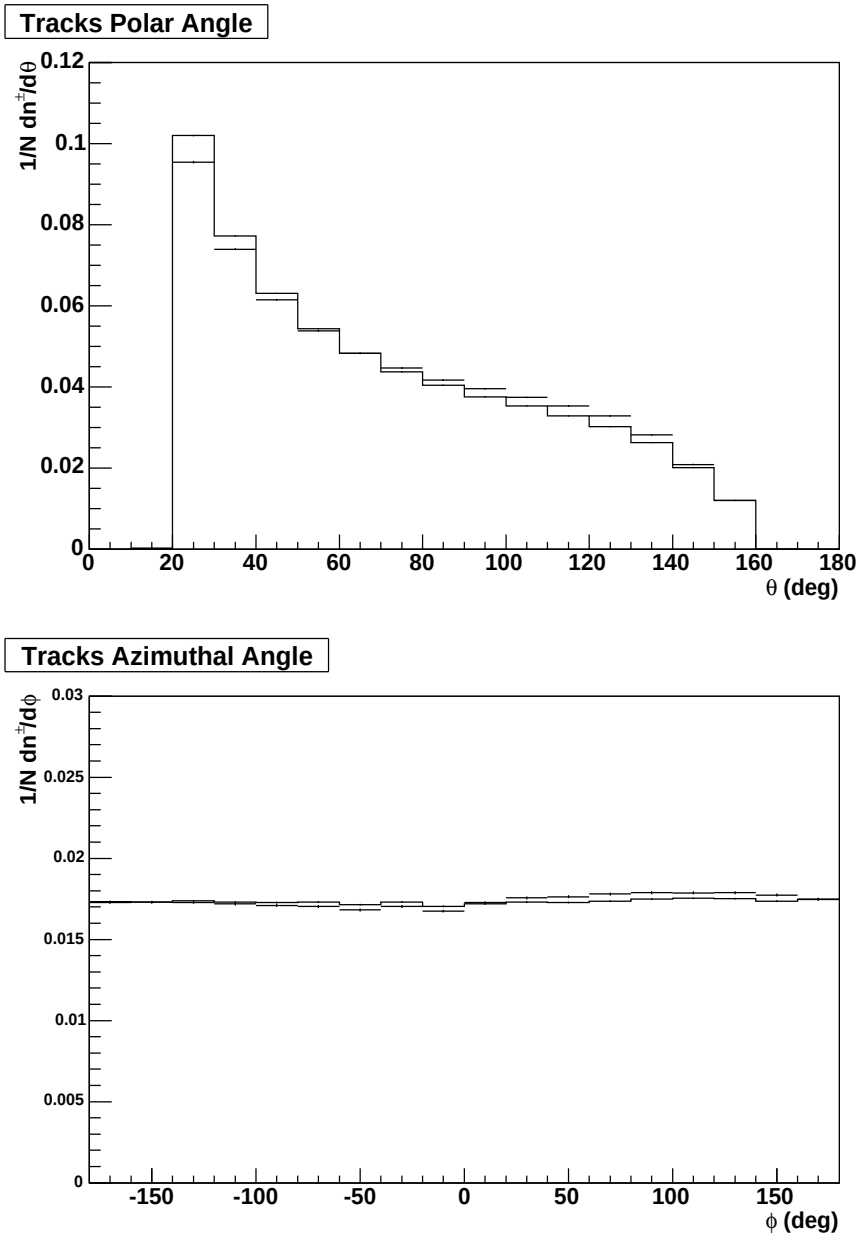

Figure 5.8: Distributions of the tracks polar and azimuthal angles (electron method).

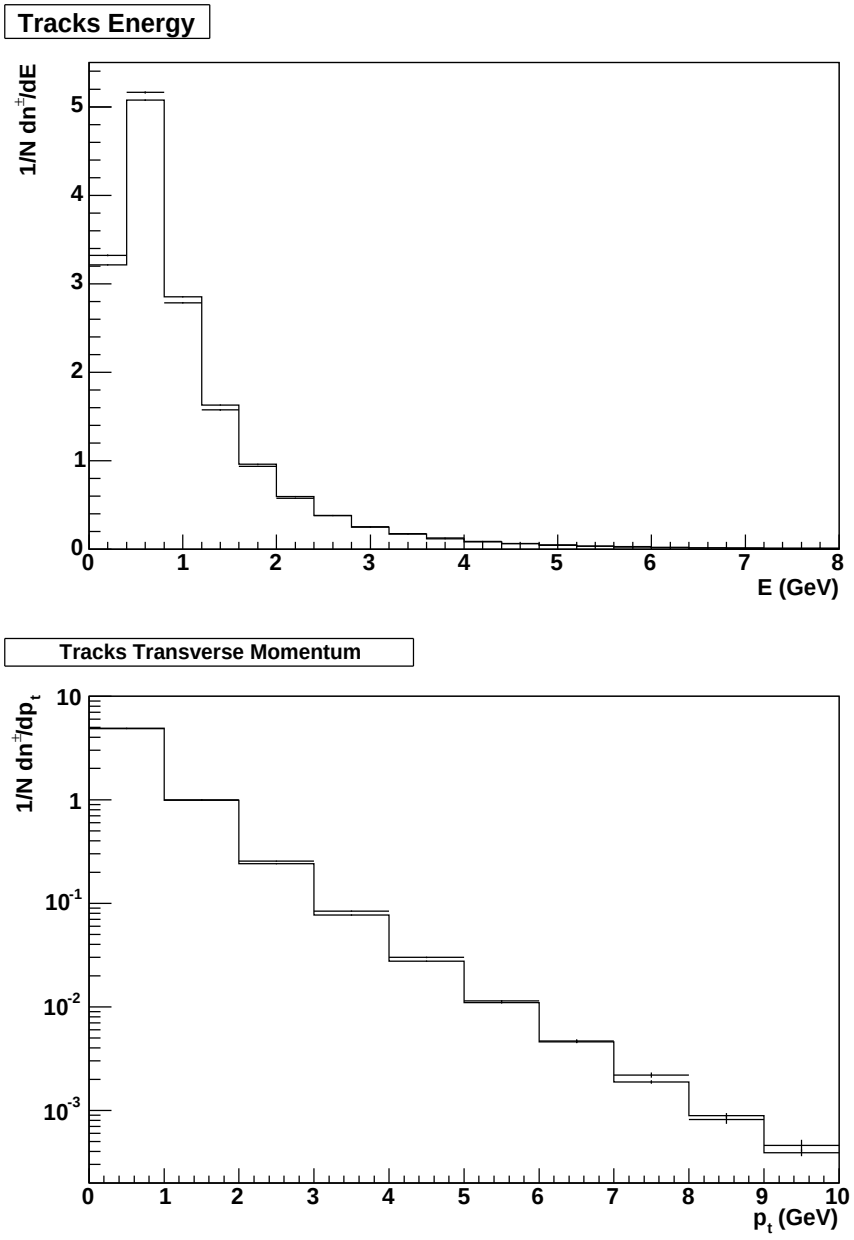

Figure 5.9: Energy and transverse momentum distributions of charged tracks (electron method).

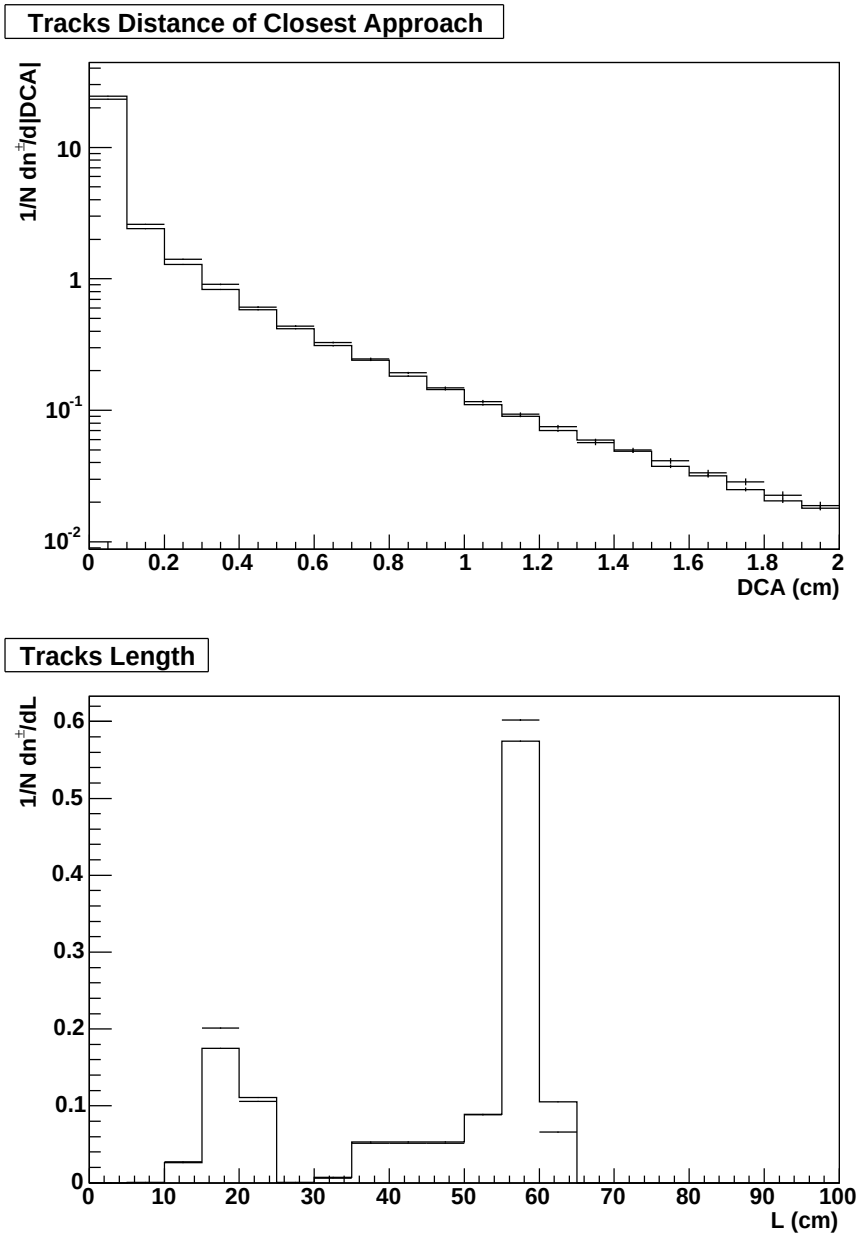

Figure 5.10: Tracks distance of closest approach to primary vertex and track length distributions (electron method).

There is overall a good agreement between the H1 data sample and the Monte Carlo simulated one, but a few points should be noted. In the scattered electron energy in figure 5.2 there is a shift between the two distributions ($\sim$ 0.5 GeV at the highest end). This shift is taken to be caused by the $\sim$ 1% uncertainty in the measured energy due to the calibration of the SpaCal calorimeter (see figure 3.11). The agreement is poorest at high energies, where the shape of the kinematic peak is not well reproduced. This could be explained by noting that this region of phase space corresponds to the shortest radii in the SpaCal calorimeter (hot-spot region), where, even with the box cut applied in the selection, there remain some problematic cells. This is further supported by the distribution of the electron energy from the double angle method (figure 5.11), where this difference is not present, although the shift still is. These data-Monte Carlo differences in the electron energies obviously have an effect in the distributions of $E - p_z$ from figure 5.3. The difference in the p_t balance distributions in figure 5.4, can be accounted for by the 4% scale uncertainty in the energies measured in the liquid argon calorimeter [57]. The difference in the y_e distributions from figure 5.6 are largest at low values of y, since, as mentioned earlier, the electron method has a poor y resolution in this region due to QED radiation effects.

The next set of figures contain the data quality histograms for the analysis carried out with the double angle method. Only the ones corresponding to those mentioned in the previous paragraph will be discussed, since the rest of the distributions are well described and look much the same. The scales have been left unchanged to allow for comparisons between the two methods to be made.

The scattered electron energy distributions in figure 5.11 display the shift

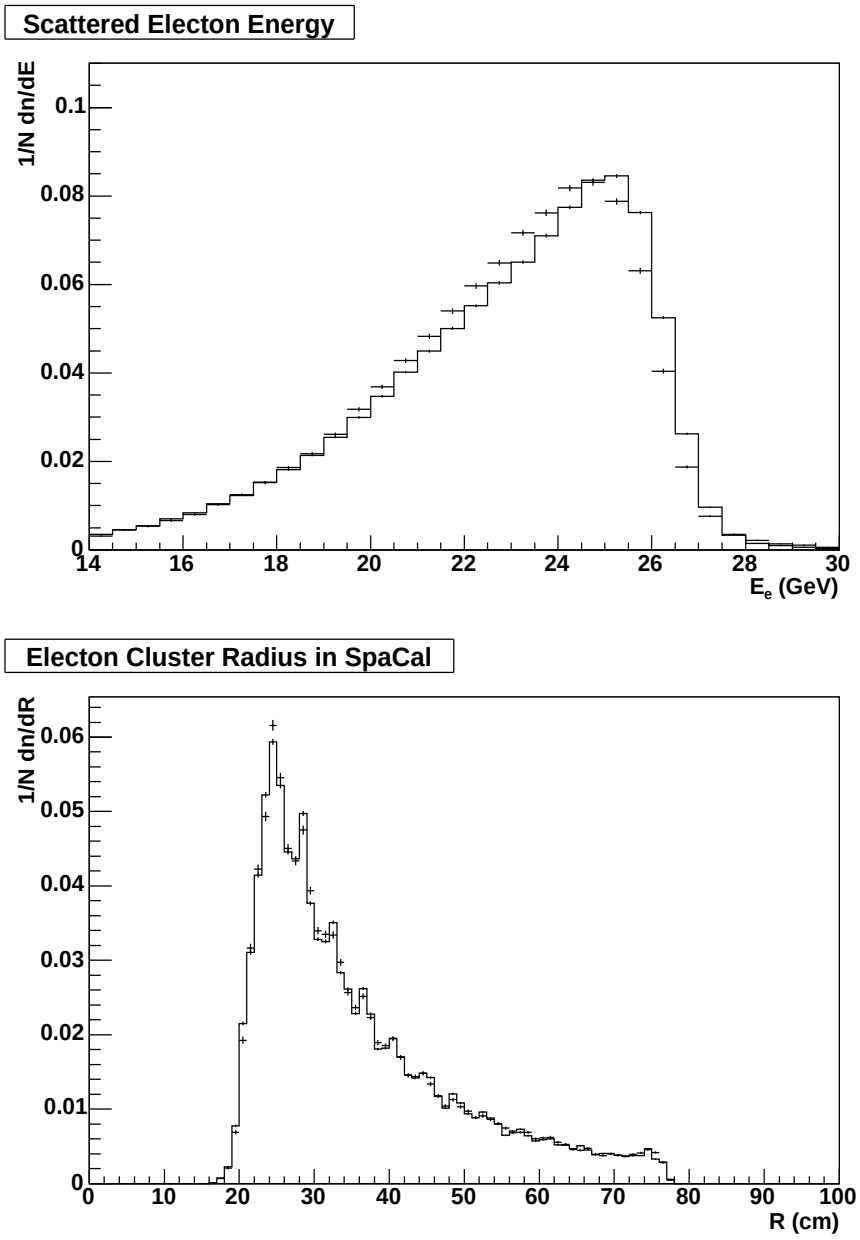

Figure 5.11: Distributions of the scattered electron energy and the radius of its cluster in the SpaCal calorimeter (double angle method). Note the suppressed zero in the energy distribution.

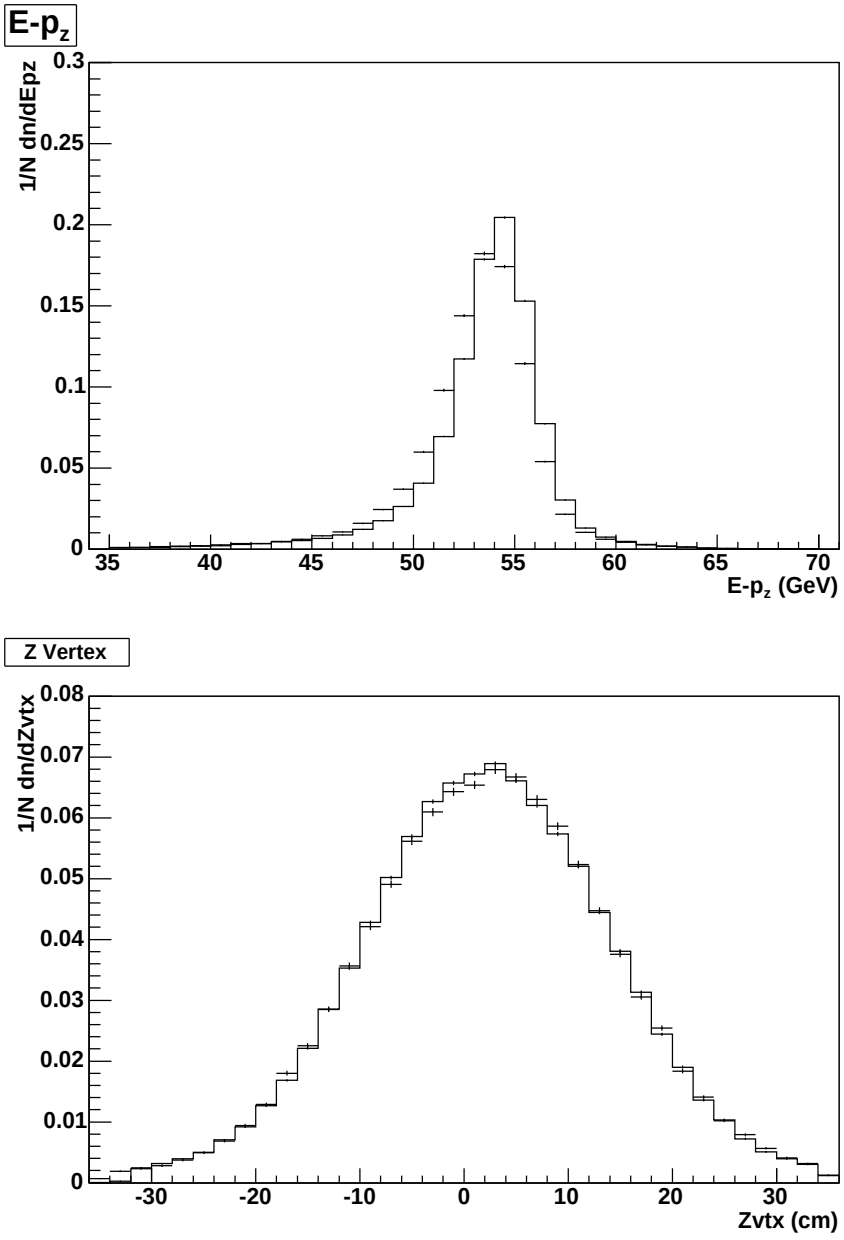

Figure 5.12: The distributions of variables $E - p_z$ and $z - vertex$ (double angle method).

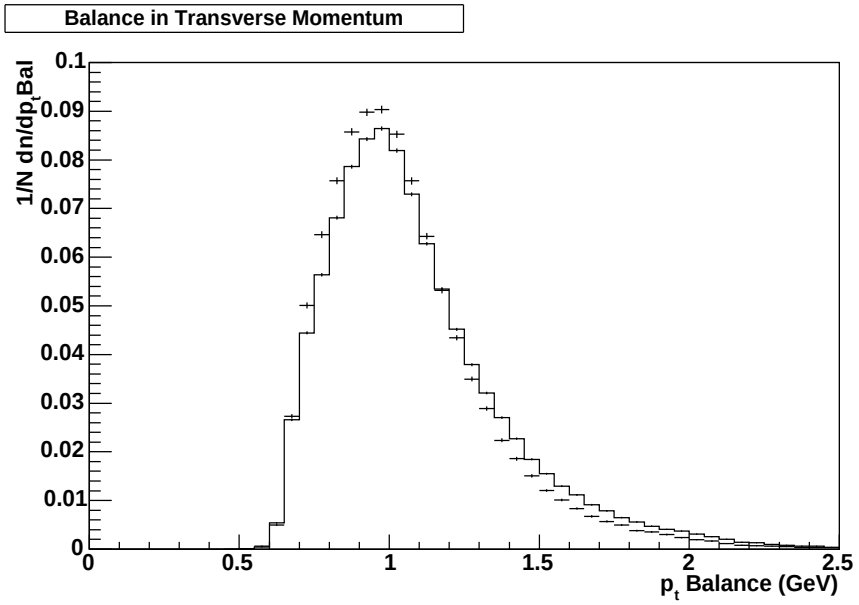

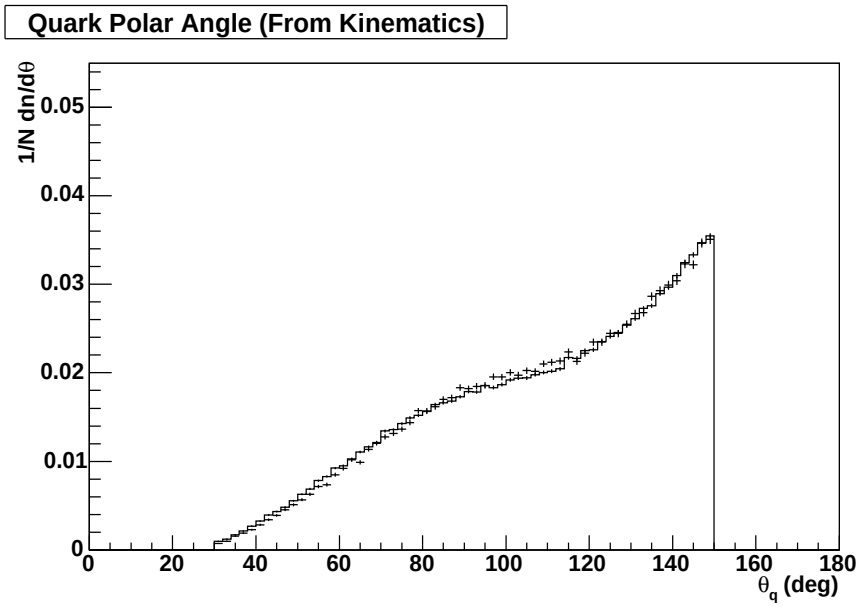

Figure 5.13: The distributions of variables p_t balance and θ_q (double angle method).

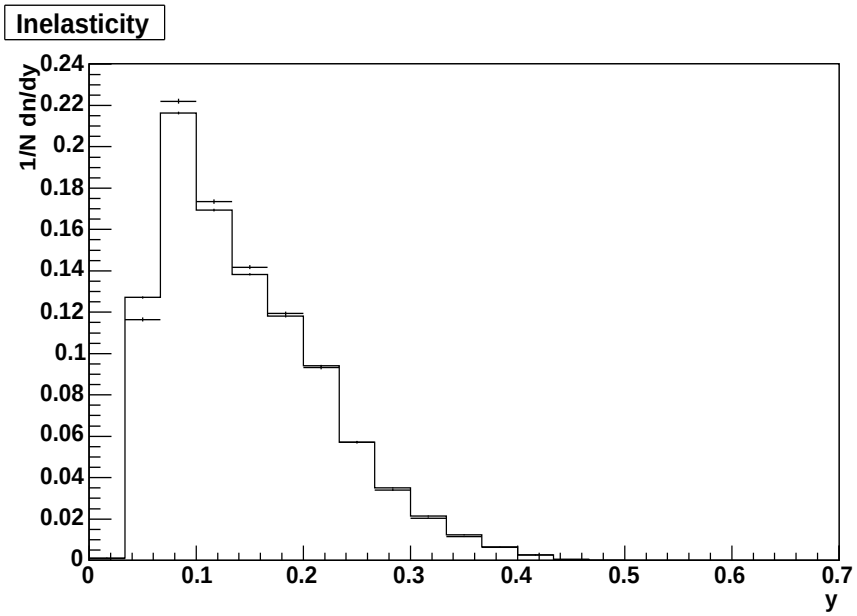

Figure 5.14: Inelasticity distribution as reconstructed with the double angle method.

also present in figure 5.2, but not the discrepancy in the kinematic peak region (this energy is reconstructed from the angles, not from the SpaCal calorimeter). The difference in the SpaCal radius between the methods can only be due to the difference in the reconstruction of the variables used in the selection, as both methods use the scattered electron angle, i.e., the electron cluster, in the SpaCal calorimeter. The same differences are also observed in the $E - p_z$ and p_t distributions (figures 5.12 and 5.13), for the same reasons as above. The y distributions however display a better agreement, since in the case of the double angle method only one of the measured quantities (θ_e) is affected by QED radiation.

5.2 Data Corrections

The main reason for using Monte Carlo generators and simulations is to correct the data collected by H1 for detector acceptance and calibration. The Monte Carlo generated (g) events, coming from the theory and models implemented in the generators, are passed through the detector simulation to produce the reconstructed sample (r). Since the simulation of the detector is supposed to reproduce all the properties and also the same inefficiencies and acceptance problems as the real detector, the reconstructed Monte Carlo sample should ideally reproduce the distributions of real data (d), given that the theory and models in the generator provide a good description of the real world.

To correct any real world measurable quantity for these detector effects and get the *real world* "true" value, known as corrected data (c), the following operation is performed:

$$c = d \times \frac{g}{r}. \tag{5.7}$$

Since d and r are very similar, c should be very similar to g. Any large discrepancies between them would have to be attributed to a problem in the underlying theory and models implemented in the Monte Carlo generator, since the modelling of the detector should be very accurate. After all, physicists have designed and built the detector, and therefore should be able to model it well. The quantity g/r is known as a correction factor, and when the real world physics are well modelled by the Monte Carlo, should be close to unity.

To correct for QED radiation, an extra correction factor is added to the

expression above. This correction factor is the ratio g_{nr}/g_r, where g_r is the value resulting from the default (radiative) Monte Carlo and g_{nr} is the value from the same sample, but with QED radiation turned off. The final correction is then,

$$c = d \times \frac{g_r}{r} \times \frac{g_{nr}}{g_r} = d \times \frac{g_{nr}}{r}, \tag{5.8}$$

where the term g_r cancels, and the total correction can be performed using only g_{nr}. In this thesis the corrections were performed this way and for each bin of phase space. In the following chapters, the correction factors for the relevant quantities will be presented along with the (corrected data) distributions for these quantities.

Chapter 6

The Breit Frame of Reference

Unlike many of the inertial frames of reference used in particle physics, the Breit frame [58] is not defined as the rest frame of any particular particle or set of particles, but rather as the frame in which the exchanged virtual boson is entirely space-like. The term space-like means that the boson has zero energy, and thus a magnitude of momentum equal to Q. As with the laboratory frame, the positive z axis is chosen to be in the direction of motion of the proton beam. The incoming and outgoing electrons thus have the same energy and magnitude of momentum, so the photon is collinear with the proton beam. An azimuthal rotation can be used afterwards to constrain the electron scattering plane to be in the $x - z$ plane. In the naive Quark-Parton Model, for an elastic collision between the photon and a quark, the latter has to have an initial z momentum of $Q/2$ and a final one of $-Q/2$ in order to conserve momentum and energy. A diagram of an ep collision boosted to the Breit frame of reference for a QPM event is shown

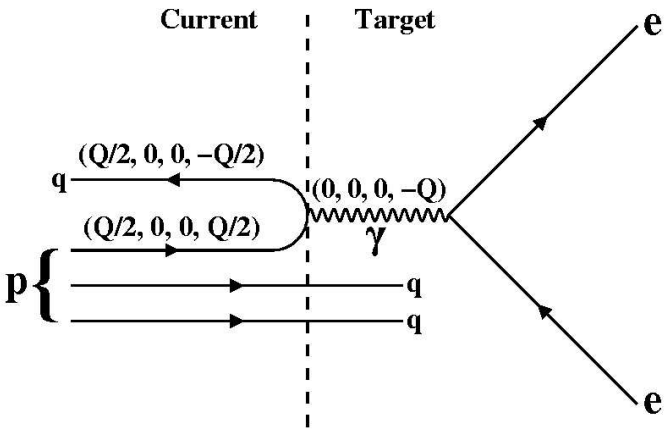

Figure 6.1: A NC, DIS, QPM ep collision boosted to the Breit frame of reference. Particles of interest are shown with their four momentum components.

in figure 6.1.

It is worth noting the similarities of the Breit frame with the hadronic centre of mass system (CMS), which, by construction also has the z axis aligned with the direction of the incoming proton. In both frames, after a DIS collision the proton remnant (spectator), which does not interact, continues in this direction and the current is directed toward the negative z direction. It is therefore clear that the transformations from one frame to the other consist in just a longitudinal boost.

6.1 Boosting to the Breit Frame

Boosting to the Breit frame could be done in one operation but it is usually done in two stages. First the events are boosted from the laboratory frame to the hadronic Centre of Mass System (CMS). The following equations give the Lorentz boost of an arbitrary four vector $p = (E, \vec{p})$ from a frame

of reference O into another frame O' with velocity $\vec{\beta}$ with respect to O:

$$E' = \gamma(E - \vec{\beta} \cdot \vec{p}) \tag{6.1}$$

$$p'_{||} = \gamma(p_{||} - \beta E) \tag{6.2}$$

$$\vec{p}'_{\perp} = \vec{p}_{\perp} \tag{6.3}$$

where $p_{||} = \vec{\beta} \cdot \vec{p}/\beta$, $\vec{p}_{\perp} = \vec{p} - p_{||}\vec{\beta}/\beta$, $\vec{\beta} = \vec{p}'/E'$, and $\gamma = (1 - \beta^2)^{-1/2} = E'/\sqrt{p'^2}$ is the usual Lorentz dilation factor. To boost the particles from the laboratory frame to the CMS, the total momentum of the hadronic CMS is calculated relative to the laboratory from the final reconstruction of an event. The relative velocity of the two frames (β) is then calculated by requiring the total momentum of the hadronic system to be zero in the CMS frame. Finally, it is a matter of inserting this relative velocity into the equations to get the particles boosted.

The transformation to the CMS is completed by a rotation, which by convention aligns the negative z axis with the direction of the virtual photon. The rotation operator is given by

$$R = \begin{pmatrix} 1 & O \\ O^T & \tilde{R} \end{pmatrix} \tag{6.4}$$

where O is the row matrix (0, 0, 0), and $\tilde{R} = R_y(\theta)R_z(\phi)$ with

$$R_y(\theta) = \begin{pmatrix} cos\theta & 0 & -sin\theta \\ 0 & 1 & 0 \\ sin\theta & 0 & cos\theta \end{pmatrix} \tag{6.5}$$

$$R_z(\phi) = \begin{pmatrix} cos\phi & sin\phi & 0 \\ -sin\phi & cos\phi & 0 \\ 0 & 0 & 1 \end{pmatrix} \tag{6.6}$$

where θ and ϕ are the polar and azimuthal angles with respect to the photon direction of motion after the boost.

For an arbitrary four momentum $p^* = (E^*, p_x^*, p_y^*, p_z^*)$ in the CMS

$$E_B = \gamma_B(E^* - \beta_B p_z^*) \tag{6.7}$$

$$p_{Bx} = p_x^* \tag{6.8}$$

$$p_{By} = p_y^* \tag{6.9}$$

$$p_{Bz} = \gamma_B(\beta_B E^* - p_z^*) \tag{6.10}$$

where the subscript B is used for quantities in the Breit frame and $\gamma_B = (1 - \beta_B^2)^{-1/2}$, β_B being the relative velocity of the Breit frame with respect to the hadronic CMS. This is given as

$$\beta_B = q^{0*}/q_z^* \tag{6.11}$$

by demanding that the energy of the virtual photon be zero. To derive β_B first we write the four momentum components of the virtual photon in the hadronic CMS (q^*) and the Breit (q_B) frames of reference. These are

$$q^* = \left[\left(\frac{W}{2}\left(\frac{1-2x}{1-x}\right)\right), 0, 0, \left(-\frac{W}{2}\left(\frac{1}{1-x}\right)\right)\right] \tag{6.12}$$

$$q_B = [0, 0, 0, -Q] \tag{6.13}$$

using the conservation laws of energy and momentum and given that the total hadronic mass is W. Note that the photon four vector is invariant in all inertial reference frames, i.e., $q^2 = q^{*2} = q_B^2 = -Q^2$.

Using the equation of β_B given in 6.11 and inserting in it the components of the photon given in equation 6.12, the velocity of the Breit frame with respect to the hadronic CMS is found to be

$$\beta_B = -(1-2x). \tag{6.14}$$

Viewed from the hadronic CMS the photon travels with speed $1-2x$ along the negative z direction. This means that for $x = 0.5$ the two systems coincide.

Figure 6.2 shows the magnitude and direction of the boost that has to be applied to particles in order to change from the laboratory to the Breit frame as a function of x and Q^2 [59]. It can be seen from the figure that for a given value of momentum transfer, the larger x is the larger (smaller) the longitudinal boost required in the negative (positive) z direction. Likewise, for a given value of x, the larger the momentum transfer is the larger

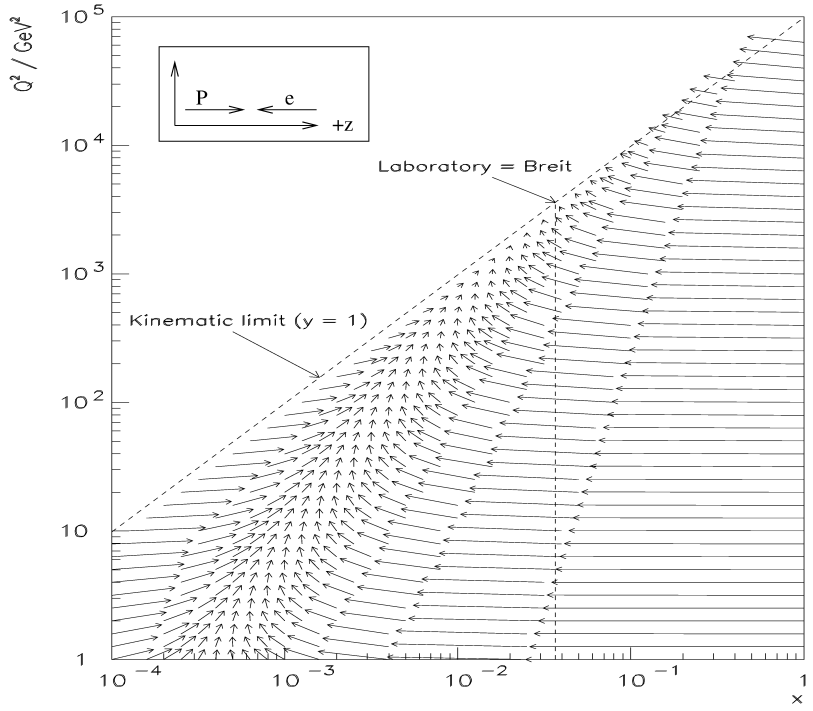

Figure 6.2: A vector of magnitude $\log\gamma$ in the direction of the boost needed to translate from the laboratory to the Breit frame is shown at regular intervals in Q^2 and x. The vertical line represents the value of x (~ 0.03) where the struck parton carries the same momentum as the incident electron.

(smaller) the longitudinal boost required in the positive (negative) z direction. Performing these boosts results in the incident and scattered partons being deflected by 180° (in the QPM scheme), and the incident and scattered electrons having equal energies, which in turn results in an entirely space-like vector boson. The vertical line in the figure represents the value of x (~ 0.03) where the struck parton carries the same momentum as the incident electron ($920 \times 0.03 \approx 27.5$). On this line, when the momentum transfer is small, corresponding to low values of y, both the electron and the parton will only be slightly deflected. When Q^2 is at its maximum ($y = 1$), the two particles will be deflected by 180° and the laboratory system coincides with the Breit frame. However, at this particular values of x and Q^2 the outgoing particles exit down the beam pipe and are therefore not detected.

The advantage of the Breit Frame of reference is that, ideally, in a DIS process all products resulting from the struck quark fragmentation fall into one hemisphere, known as the current region, the remnant of the collision falling into the other one, known as the target region. This property makes it suitable for comparing *ep* collisions boosted to the Breit Frame with e^+e^- annihilations in their centre of mass frame, where E^* is the centre of mass energy. The current region of the Breit frame in principle contains only a quark with a z momentum of $Q/2$, being therefore equivalent to one hemisphere of the $e^+e^- \rightarrow \gamma/Z^o \rightarrow q\overline{q}$ process, which contains only a quark with, if aligned, a z momentum of $E^*/2$. It is common in e^+e^- experiments, as in this thesis, to perform analyses using only the magnitude of the momenta of the outgoing particles.

The following figures are presented in the same fashion as the data quality plots in the previous chapter (points for the data and histograms for Monte

Carlo). The electron method reconstructed distributions for the cosine of the tracks polar angles and for the tracks azimuthal angles relative to the Breit frame are shown in figure 6.3. The points correspond to the H1 data and the histograms to the reconstructed Monte Carlo (DJANGOH13). The positive values of $cos\theta$ correspond to the target hemisphere, where most of the tracks lie. These are associated with the spectator system. The negative values correspond to the current hemisphere, where all the products from the struck quark (ideally) fall. The azimuth is counted from the electron direction by choice and, since the struck quark is supposed to exit along the negative z direction and the proton remnant continues in the positive z direction, it is clear that the ϕ distribution should be flat for a perfectly boosted event. The fact that this distribution is not flat for the data analysed indicates that the boosting procedure was not perfect due to small errors in the reconstruction of kinematic variables. The distribution for the tracks energies and their transverse momenta are shown in figure 6.4, where it can be seen that most tracks are low energetic and have a small transverse component of the momentum.

Figures 6.5 and 6.6 are the equivalent of figures 6.3 and 6.4 but looking only at the current hemisphere of the Breit frame. The only difference is that the distribution for the cosine of the polar angle has been changed for the average charged track multiplicity distribution in figure 6.5, which shows that in this region of phase space low multiplicities are produced.

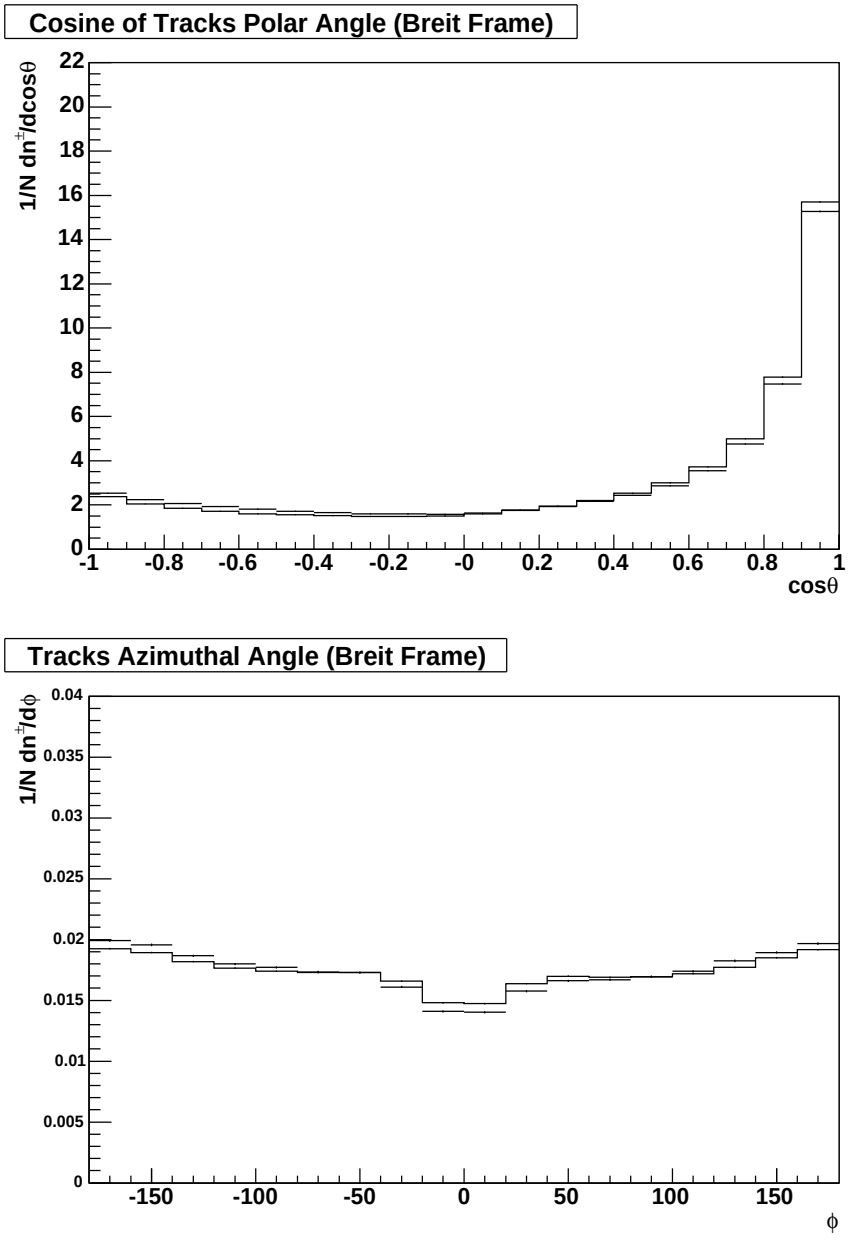

Figure 6.3: Cosine of the polar angle and azimuthal angle distributions for charged tracks in the Breit frame of reference (electron method).

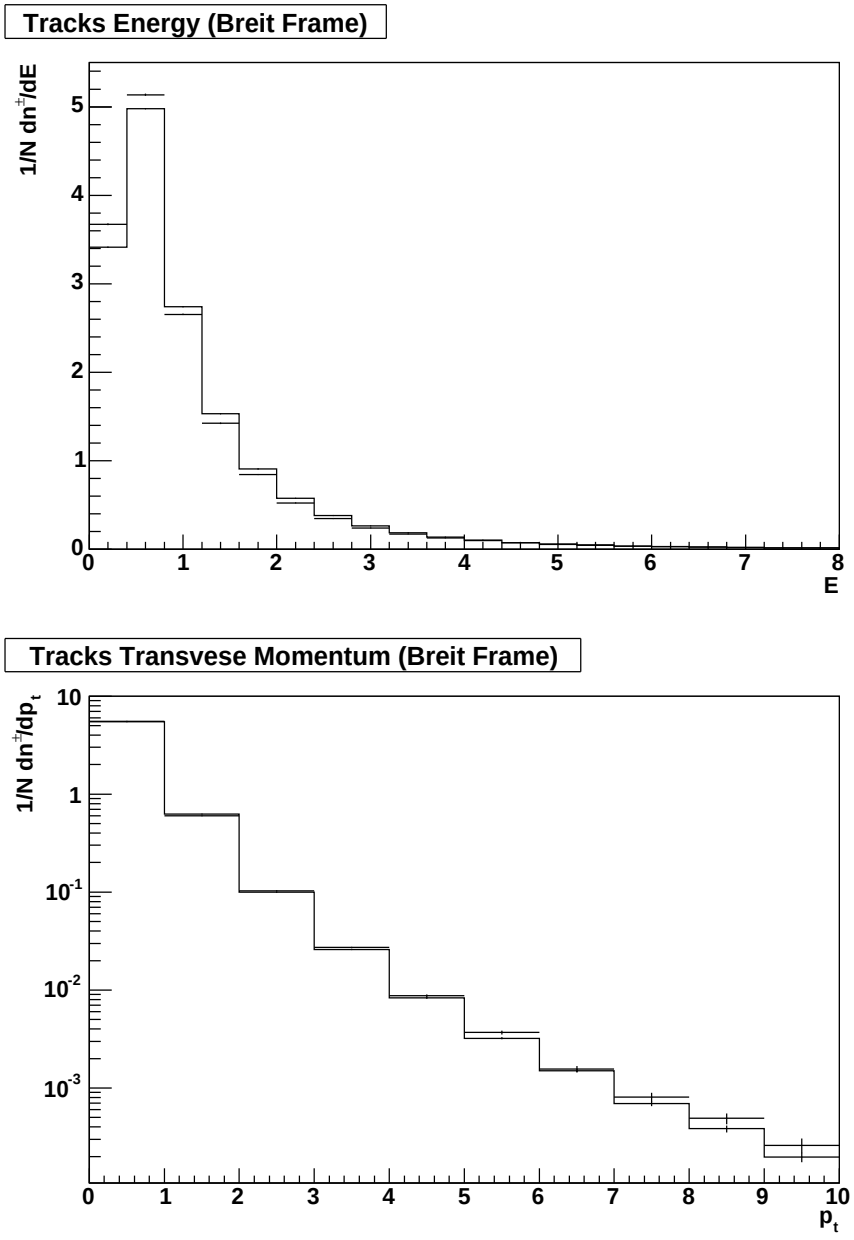

Figure 6.4: Energy and transverse momentum distributions for charged tracks in the Breit frame of reference (electron method).

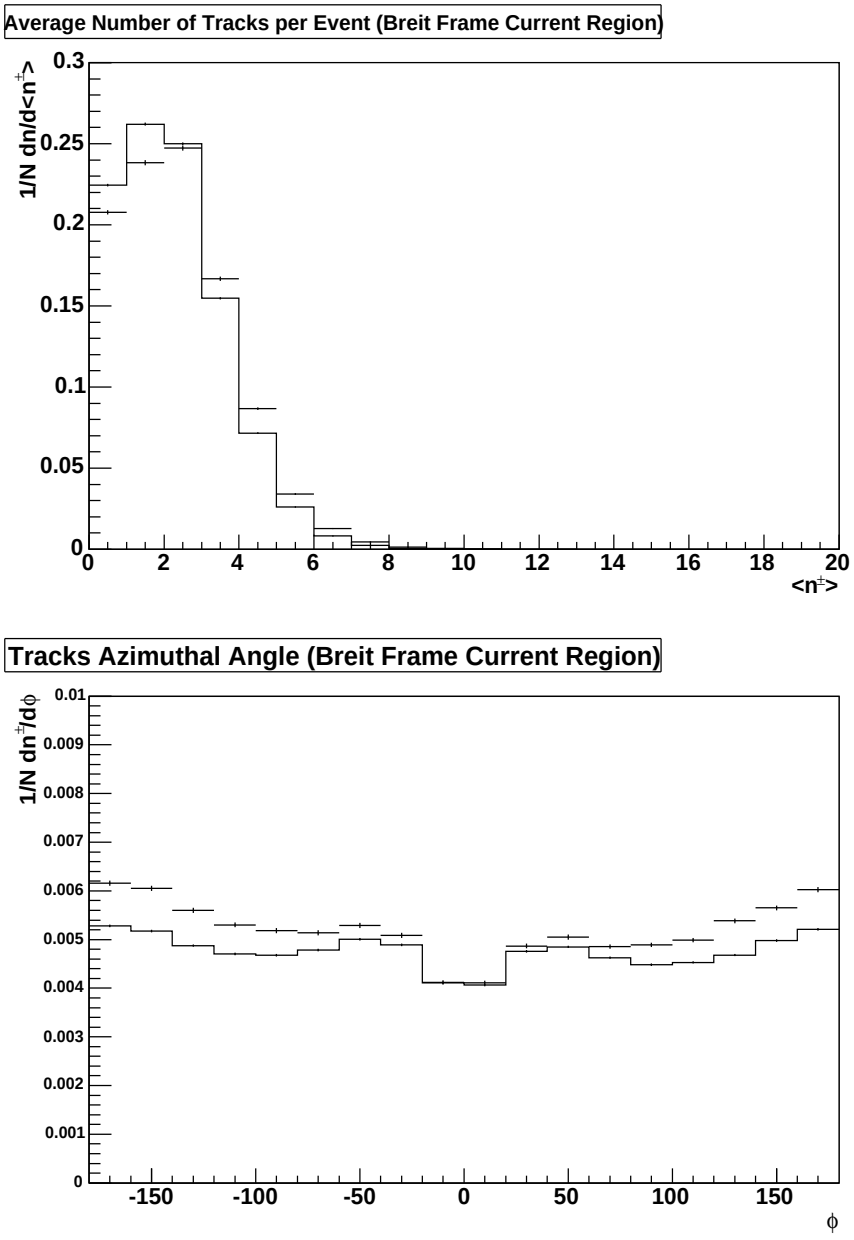

Figure 6.5: Average charged track multiplicity and azimuthal angle distributions for charged tracks in the Breit frame of reference (electron method).

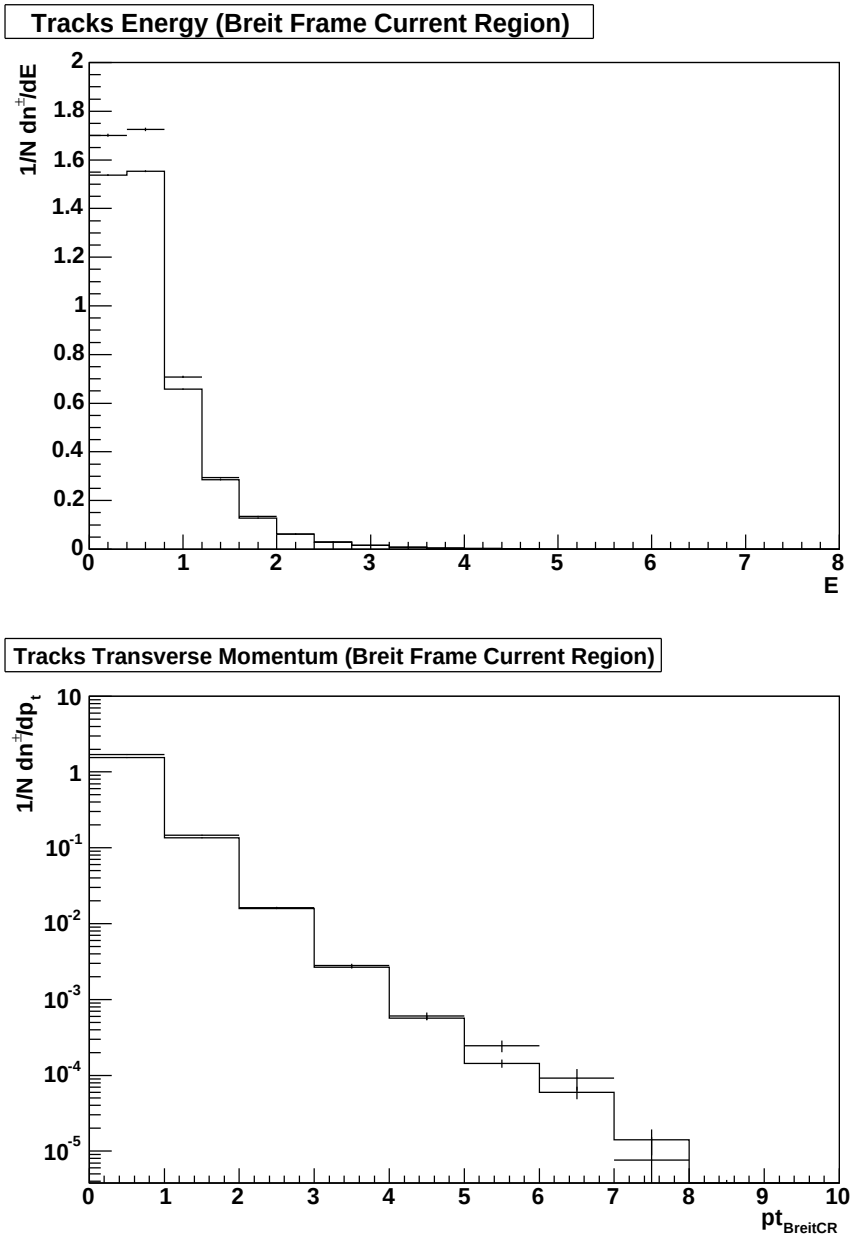

Figure 6.6: Energy and transverse momentum distributions for charged tracks in the Breit frame of reference (electron method).

The following four figures (6.7, 6.8, 6.8 and 6.10) are the double angle method versions of the previous four. The data distributions in these figures are for the most part well described by the Monte Carlo for both reconstruction methods. There are some minor discrepancies when looking at the current region, the biggest of which being in the ϕ distributions. Here the Monte Carlo is modelling the shapes of the data distributions but with different slopes. It should be noted that this distribution is the least important to this analysis.

6.2 The Fragmentation Function

Naively, it would be reasonable to assume the fragmentation of a quark to be independent of the process by which the quark was created. This is known as quark fragmentation universality. A natural result of this assumption is that the distributions of variables related to quark fragmentation look the same for a quark coming from an $e^+e^- \rightarrow q\overline{q}$ process and for the struck quark from an ep process. The most important such variable is the fraction of the quark momentum carried by the hadrons that are produced from it. The name chosen for this variable is x_p, since it relates the hadrons to the (parent) quark in the same way as x_{Bj} relates the quarks to the proton:

$$x_p = 2p_h/Q. \tag{6.15}$$

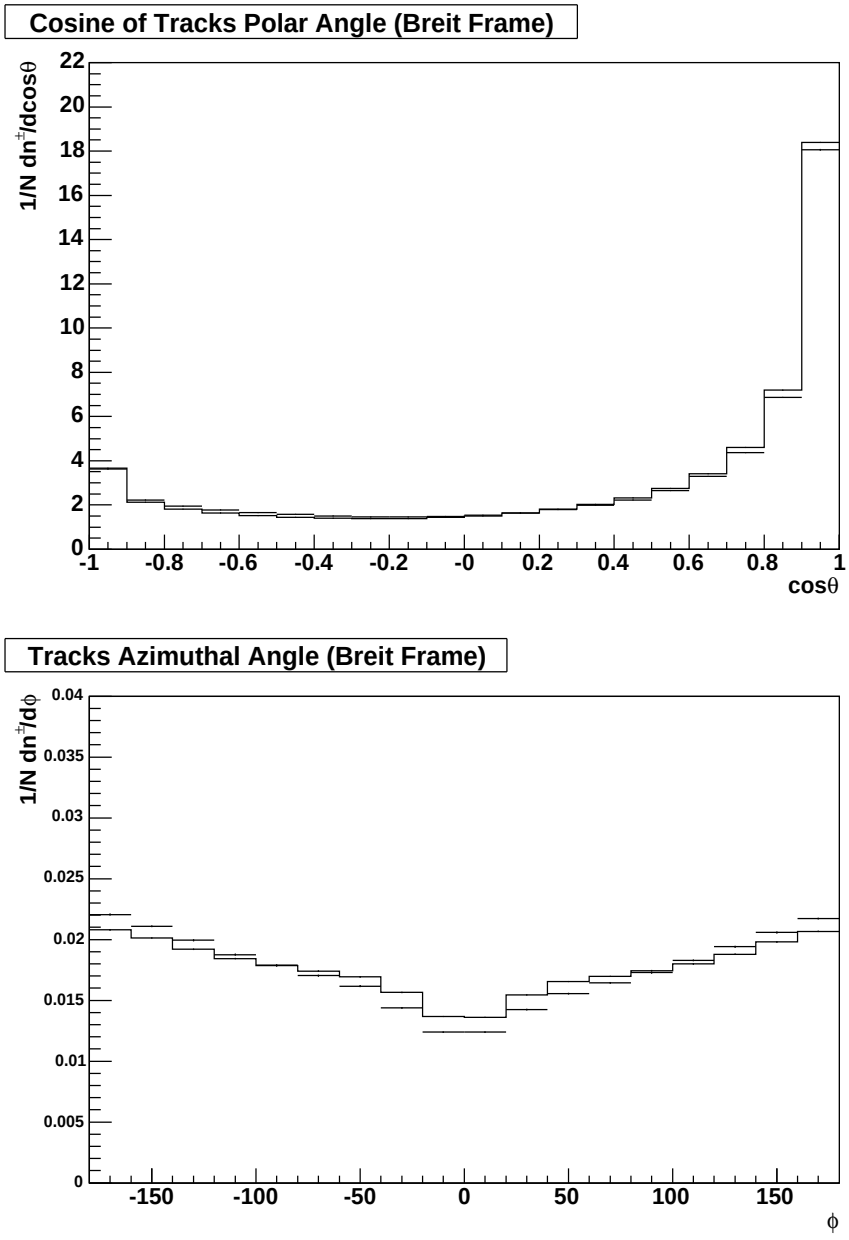

Figure 6.7: Cosine of the polar angle and azimuthal angle distributions for charged tracks in the Breit frame of reference (double angle method).

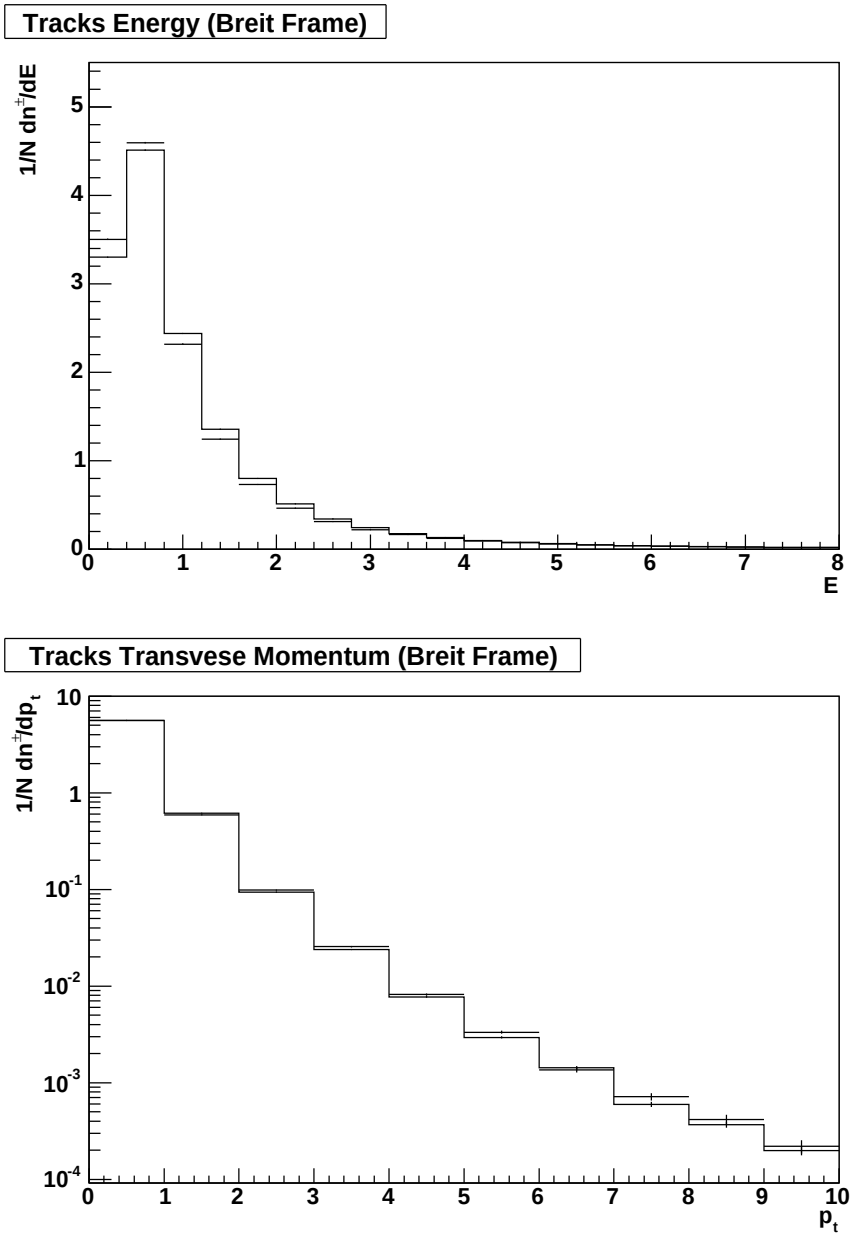

Figure 6.8: Energy and transverse momentum distributions for charged tracks in the Breit frame of reference (double angle method).

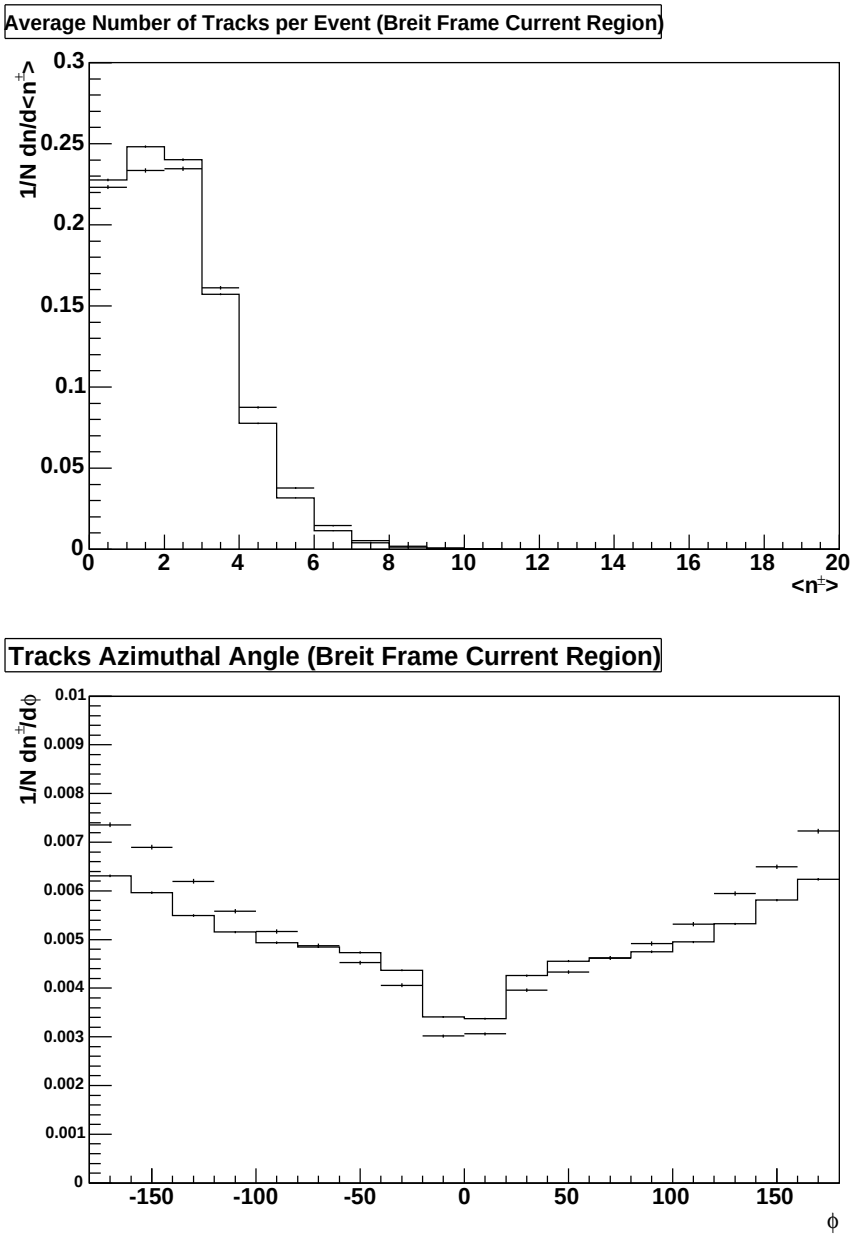

Figure 6.9: Average charged track multiplicity and azimuthal angle distributions for charged tracks in the Breit frame of reference (double angle method).

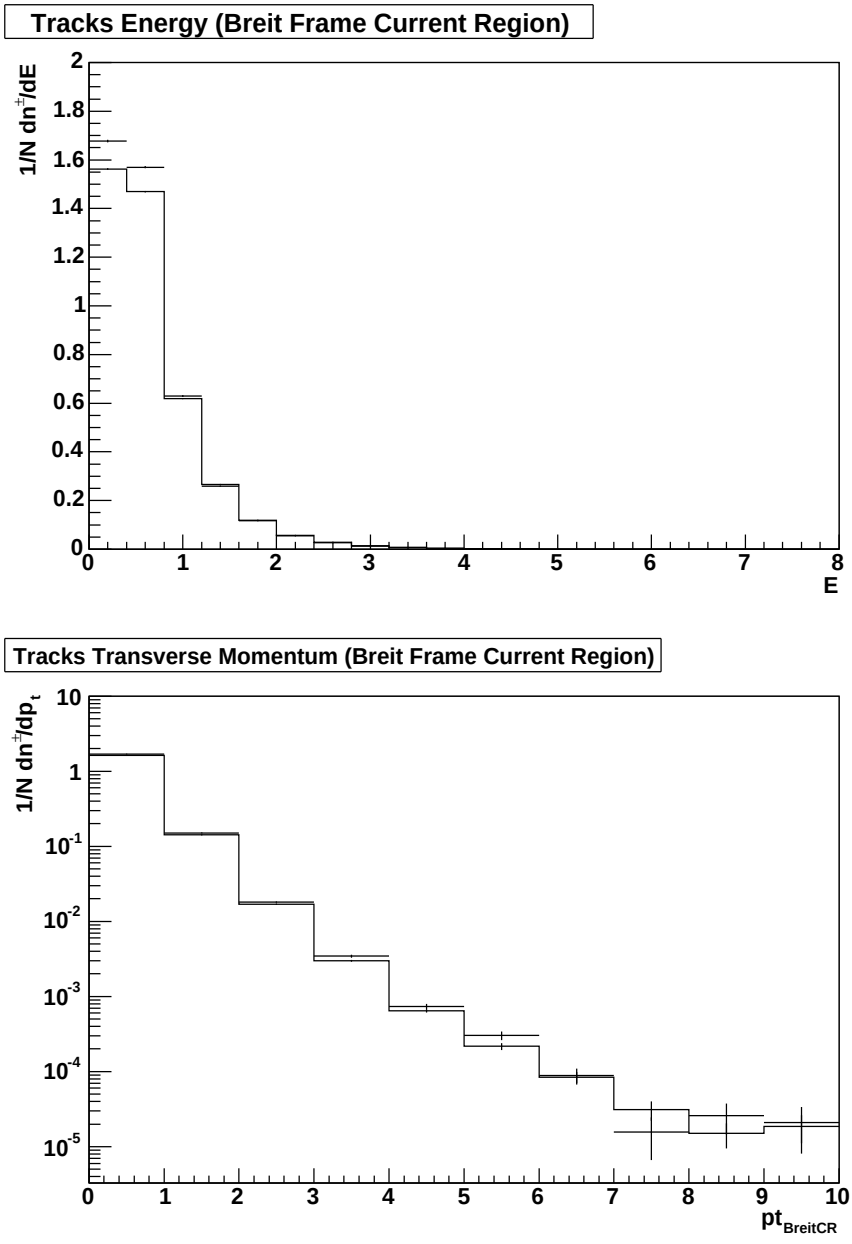

Figure 6.10: Energy and transverse momentum distributions for charged tracks in the Breit frame of reference (double angle method).

The average charged multiplicity expressed as a function of x_p and Q (equivalent to centre of mass energy E^* for the e^+e^- data) is known as the fragmentation function and is written as:

$$D^{\pm}(x_p, Q) = \frac{1}{N}\frac{d^2n^{\pm}}{dx_p dQ} \tag{6.16}$$

The comparison of the fragmentation function for the data used in this thesis and for e^+e^- data [60], derived from [61], are shown in figure 6.11. There is good agreement between the two samples in the high Q, high x_p region, but in the low Q, low x_p region there is a large discrepancy. The low Q region is shown in more detail in figure 6.12, in which 1996-97 H1 data [62] and DJANGOH13 predictions are also shown to illustrate the level of agreement with the analysed data in this thesis. Here, the lowest x_p histograms show a large difference between the e^+e^- and the ep data samples in the lowest Q region. As x_p increases (meaning fewer particles sharing a bigger fraction of the quark's momentum) the average multiplicity drops for both the e^+e^- and ep samples (see figure 6.13). The difference between them is also reduced as x_p increases (see figure 6.11). Note that the e^+e^- points are from a different experiment each. The e^+e^- curve is thus subject to additional systematic errors.

It can clearly be seen from figure 6.13 that there is a $(log)Q$ dependence of the fragmentation function. The cause of these scaling violations of the fragmentation function is essentially the same as the cause for the structure function F_2 scaling violations (see section 2.5.3). Again, it can be seen in two equivalent ways. One is to say that the higher the energy of the collision the more hadrons (with lower x_p) can be produced. The other is to say that low x_p hadrons are always there, but the momentum of the probe (Q^2),

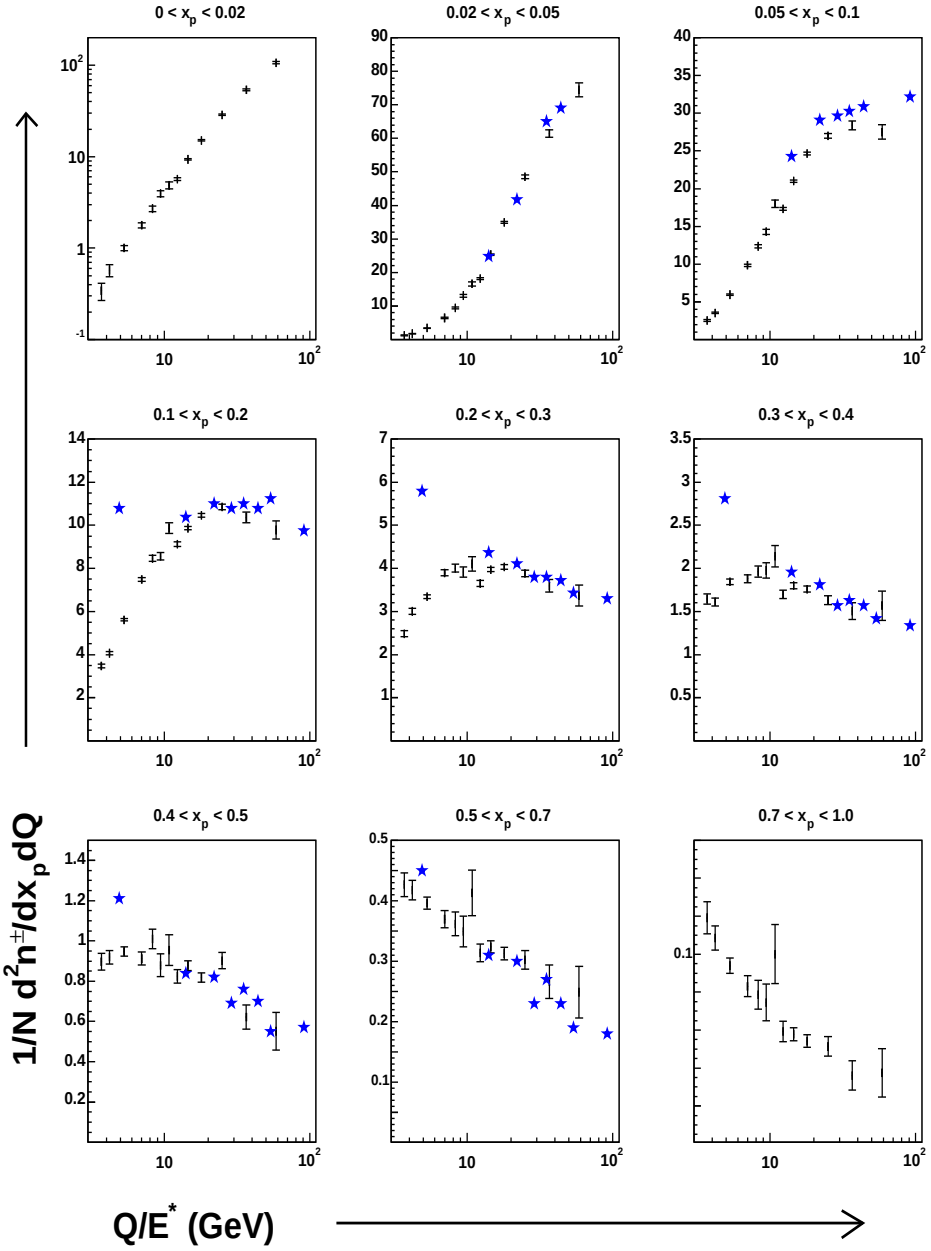

Figure 6.11: Distributions of x_p as a function of Q (equivalent to E^* for e^+e^-). Shown are the year 2000 H1 (points) and e^+e^- (stars) data samples for both the low energy (analysed data) and high energy [60] (from 12 GeV upwards) regions. The samples include statistical errors only.

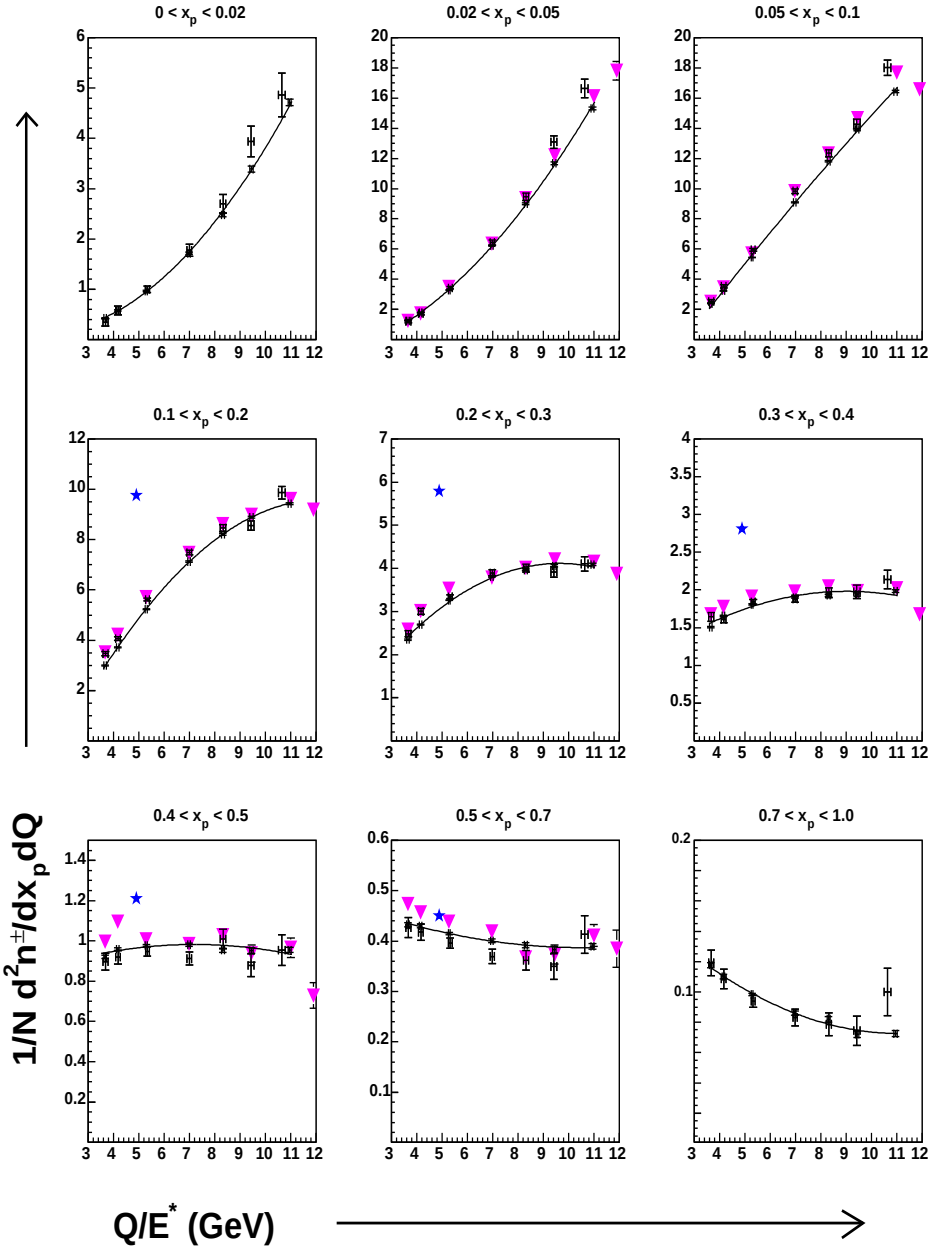

Figure 6.12: Low Distributions of x_p as a function of Q (equivalent to E^* for e^+e^-) for the low Q region. Shown are the year 2000 H1 (points), the years 1996/97 H1 (triangles), DJANGOH13 points, fitted with 2nd degree polynomials, and e^+e^- (stars) data samples. The samples include statistical errors only.

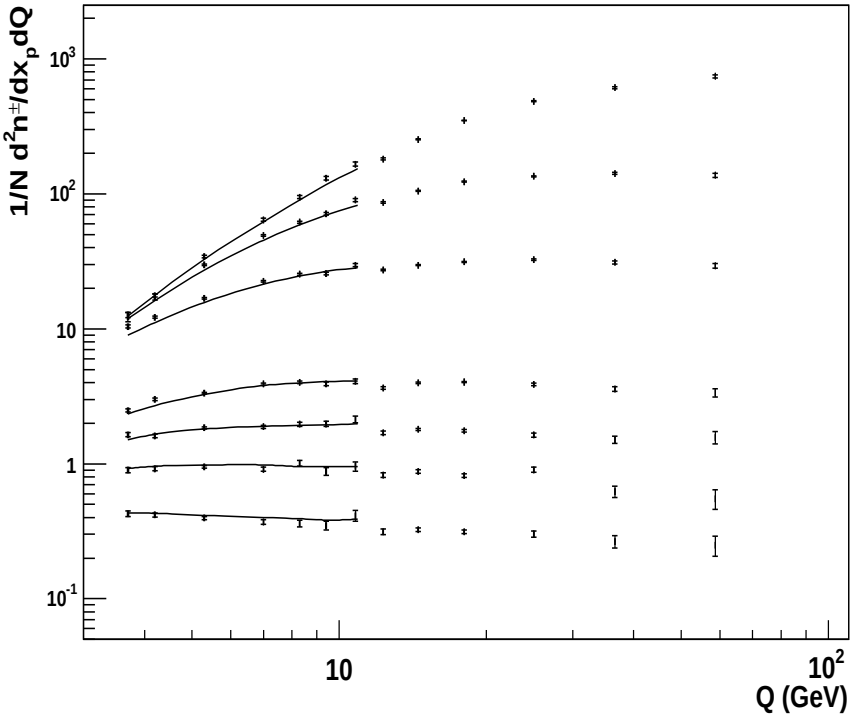

Figure 6.13: Data distributions of x_p from figure 6.11 combined in a single plot. from top to bottom, the lines correspond to the following x_p bins: 0.02-0.05($\times$10), 0.05-0.1($\times$5), 0.1-0.2($\times$3), 0.2-0.3, 0.3-0.4, 0.4-0.5 and 0.5-0.7. The low Q, DJANGOH13 predictions have been included to guide the eye.

which sets the factorisation scale, dictates what is resolvable and which is not [1]. Again, both of these views result in an increase (decrease) in the number of low (high) momentum partons at large Q^2. To see the effect of the scaling violations on the fragmentation function, which is the same as that observed in the behaviour of F_2, the data from figure 6.11 have been combined in a similar fashion as the F_2 data in figure 6.13.

Of course in *ep* collisions there are initial-state, leading order QCD processes (see next section) not present in e^+e^- processes, these being Boson-Gluon Fusion (BGF) and Initial-state Compton QCD (ICQCD). These QCD processes can produce a depopulation of the current region of the Breit frame, and even result in an empty current hemisphere. Actually, any kind of DIS event can result in an empty current hemisphere, since neutral tracks are not "seen" by the trackers, and an event with (by coincidence) only tracks of this kind in this region is counted as an empty current hemisphere event. Therefore what is meant here is that taking into account these leading order QCD processes results in an increase in this type of events. Final state Compton QCD (FCQCD), which also occurs in e^+e^- collisions, does not result as much in empty current hemisphere events for DIS, since the initial state is identical as that of a QPM event, i.e., with the struck quark exiting in the direction of negative z with no transverse momentum.

The fraction of empty current hemisphere events is an important quantity in this thesis, as it is later used as a means to determine the fraction of gluon initiated events (see section 7.1). The essential difference between *ep* and e^+e^- collisions is that, whereas in DIS events whatever goes outside the current region of the Breit frame is lost, in e^+e^- both hemispheres are used,

[1] this is equivalent to saying that at low energies there is a higher probability to measure the wave function as a single hadron rather than as two distinct particles with a small angle between them.

since they are equivalent. Whatever is lost in one hemisphere is gained in the other. This means that no final-state process can produce any net loss of tracks.

The histograms (bins) with no electron-positron data in figures 6.11 and 6.12 were not kinematically accessible for the e^+e^- experiments since hadrons with such low momenta in the lab frame could not be detected. This is an advantage of the *ep* experiments performed at HERA, as the boost performed allows for hadrons of arbitrarily low momenta in the Breit frame (these can have large enough momenta in the lab frame to be measured). For the ones accessible by the e^+e^- experiments, the lowest ones ($0.1 < x_p < 0.2$ and $0.2 < x_p < 0.3$) show that this data set has twice as many charged tracks as the *ep* DIS data. It is reasonable to expect this difference to be due to these leading order QCD processes. The loss of tracks in the lowest Q region can be explained by saying that in ICQCD and BGF events, the struck quark, which has a sizable transverse component of the momentum (see figure 6.17 in the next section) will get closer to the target region as Q decreases, since it will be getting smaller boosts in the negative z direction. The decrease in the discrepancy between the e^+e^- and *ep* samples at high x_p can then be explained by noting that, as x_p gets large there is a small number of hadrons sharing the quark's momentum. This leads to a suppression of QCD splitting processes, since these produce more hadrons, often in events with two distinct jets, than the simpler QPM processes with fewer hadrons and single jet events. Figures 6.14 and 6.15 show a clear one jet (QPM) event and a clear dijet (LOQCD) event respectively.

Candidate from NC sample

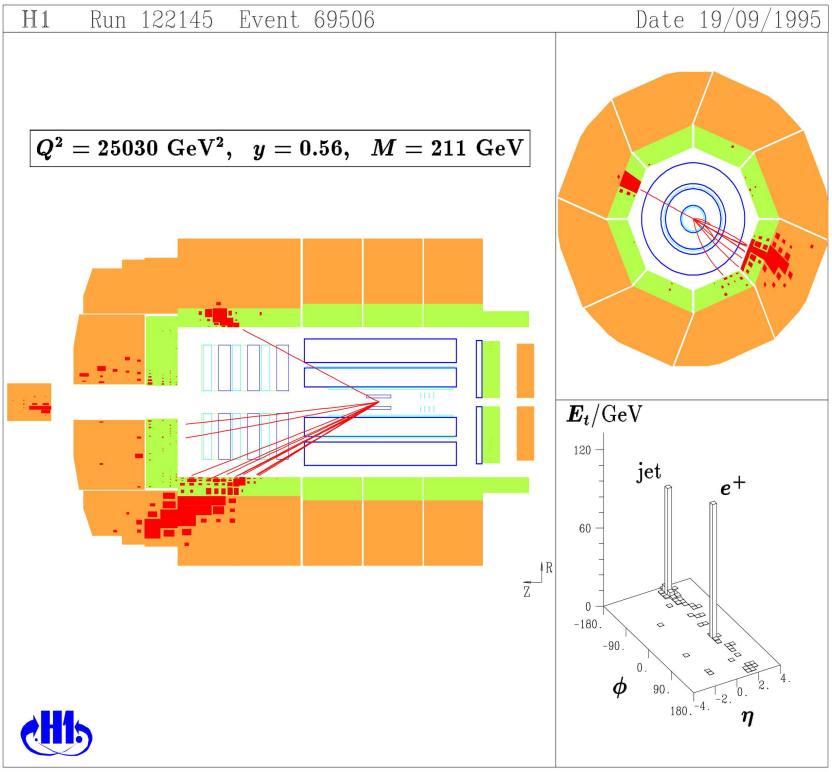

Figure 6.14: H1 event display of a high Q^2, QPM event. A single jet originating from the struck quark can be seen in the lower part of the detector. The edges of the jet originating from the (coloured) proton spectator system can be seen in the forward region surrounding the beam pipe. The electron is picked up in the upper region of the detector. Shown are the transverse and front views of the detector and a ϕ/η (azimuthal angle/pseudo-rapidity) histograms showing the position of the jet.

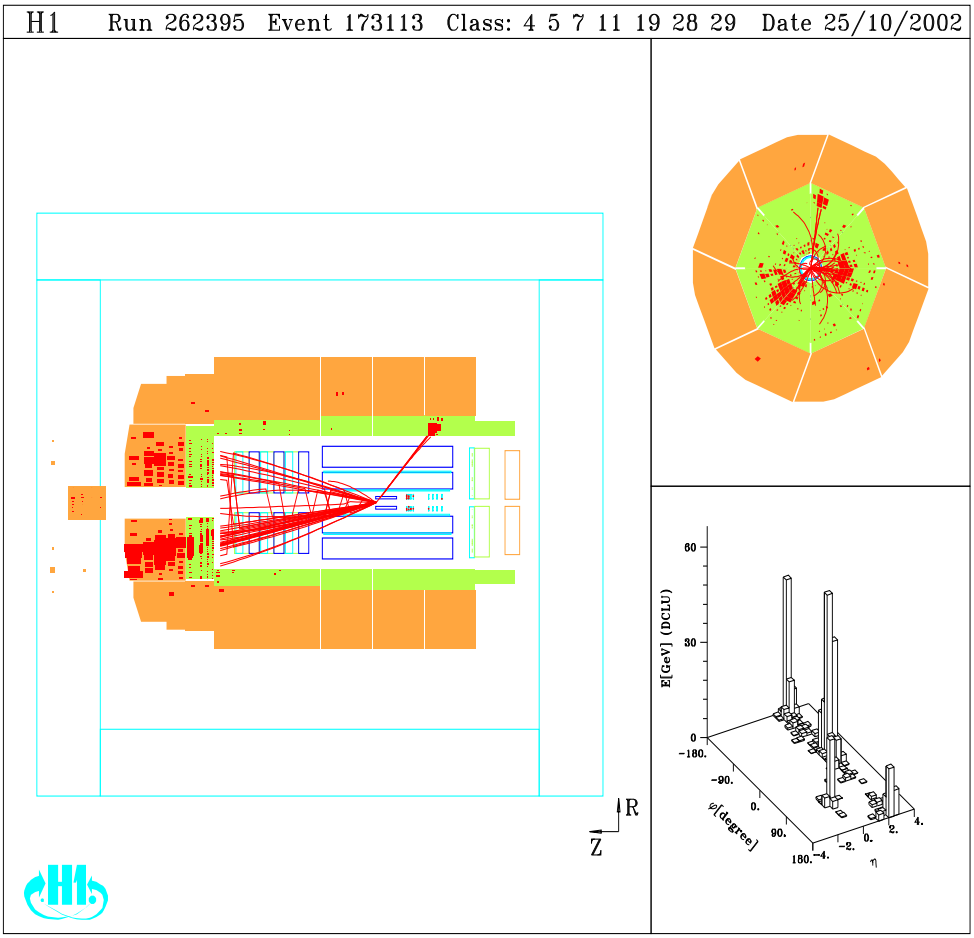

Figure 6.15: H1 event display of a high Q^2, leading order QCD event. The two jets originating from each of the partons resulting from the leading order QCD process can be seen in the forward part of the detector. The electron is picked up in the backward region of the detector. Shown are the transverse and front views of the detector and a ϕ/η (azimuthal angle/pseudo-rapidity) histograms showing the positions of the jets.

6.3 Leading Order QCD Processes

The above discussion of the QPM scheme in the Breit frame is modified when leading order QCD processes are taken into account. These are the already mentioned boson-gluon fusion and Compton QCD. In BGF an incident gluon splits into a quark-antiquark pair above the QCD factorisation scale. One of these quarks is struck by the exchanged boson and the other goes into the target hemisphere. In ICQCD the struck quark emits a gluon transferring some of its momentum to it and then interacts with the electron. The lower Q is the larger α_s and so the more likely to get parton splitting. This is correlated with low x since, the lower x is the more likely is the quark to have come from a split incident parton. In both cases the momentum of the quark struck by the boson (related to the x value of the event) is no longer in the z direction, since, due to the splittings, it acquires a transverse momentum. Because these daughter quarks have a smaller (positive) longitudinal momentum than their parent particle and a (sizable) transverse momentum, they are more likely to produce an empty current hemisphere than quarks not undergoing these leading order QCD processes.

In FCQCD a quark interacts with the photon and then emits a gluon, resulting in a loss of (negative) longitudinal momentum and in a gain of transverse momentum. Simple classical analogues have been made in the above argument. It is a quantum-mechanical fact that ICQCD and FCQCD are not really time ordered, but just the two peaks of the bimodal CQCD wavefunction, one in which the gluon goes into the target region (ICQCD), the other with the gluon going into the current region (FCQCD). For illustrative purposes these leading order QCD processes are shown in figure 6.17, as viewed from the Breit frame of reference.

It is possible to divide an inclusive sample of Monte Carlo generated events into two subsamples, one containing only gluon initiated events (BGF), the other containing the remaining quark initiated events (CQCD and QPM). Average charged track multiplicities are shown in figure 6.18 using a sample of events generated with the Monte Carlo program DJANGOH13 (with the CDM fragmentation model and the CTEQ5L parton density function) and boosted to the Breit frame of reference. It is clear from this figure that the gluon sample produces a much higher fraction of empty current hemisphere events than that of the quark sample. This is due to the fact that, even though ICQCD can produce as many empty current hemisphere events as BGF, it cannot be isolated from FCQCD, since, as mentioned above, they are just the two modes of the same CQCD wave function. Furthermore, CQCD cannot be completely isolated from the QPM diagram, since they are both quark initiated processes. An increase in the number of quarks going into the PDF will therefore result in an increase in CQCD events (initial and final-state by the same amount), and clearly in QPM events as well. The gluon sample is independent of the others, and therefore an increase in the number of gluons leads to an (independent) increase in the fraction of empty current hemisphere events.

The principal aim of this analysis is to try to constrain the gluon density functions since, gluons being electrically neutral, they are less well determined than the quark density functions (see figure 6.16). Average charged track multiplicity histograms are shown in figure 6.19 for two DJANGOH13 (CDM) samples at the generated level, one using CTEQ5L and the other MRSG (see section 2.6). An 8% difference can be observed in the fraction of empty current hemispheres between the two samples, which is a large enough difference to give hope for constraining these PDFs (see next chapter).

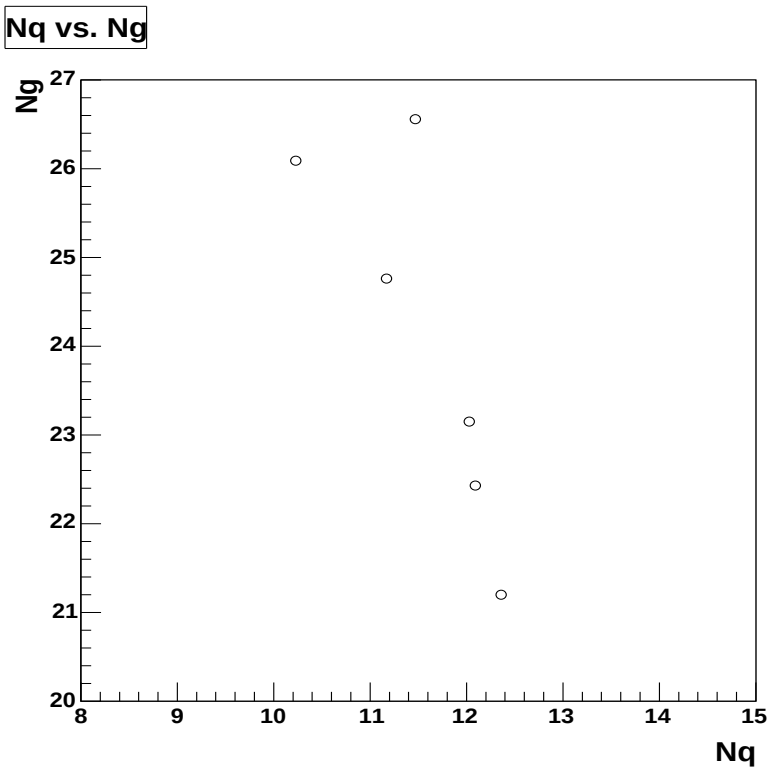

Figure 6.16: The number of quarks (horizontal axis) and the number of gluons (vertical axis) predicted by six different parton density functions. From left to right these are: GRV98, ALEKHIN, CTEQ5L, H12000, MRSG and ZEUS2005. Since quarks are charged particles, their number is much better determined than the number of gluons, which are neutral.

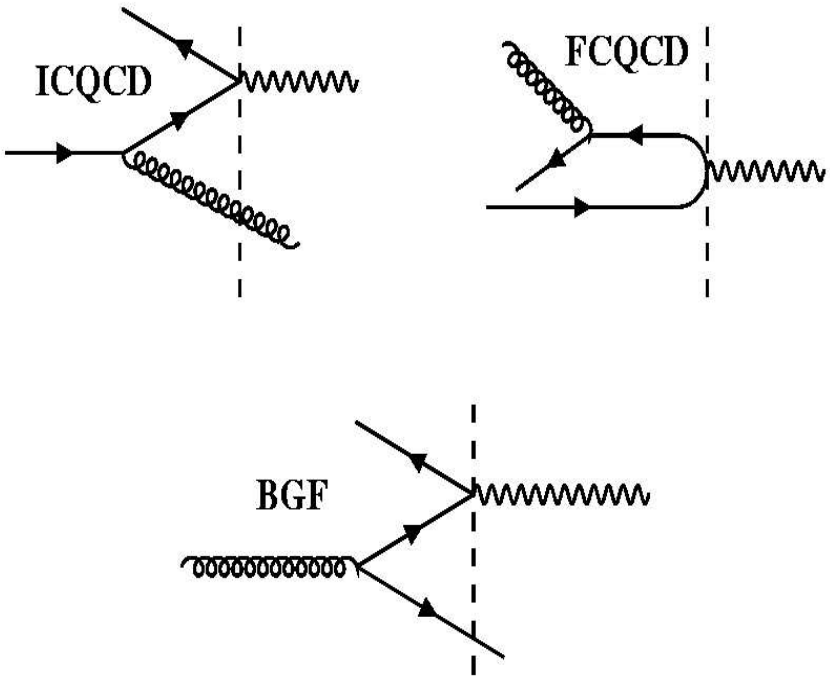

Figure 6.17: Events containing the leading order QCD processes ICQCD (top-left), FCQCD (top-right) and BGF (bottom), and boosted to the Breit fame of reference. The current hemisphere is to the left of the dashed lines, the target one to the right.

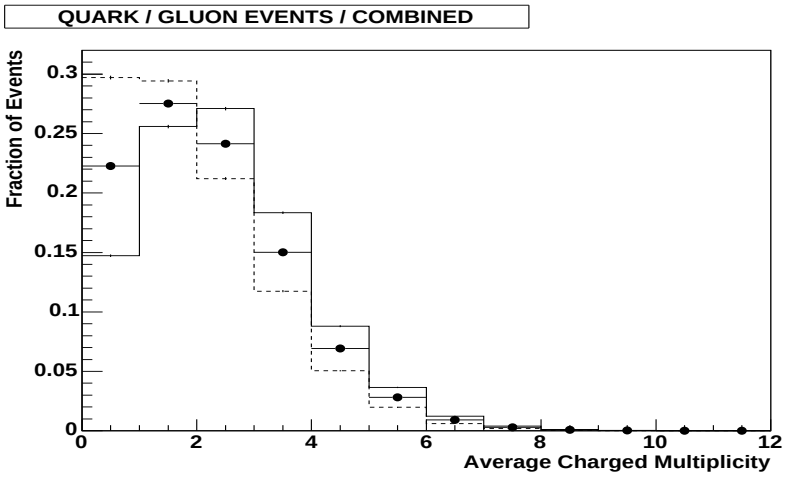

Figure 6.18: Average charged track multiplicities for a Monte Carlo (DJANGOH13, CDM, CTEQ5L) sample of events at the generated level (points) with its two subsamples: the gluon initiated events (dashed histogram) and the quark initiated events (solid histogram).

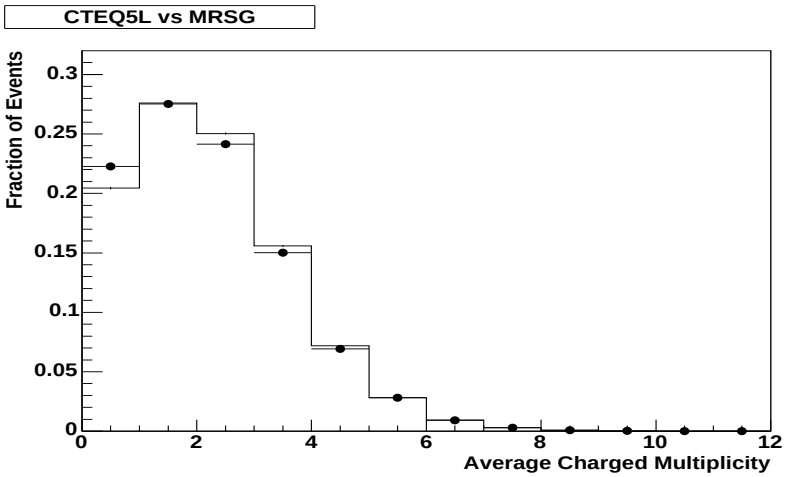

Figure 6.19: Average charged track multiplicities for two Monte Carlo (DJANGOH13, CDM) samples of events at the generated level, one using CTEQ5L (points), the other using MRSG (histogram).

Chapter 7

Determination of the fraction of gluon initiated events

Using the theoretically predicted behaviour of the pure gluon initiated (BGF) and the pure quark initiated ($\overline{BGF}$) Monte Carlo samples, it is possible to determine the fraction of gluon initiated events (f_{BGF}) in the corrected data sample. In turn, this can be used to constrain the gluon density functions. Although these studies were only carried out in leading order QCD, the method presented is completely different from those in other analyses [63, 64], and is therefore an independent determination of the gluon density in the proton.

7.1 Determining f_{BGF}

There are two variables related to the loss of tracks in the current region of the Breit frame that can be used for this purpose. These are the fraction of empty current hemisphere events (f_{ECH}) and the average charged multi-

plicity ($\overline{n}^{\pm}$). The values that these variables take for the two Monte Carlo samples are shown in table 7.1 for four different phase space regions. It is clear from the table that the samples are more sensitive to the fraction of empty current hemisphere events for most of the phase space, so this has been the variable chosen for the analysis. By using this fraction for each of the samples it is possible to get a value for the fraction of gluon initiated events that the data should have had:

$$f_{BGF} = \frac{CD - \overline{BGF}}{BGF - \overline{BGF}} \tag{7.1}$$

where CD is the fraction of empty current hemisphere events in the corrected data event sample, and BGF ($\overline{BGF}$) the corresponding fraction for the "gluon" ("quark") sample for a given Monte Carlo calculation. The fractions of empty current hemisphere events, as derived using the electron reconstruction method, for the corrected data and the Monte Carlo (DJANGOH13, CDM, CTEQ5L) samples with and without BGF events are shown in figures 7.1 and 7.2, as a function of Q^2 for the different x bins, and as a function of x for the different Q^2 bins respectively. The fractions of gluon initiated events are shown in the same format in figures 7.3 and 7.4, for the corrected data and the Monte Carlo (DJANGOH13, CDM) samples with PDFs CTEQ5L and MRSG. A straight line has been fitted through the data points. From these figures it can be seen that, although the fraction of gluon initiated events is almost constant around 50% throughout all Q^2 and x ranges, the fraction of empty current hemispheres increases for decreasing Q^2 values. This is in support of the explanation given in chapter 6 in which the struck quark gets a smaller boost in the negative z direction. The figures also show the analysed data being closer to the MRSG predictions.

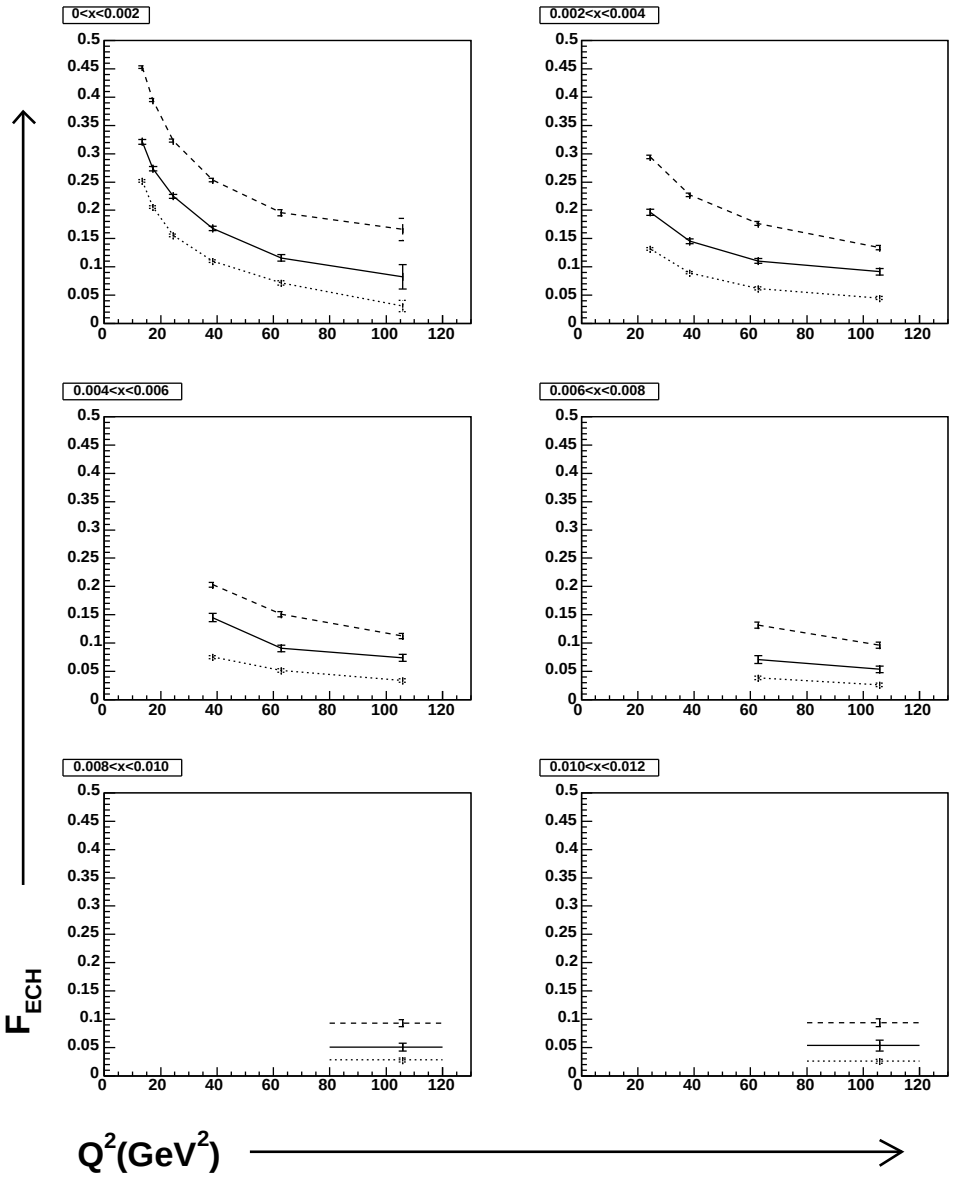

Figure 7.1: Fraction of events with an empty current hemisphere when boosted to the Breit frame of reference, as a function of Q^2 for six different x_{Bj} bins. Shown are the corrected data sample (solid line), and generated Monte Carlo (DJANGOH13, CDM, CTEQ5L) samples with only BGF events (dashed line) and without them (dotted line). (Electron method).

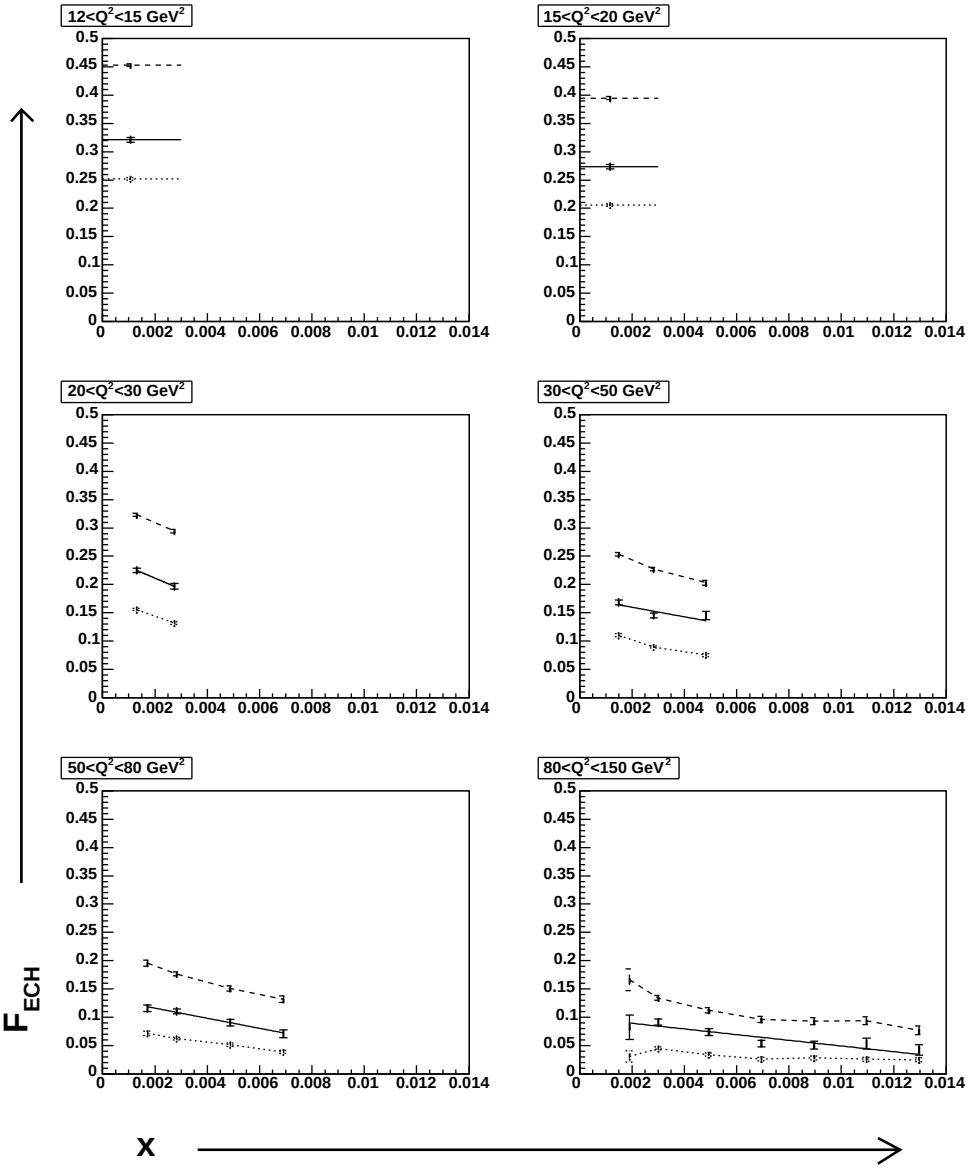

Figure 7.2: Fraction of events with an empty current hemisphere when boosted to the Breit frame of reference, as a function of x_{Bj} for six different Q^2 bins. Shown are the corrected data sample (solid line), and generated Monte Carlo (DJANGOH13, CDM, CTEQ5L) samples with only BGF events (dashed line) and without them (dotted line). (Electron method).

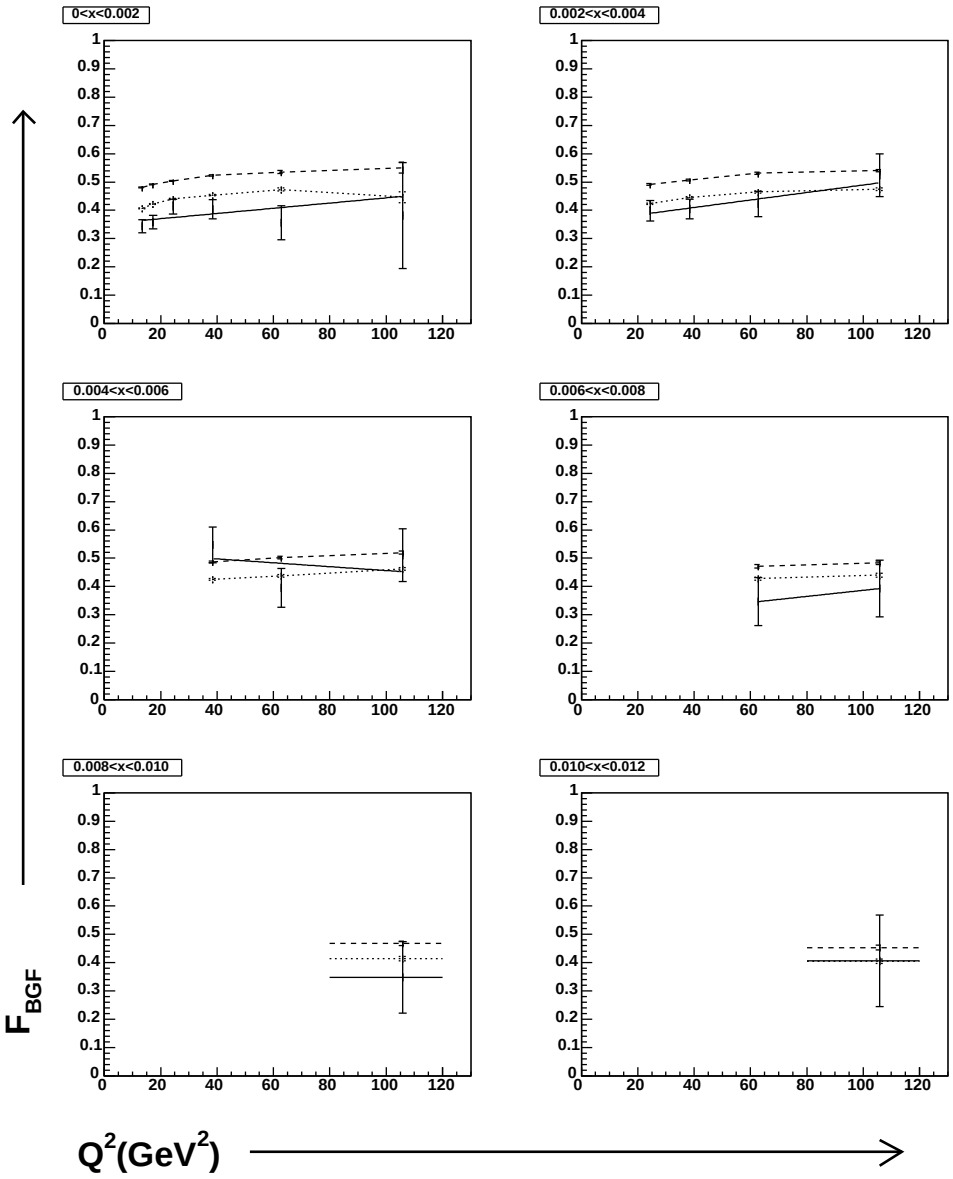

Figure 7.3: Fraction of gluon initiated events (BGF) derived from the fraction of empty current hemisphere events, as a function of Q^2 for six different x_{Bj} bins. Shown are the corrected data sample (solid line), and generated Monte Carlo samples (DJANGOH13, CDM), with two different PDFs: CTEQ5L (dashed line) and MRSG (dotted line). (Electron method).

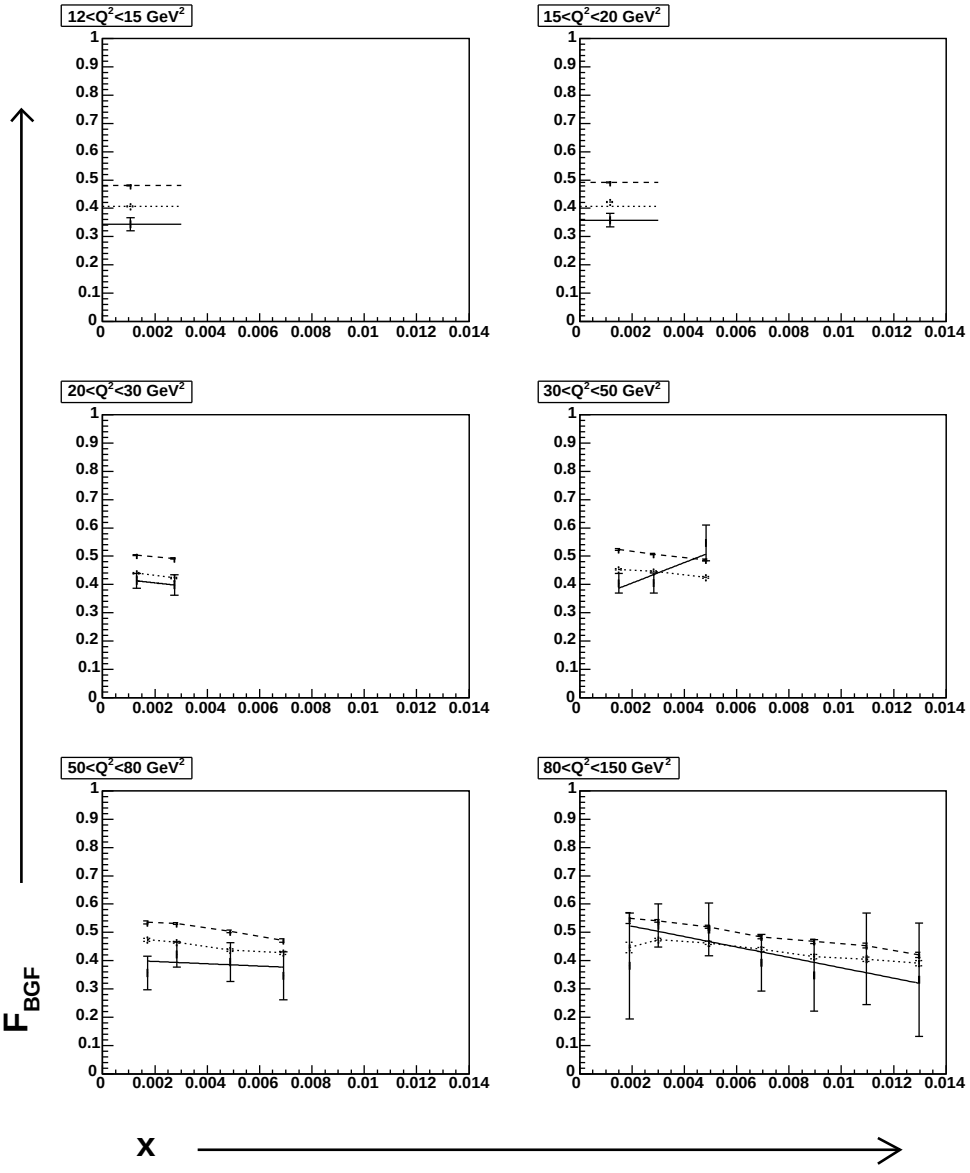

Figure 7.4: Fraction of gluon initiated events (BGF) derived from the fraction of empty current hemisphere events, as a function of x_{Bj} for six different Q^2 bins. Shown are the corrected data sample (solid line), and generated Monte Carlo samples (DJANGOH13, CDM), with two different PDFs: CTEQ5L (dashed line) and MRSG (dotted line). (Electron method).

The following four figures (7.5, 7.6, 7.7 and 7.8) are the double angle method versions of the previous four. The values for the fraction of empty current hemisphere events are summarised in table 7.2. These show that the two methods of reconstruction are generally compatible.

Figures 7.9 and 7.10 contain the correction factors (see section 5.2) for the fraction of empty current hemisphere events for the electron method and double angle method analyses respectively, as a function of x, for six different Q^2 bins. The factors are mostly within the 10% mark, except for the highest Q^2 bins, which are the ones with lowest statistics. Overall they result in a correction factor of 0.09 for the central values in both analyses.

It might seem strange that the fraction of gluon initiated events is close to 50% throughout the whole of the phase space, since at low values of Q^2 (i.e. low x) there are many more gluons than quarks (see figure 7.11). However, the leading order QCD term in equation 2.24 contains an integral over the five quark flavours, as well as over the gluons. The limits of integration

	LoQ, LoX	LoQ, HiX	HiQ, LoX	HiQ, HiX
FECH$_{BGF}$(%)	36.0 ± 0.3	23.0 ± 0.7	18.2 ± 0.3	13.0 ± 0.3
FECH$_{\overline{BGF}}$(%)	18.3 ± 0.2	9.0 ± 0.4	6.8 ± 0.2	4.3 ± 0.1
D(FECH)	53.9	18.4	29.3	27.0
$\overline{n}^{\pm}_{BGF}$	1.08 ± 0.01	1.52 ± 0.02	2.01 ± 0.02	2.32 ± 0.02
$\overline{n}^{\pm}_{\overline{BGF}}$	1.63 ± 0.01	2.11 ± 0.03	2.67 ± 0.02	2.94 ± 0.02
D($\overline{n}^{\pm}$)	57.6	15.2	22.3	19.5

Table 7.1: Values of the fraction of empty current hemisphere events and of the average charged multiplicity for the quark and gluon Monte Carlo subsamples, along with the difference (D) between them in terms of standard deviations. The low Q^2 bin goes up to 40 GeV^2, and the low x bin up to 0.004.

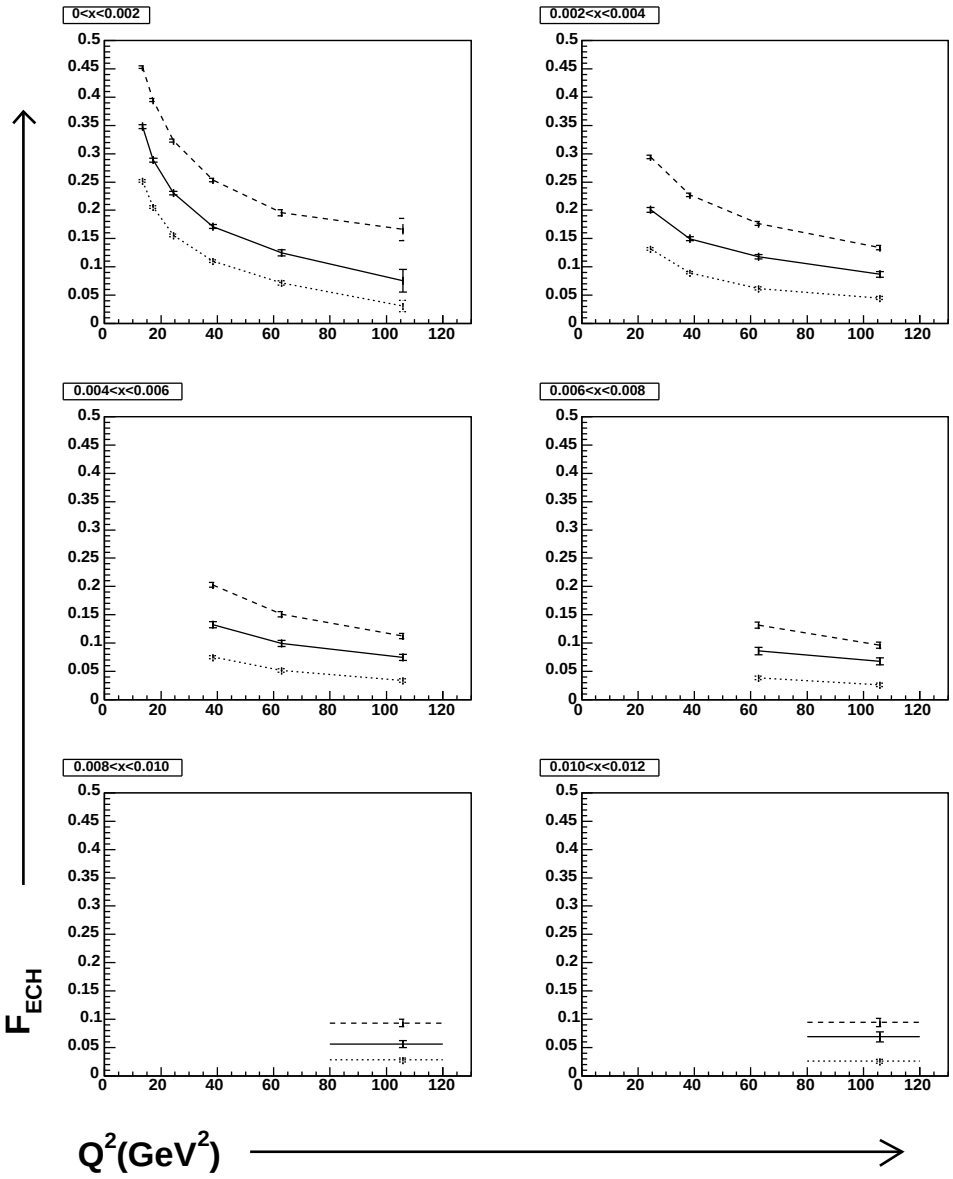

Figure 7.5: Fraction of events with an empty current hemisphere when boosted to the Breit frame of reference, as a function of Q^2 for six different x_{Bj} bins. Shown are the corrected data sample (solid line), and generated Monte Carlo (DJANGOH13, CDM, CTEQ5L) samples with only BGF events (dashed line) and without them (dotted line). (Double angle method).

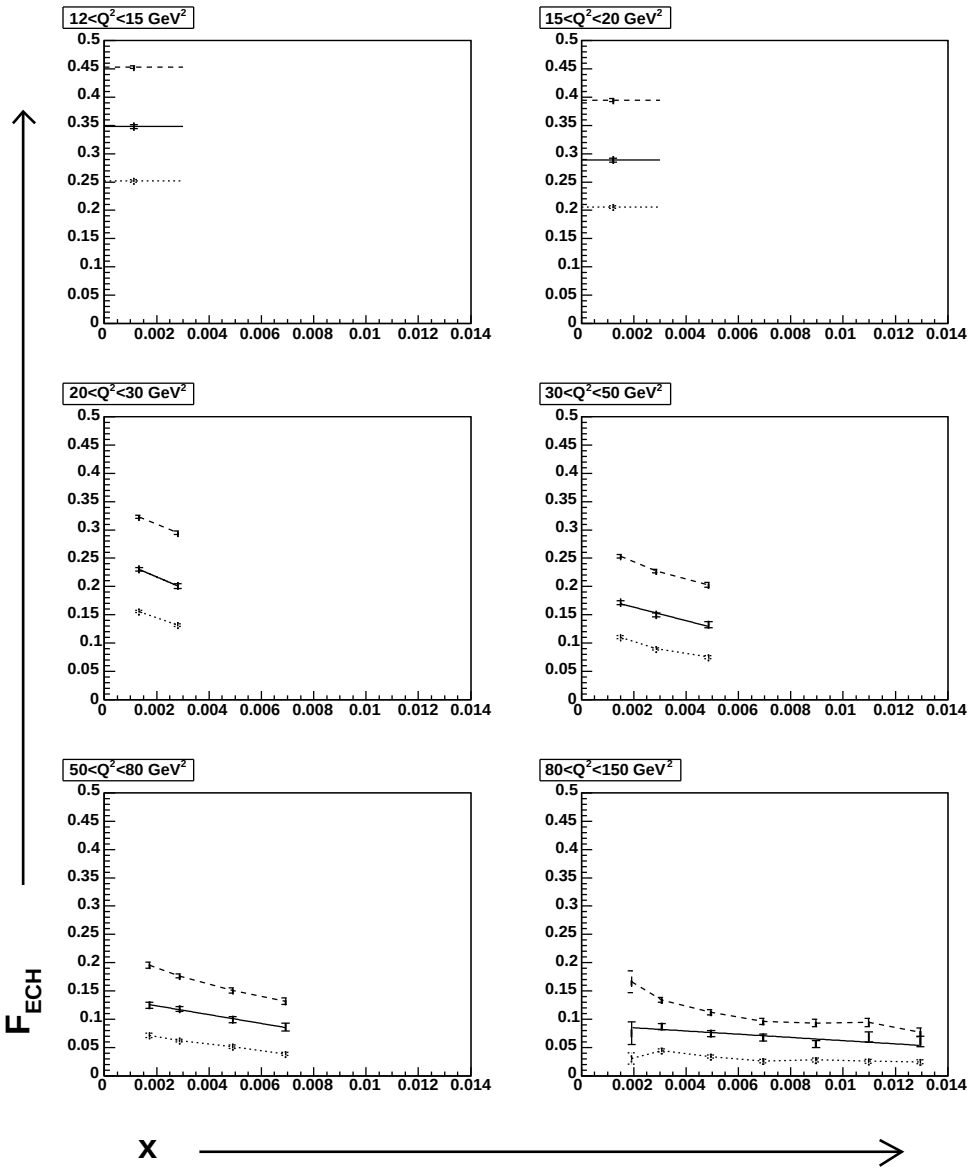

Figure 7.6: Fraction of events with an empty current hemisphere when boosted to the Breit frame of reference, as a function of x_{Bj} for six different Q^2 bins. Shown are the corrected data sample (solid line), and generated Monte Carlo (DJANGOH13, CDM, CTEQ5L) samples with only BGF events (dashed line) and without them (dotted line). (Double angle method).

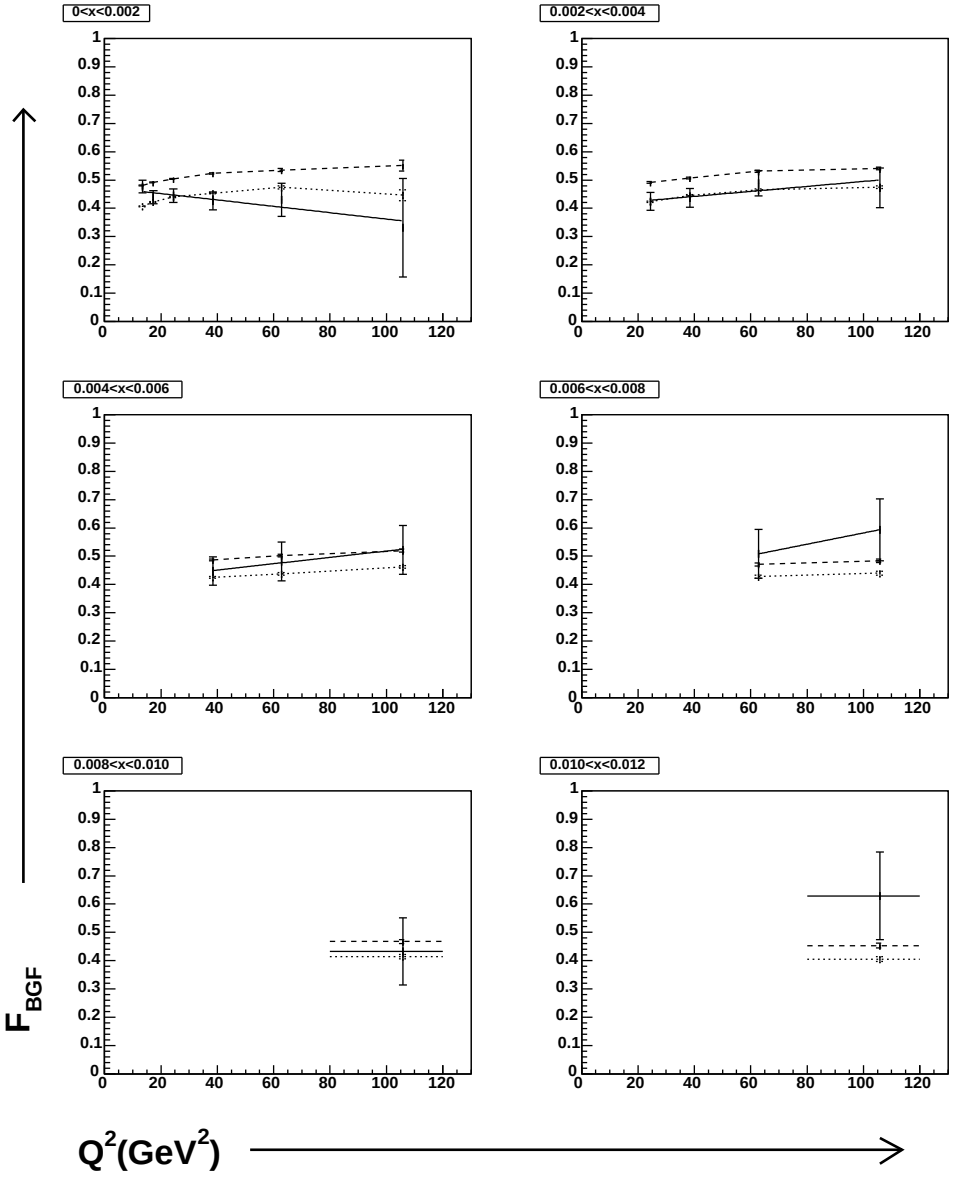

Figure 7.7: Fraction of gluon initiated events (BGF) derived from the fraction of empty current hemisphere events, as a function of Q^2 for six different x_{Bj} bins. Shown are the corrected data sample (solid line), and generated Monte Carlo samples (DJANGOH13, CDM), with two different PDFs: CTEQ5L (dashed line) and MRSG (dotted line). (Double angle method).

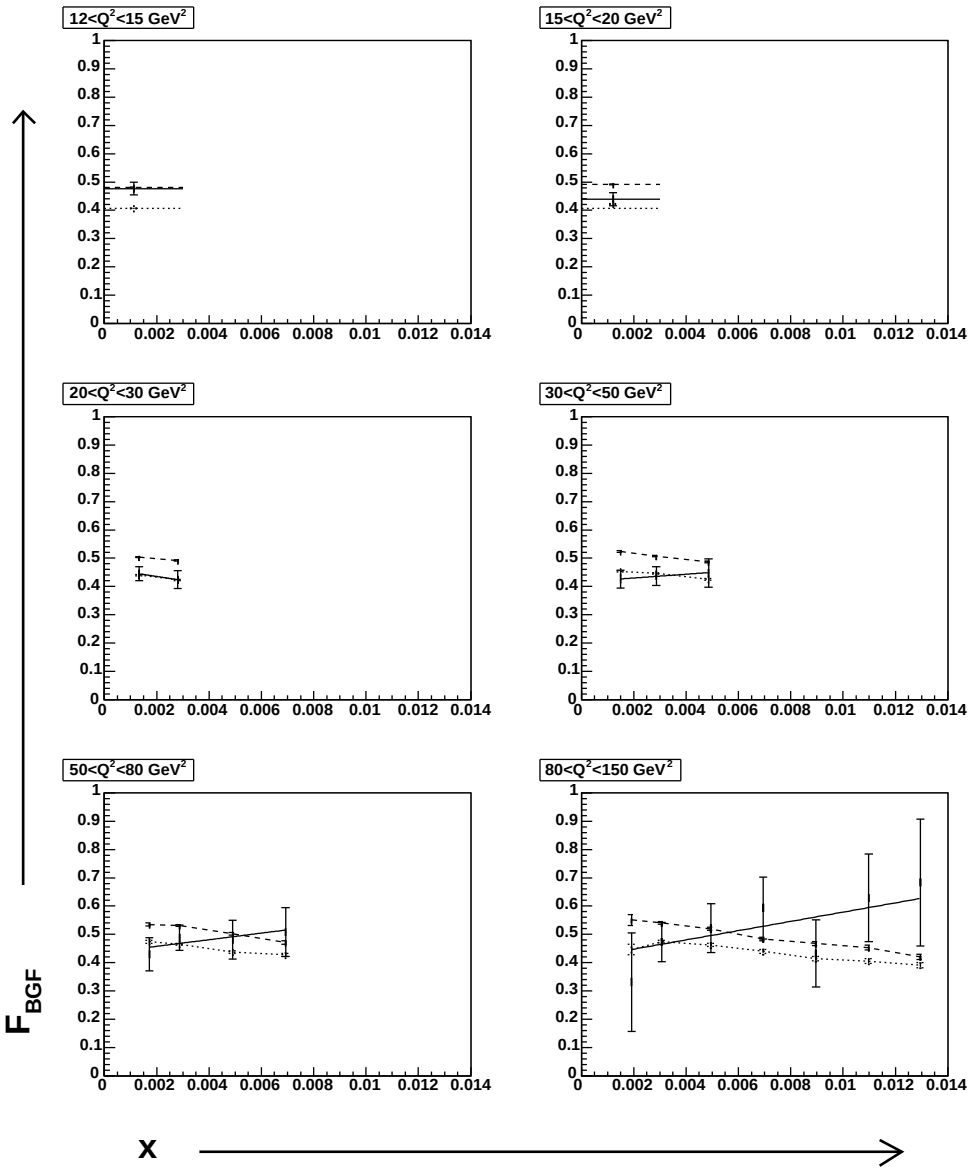

Figure 7.8: Fraction of gluon initiated events (BGF) derived from the fraction of empty current hemisphere events, as a function of x_{Bj} for six different Q^2 bins. Shown are the corrected data sample (solid line), and generated Monte Carlo samples (DJANGOH13, CDM), with two different PDFs: CTEQ5L (dashed line) and MRSG (dotted line). (Double angle method).

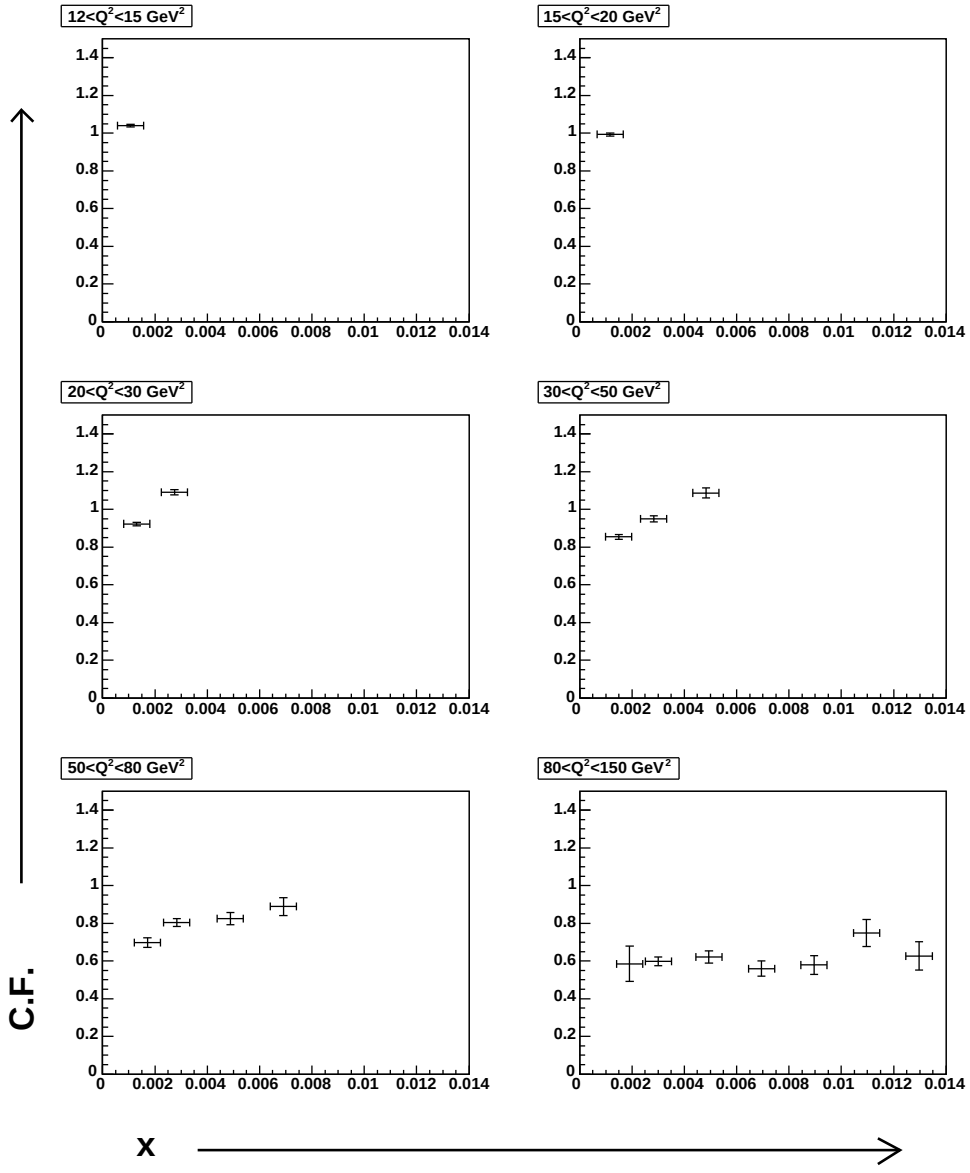

Figure 7.9: Correction factors for the distribution of the fraction of empty current hemisphere events (electron method).

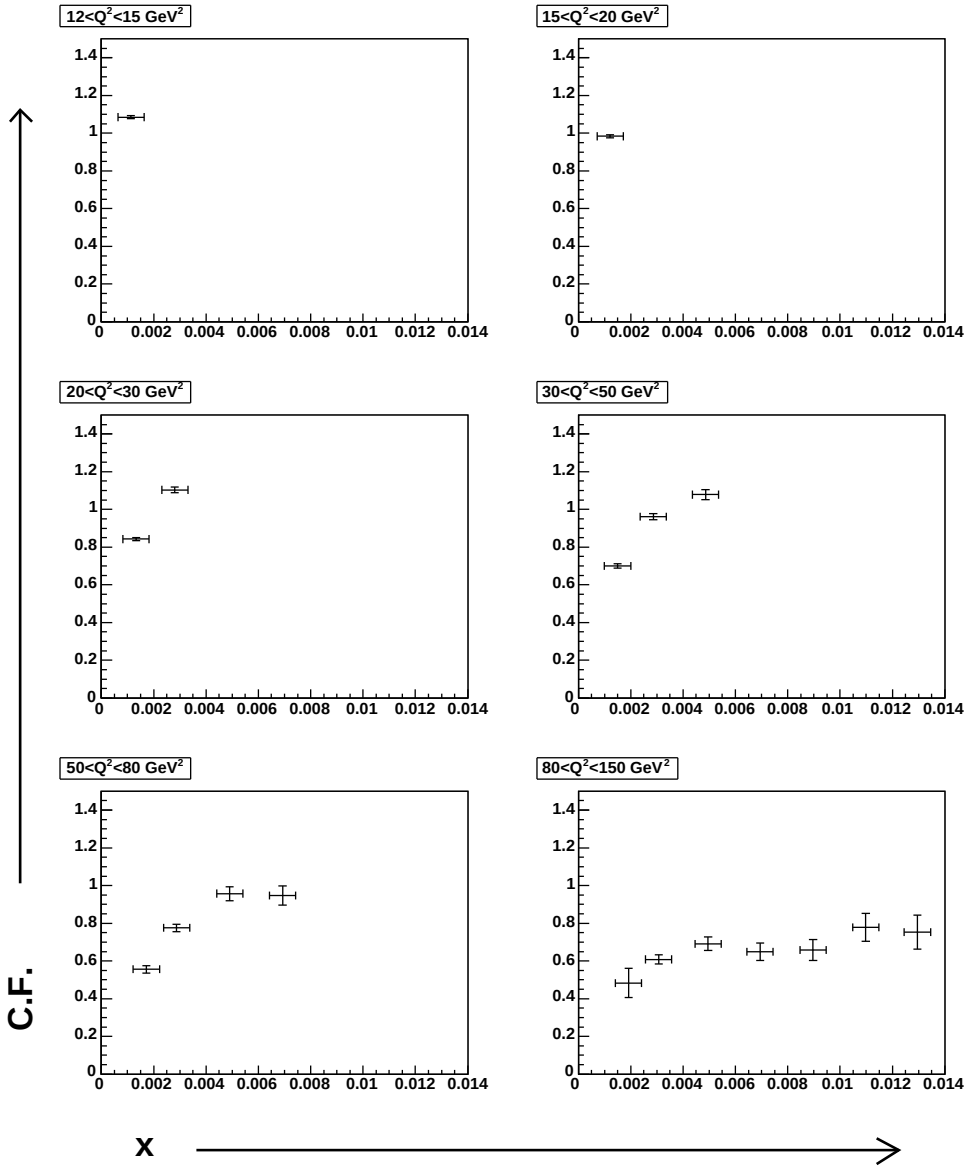

Figure 7.10: Correction factors for the distribution of the fraction of empty current hemisphere events (double angle method).

go from the value of x associated with the struck quark up to 1 (where there are many more quarks than gluons), since this quark could have come from a parent parton carrying arbirarily larger momenta. The fact that the strong coupling is greater in the low Q^2 region is not very significant in this argument, since it leads to an increase in both quark and gluon initiated leading order processes.

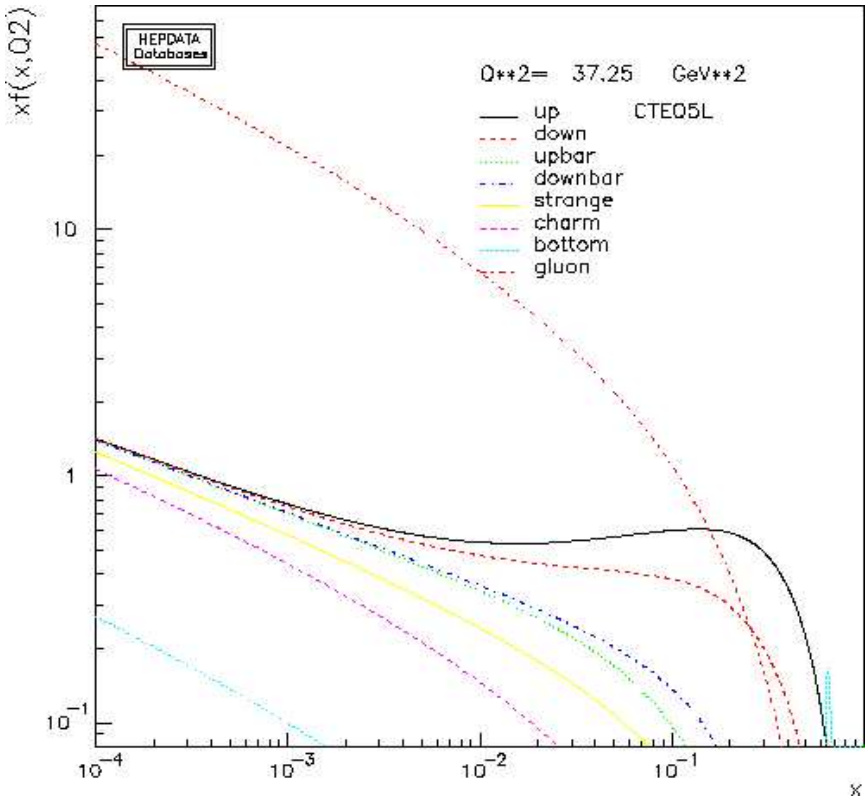

Figure 7.11: The CTEQ5L parton density functions for quarks and gluons.

Due to the large errors in the corrected data sample, the results of the analysis are presented for the central values of the whole sample at $Q^2 = 36.9$ GeV^2 and $x = 0.002$. For the analysis using the electron method, The central value for the fraction of empty current hemisphere events in the

corrected data sample is $(17.0 \pm 0.1(stat) \pm 1.3(syst))\%$ (see section 8.1 for a discussion of systematic uncertainties). The corresponding central values for the gluon and quark samples are $(26.6 \pm 0.1(stat))\%$ and $(10.4 \pm 0.1(stat))\%$ respectively. This gives a value for the fraction of gluon initiated events in the corrected data sample of $41.0 \pm 0.4(stat) \pm 7.9(syst)\%$. The statistical error on the quark sample has been neglected in the numerator of the expression

$$f_{BGF} = \frac{CD - \overline{BGF}}{BGF - \overline{BGF}},$$

since it is much smaller than the error on the data sample. This way the correlation between numerator and denominator is avoided, allowing for the rest of the errors to be added in quadrature.

Percentage of empty current hemisphere events as function Q^2, x.

$Q^2 \rightarrow$ $x \downarrow$	12-15 GeV^2	15-20 GeV^2	20-30 GeV^2	30-50 GeV^2	50-80 GeV^2	80-120 GeV^2
0	$30.9 \pm 0.3 \pm 2.3$	$27.5 \pm 0.3 \pm 2.0$	$24.4 \pm 0.3 \pm 1.6$	$19.7 \pm 0.4 \pm 1.0$	$16.6 \pm 0.7 \pm 1.2$	$14.1 \pm 3.1 \pm 1.2$
to 0.002	$32.1 \pm 0.3 \pm 1.3$	$29.4 \pm 0.3 \pm 1.0$	$27.3 \pm 0.3 \pm 1.2$	$24.5 \pm 0.4 \pm 1.5$	$22.4 \pm 0.7 \pm 2.1$	$15.7 \pm 3.4 \pm 2.3$
0.002			$18.0 \pm 0.4 \pm 2.2$	$15.3 \pm 0.4 \pm 1.5$	$13.7 \pm 0.4 \pm 1.1$	$15.3 \pm 0.7 \pm 1.0$
to 0.004			$18.2 \pm 0.3 \pm 1.0$	$15.6 \pm 0.3 \pm 0.8$	$15.2 \pm 0.4 \pm 0.9$	$14.3 \pm 0.6 \pm 0.9$
0.004				$13.3 \pm 0.5 \pm 1.5$	$11.0 \pm 0.6 \pm 1.7$	$11.9 \pm 0.8 \pm 0.7$
to 0.006				$12.3 \pm 0.4 \pm 0.7$	$10.4 \pm 0.5 \pm 0.8$	$10.8 \pm 0.6 \pm 0.5$
0.006					$8.0 \pm 0.7 \pm 1.5$	$9.6 \pm 0.9 \pm 1.8$
to 0.008					$9.1 \pm 0.5 \pm 1.1$	$10.4 \pm 0.7 \pm 1.3$
0.008						$8.8 \pm 1.0 \pm 1.6$
to 0.010						$8.6 \pm 0.7 \pm 0.6$
0.010						$7.1 \pm 1.1 \pm 1.1$
to 0.012						$8.8 \pm 0.8 \pm 0.9$
0.012						$6.7 \pm 1.2 \pm 2.0$
to 0.014						$8.0 \pm 0.9 \pm 0.7$

Table 7.2: Values for the fraction of empty current hemisphere events (%) for the different analysis bins. Statistical errors are quoted first, followed by the systematic uncertainties. The upper values are derived from the electron method, the lower ones from the double angle method. Generally, the values from the electron method are smaller than those from the double angle method. Also, the systematic errors for the electron method decrease with increasing Q^2, whilst those for the double angle method increase.

Chapter 8

Systematic Uncertainties and Checks

The systematic uncertainties arise from the lack of precise knowledge of some aspects of the detector, namely its calibration and track reconstruction efficiency. These effects are not cancelled when correcting the data, since the same reconstruction software ($H1Rec$ [65], with the same calibration coefficients) is used for real data and Monte Carlo. The *checks* carried out were used to establish the sensitivity of the results on some of the selection cuts and aspects of the models used, even though these effects will be accounted for when correcting the data.

Both the systematic error analysis and checks were carried out in a bin by bin basis. Since the deviations observed were in the same direction for all bins in each test, and since the final results are given for the central values, so are the quoted shifts below.

8.1 Systematic Uncertainties

The systematics were calculated using reconstructed Monte Carlo. The idea is to get the results for the default sample and take them as if they were the data results that would come out had the detector been perfectly calibrated and 100% efficient. Then, "shifted" Monte Carlo samples are produced in which the relevant measured variables have been changed to their upper and lower values. These values are determined from our best knowledge of the detector resolutions and inefficiencies. The difference in the results for the variables under study are then taken as the systematic uncertainty.

This section is divided into two subsections. The first one contains studies about the effect of detector calibration. These studies are particular for each analysis, since different measured quantities are used for kinematic reconstruction in different analyses. The second subsection contains studies about the effect of detector inefficiencies for track reconstruction and the uncertainty introduced by the parton cascade model used. These uncertainties are the same for both analyses.

8.1.1 Calibration Uncertainties

The shifts made to the measured variables are the standard values taken from the database "H1Calculator" [66]. This database is part of the H1 analysis software, and contains the best estimates for the uncertainties. However, the shift in the scattered electron energy has been modified. The reason for this is that the default shift in the H1 Calculator (2%) was used before the SpaCal calorimeter calibration, but since the calibration has been applied to the data presented, the shift has been reduced to 1% (see figure 3.11). The following shifts were observed for the analysis using the electron method for

kinematic reconstruction:

- Scattered Electron Energy: $E_e \pm 1\%$: $f_{ECH} \pm 6.6\%$
- Scattered Electron Polar Angle: $\theta_e \pm 0.3\%$: $f_{ECH} \pm 0.1\%$ (Negligible).
- Scattered Electron Azimuthal Angle: $\phi_e \pm 0.1\%$: Less than 0.1% shift in f_{ECH} (Negligible).

This shows that the most sensitive variable is the energy of the scattered electron, and highlights the importance of the calibration of the SpaCal calorimeter electromagnetic section.

Similarly, for the analysis using the double angle method for kinematic reconstruction:

- Scattered Electron Polar Angle: Same as above.
- Scattered Electron Azimuthal Angle: Same as above.
- Hadronic System Polar Angle: $\gamma \pm 2\%$: $f_{ECH} - 2\%$
- Hadronic System Azimuthal Angle: $\phi_h \pm 2\%$: Less than 0.1% shift in f_{ECH} (Negligible).

8.1.2 Track Efficiency Uncertainties

To estimate the error associated with track digitalisation inefficiencies, tracks were randomly removed in the following way [67]:

- $p_t < 150$ MeV, 7% of tracks removed.

- $150 < p_t < 200$ MeV, 5% of tracks removed.

- $p_t > 200$ MeV, 3% of tracks removed.

A deviation of +3.6% was observed from the default value for the fraction of empty current hemisphere events. Since it is not known if some tracks were added by noise, this error was taken to be symmetric, i.e., $\pm 3.6\%$.

To estimate the error introduced by the parton cascade model, a Monte Carlo sample using the parton shower model, as opposed to the colour dipole model in the default sample, was created. Again, the difference in the results was taken as the systematic error. This difference is less than 0.4%, making the contribution of the parton cascade model small in the final error, since it is calculated by adding all the individual systematics in quadrature.

8.1.3 Summary

The values for the fraction of empty current hemisphere events (f_{ECH}) and for the fraction of gluon initiated events (f_{BGF}), for both analyses, are presented here. Statistical errors are quoted first and systematics second. The total systematic uncertainty in the fraction of empty current hemisphere events was obtained by adding the individual systematics in quadrature.

For the analysis using the electron method for kinematic reconstruction, the final figures are as as follows:

$$f_{ECH} = (17.0 \pm 0.1 \pm 1.3)\%$$

$$f_{BGF} = (41.0 \pm 0.8 \pm 7.9)\%$$

For the analysis using the double angle method for kinematic reconstruction, the final figures are as as follows:

$$f_{ECH} = (18.1 \pm 0.1 \pm 0.7)\%$$

$$f_{BGF} = (47.5 \pm 0.8^{+4.0}_{-4.6})\%.$$

Since the two methods use the same data set (and the systematic errors are in any case dominant), the two results $(41.0 \pm 7.9)\%$, $(47.5 \pm 4.6)\%$ were combined using $1/\delta f^2_{BGF}$ as weights to give a combined method result of

$$f_{BGF} = (45.8 \pm 0.8(stat) \pm 4.0(syst))\%.$$

8.2 Checks

This section is intended to establish the sensitivity of the analysis results to the modelling of the non-perturbative regime of QCD (the Lund string hadronisation model), and also to the low transverse momentum selection that was applied to the data. In other words, the section studies the infra-red safety and the low p_t modelling of the analyses carried out.

8.2.1 Infra-red Safety

In this thesis the charged hadrons picked up in the detector were used to look at effects of partonic level diagrams. In order to establish the effect of hadronisation, a sample of generated events at the parton level was created. The fragmentation process was stopped just after the parton cascade (CDM) modelling the higher orders in the perturbative QCD expansion. Therefore, instead of hadrons the resulting particles in the sample are the quarks and gluons. Note that the analysis at the parton level takes into account both quarks and gluons (charged and neutral partons) when determining the fraction of empty current hemisphere events, whereas in data and Monte Carlo charged hadrons are used as the measurable. The fraction of empty current hemisphere events for these two samples is shown in figure 8.1 as a function of Q^2. At high Q^2, where many particles are produced, the two samples agree well. It is in the low Q^2 region where the hadronisation process has the biggest effect, since, due to the low momentum transfer not many particles can be produced. However, it can be argued that even in this region the hadronisation process does not produce a significant effect. Even if the uncertainty in hadronisation were as high as 10%, the biggest difference in the fraction of empty current hemisphere events in the generated Monte Carlo

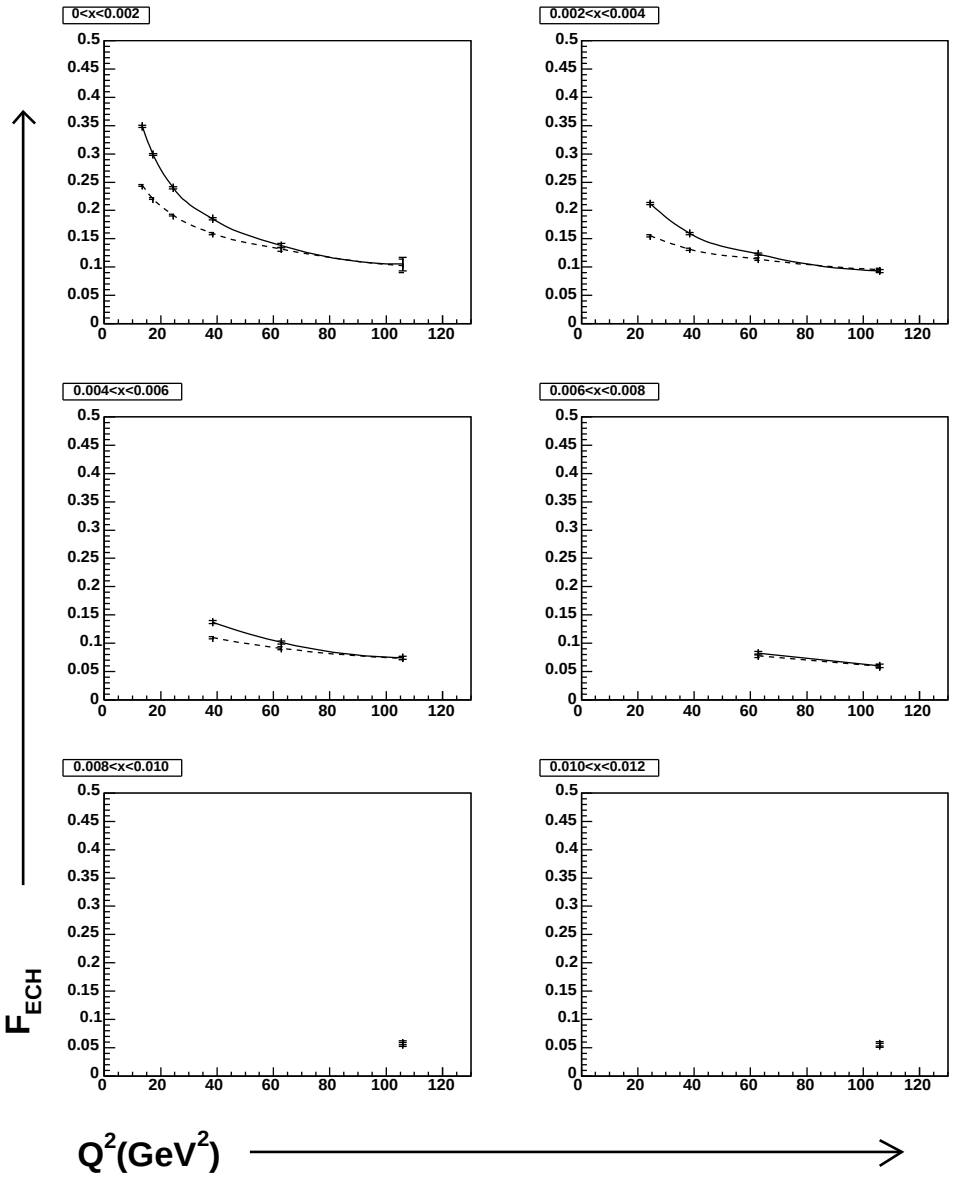

Figure 8.1: Fraction of empty current hemisphere events for the generated Monte Carlo sample at the level of charged hadrons (solid line), and for the generated sample at the partonic level using all partons (dashed line).

sample would be of the order of 1%.

8.2.2 Low p_t Modelling

The minimum transverse momentum of tracks that are accepted in the standard analyses is 120 MeV, and the minimum polar angle is 20^o. These two cuts were extended to 150 MeV and 30^o respectively. After changing these cuts (separately) in the data and reconstructed Monte Carlo, the fraction of empty current hemisphere events in the resulting corrected data sample was found to be less than 0.1% different from that derived from the standard analyses in both cases. Therefore the results are not sensitive to these cuts, or, in other words, the Monte Carlo is reproducing the data results well in the low momentum region.

Chapter 9

Determination of the number of gluons in a proton

The fraction of gluon initiated events presented in chapter 7 was used to try to determine the number of gluons in the proton. This chapter is intended as an additional section to the main body of the thesis. The analysis is heavily based in Monte Carlo predictions and in some significant assumptions, but shows nonetheless a possible use for the results already presented.

9.1 Determining N_g

In this thesis the (theoretical) number gluons in the proton at any given Q^2 and x values is defined as the integral of any given PDF from the desired x value up to 1 (at the desired Q^2 value). The data used for the integration was taken from the Durham database [68]. A testable assumption can be made, in which the number of gluon initiated events is related to the number of gluons N_g by some function a ($N_{BGF} = a(x, Q^2) \times N_g$) which will vary

kinematically. This is a reasonable assumption, since for BGF the integral in leading order QCD is over the gluon PDF multiplied by slowly varying kinematic factors (see equation 2.24).

The same assumption can be made for the relation between the number of quark initiated events (QPM + CQCD) and the number of quarks N_q ($N_{\overline{BGF}} = b(x, Q^2) \times N_q$). This is less obvious than the gluon case since, in the integral for CQCD, the various quark species have different contributions by charge and the QPM term does not contain an integral but only the term $xf_q(x, Q^2)$ summed over the active flavors. However, the QPM term is related to the integrand, so it is worth testing the assumption. Again the number of quarks is determined by integration of the PDFs.

If the above assumptions are correct, the fraction of BGF events can be written as

$$f_{BGF} = \frac{N_{BGF}}{N_{BGF} + N_{\overline{BGF}}} = \frac{a(x, Q^2)N_g}{a(x, Q^2)N_g + b(x, Q^2)N_q} \tag{9.1}$$

or,

$$f_{BGF} = \frac{N_g}{N_g + \tau(x, Q^2)N_q} \tag{9.2}$$

where $\tau = b/a$ is some kinematic function independent of PDFs. The test for these assumptions is to evaluate τ at different phase-space regions for values of f_{BGF} derived from the same Monte Carlo program, but using different PDFs (with the corresponding values for the number of gluons and the number of quarks). The values for the τ function are shown in table 9.1 and plotted in figure 9.1 for the PDFs CTEQ5L and MRSG. The filled boxes correspond to some of the Q^2/x bins chosen for the analysis. The empty

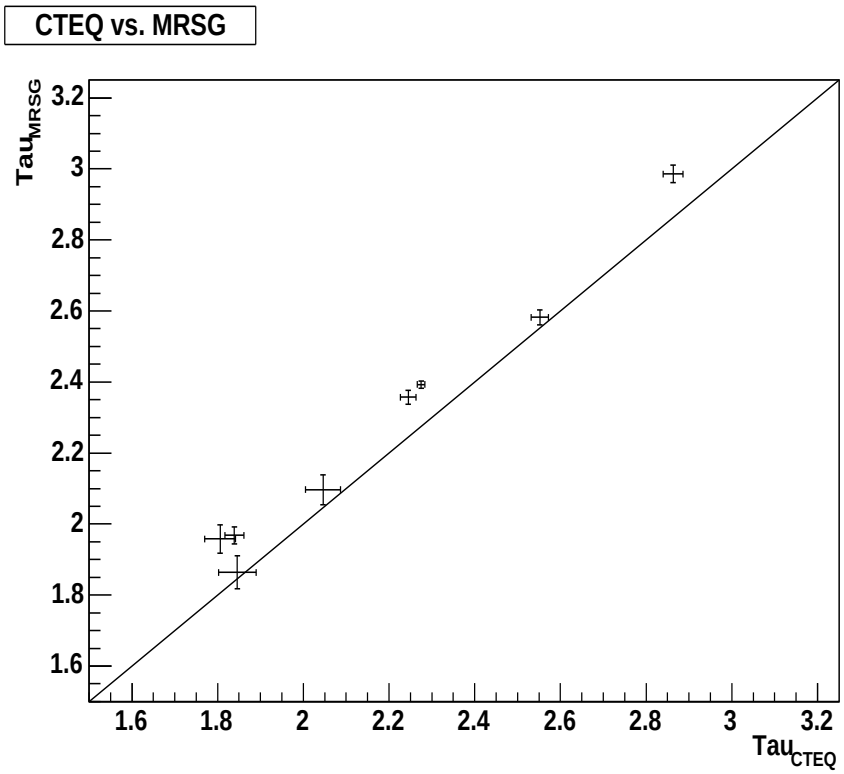

Figure 9.1: Comparison of the values of the τ functions resulting from CTEQ5L and MRSG, for different phase space regions. A 45^{o} line is displayed showing where the points should lie in order for the τ function to be fully independent of the PDF.

boxes (bins) are not kinematically accessible with the presented data. The values at $Q^2 = 35.7$ GeV^2 and $x = 0.0022$ are calculated with full statistics, since these are the mean values for the Monte Carlo event samples. This shows that τ is approximately a universal function. The τ values coming from the two PDFs are close together, but the values from MRSG are always greater than those from CTEQ5L, which means that there is also a small PDF dependence. This dependence is allowed for by introducing an extra systematic error, which will be discussed after equation 9.3 is presented.

$x \downarrow$; $Q^2(GeV^2) \rightarrow$	13.42	24.48	35.7	62.90
0.0011	2.86 ± 0.02 2.99 ± 0.02			
0.0013		2.55 ± 0.02 2.58 ± 0.02		
0.0017				2.05 ± 0.04 2.10 ± 0.04
0.0022			2.28 ± 0.01 2.39 ± 0.01	
0.0028		2.25 ± 0.02 2.36 ± 0.02		
0.0029				1.84 ± 0.02 1.97 ± 0.02
0.0049				1.81 ± 0.04 1.96 ± 0.04
0.0069				1.85 ± 0.04 1.86 ± 0.05

Table 9.1: Values of the τ function for CTEQ5L and MRSG parton density functions for different Q^2/x bins. In each box the CTEQ5L value is displayed first with the MRSG value below it. The errors quoted are statistical only.

Once the τ function has been determined from the Monte Carlo it can be used with the (better known) predicted number of quarks and the experimentally determined fraction of gluon initiated events to determine the number of gluons, as defined above, in the data sample.

Rearranging eq 9.2 one obtains:

$$N_g = N_q \tau(x, Q^2) \frac{f_{BGF}}{1 - f_{BGF}}. \tag{9.3}$$

This gives a central value of

$$N_g = 23.3 \pm 0.4(stat) \pm 2.0(syst) \pm 1.2(PDF).$$

where the value for f_{BGF} taken is the combined result from the two analyses quoted in section 8.1.3. The value for $N_q\tau(x, Q^2)$ was taken to be the mean of $(N_q\tau(x, Q^2))_{CTEQ}$ and $(N_q\tau(x, Q^2))_{MRSG}$. The PDF systematic uncertainty, mentioned earlier, is taken to be half the difference between these two values.

Chapter 10

Conclusions

An innovative method has been presented which uses event topologies in the Breit frame of reference to constrain the gluon density functions. From there, an estimation of the number of gluons in the proton, as defined in the text, and in the region of phase-space analysed could be performed. Due to the large systematic uncertainties to which the analysis was subject, the constraint provided cannot be considered as definitive or very powerful. However, from the two parton density functions investigated, the fraction of gluon initiated events found in the corrected data sample appears to favour MRSG over CTEQ5L. These two PDF display a considerable difference in the prediction for the number of gluons in the proton (see figure 6.16), again, as defined in the presented work. Although the determined value for the number of gluons favours MRSG, at this stage the errors were so large that the final result is in agreement with all six of the PDFs presented in figure 6.16. One interesting remark is that this value is closest to, and almost on top of, the parton density function from the H1 experiment (H12000).

Another point that should be noted is that in the Monte Carlo programs

used, the matrix element was calculated only up to leading order QCD. It could be argued however, that performing next to leading order calculations would not yield results very different to the ones presented here, since the probability of further "hard process" splittings decreases with increasing order.

Thus, this thesis most importantly should be taken as an illustration of a novel technique, rather than as an accurate determination of the number of gluons in the proton or as a serious constrain to the PDFs. Future analyses with more modern detectors and performing higher order calculations may some day use the method for these purposes.

Acknowledgements

First and foremost I would like to thank my supervisor, Prof. Graham Thompson, for all the help and time he has given me, and for encouraging me all the way to the end. I feel that with me particularly he has been very patient and has gone way beyond the call of duty. For this, some day I will build a monument in his honour (this is a Spanish expression, meaning I am very grateful).

Second but not least, I thank my mother Carmen and wife Elena, to whom this thesis I dedicate. To Carmen for putting up with all my difficult teenage years and also for fleeing Spain for the sake of her children. To Elena for supporting me emotionally and having to put up with all my stressful moments, since I know it must have been very hard (sorry darling). Also for supporting me financially when my grant was over by working in something she does not like at all (crappy Top-Shop). Two more monuments on the way then!

Special thanks go also to Dan Traynor from QMUL, who showed me absolutely everything I needed to produce my analysis computing-wise, and who helped me with some of the physics as well. Cheers Dan.

From the people I met in DESY, thanks to Paul Laycock for his encouragement on difficult times, to Ewelina Lobodzinska for her help with the SpaCal calibration, and to Eram Rizvi for answering many questions.

From London, I would like to thank Melisa Carames and Manoly Gumbau for giving me political asylum in difficult times when I was homeless. Had it not been for them I would have had to sleep in some abandoned tube station in the last stages of my Ph.D. Thank you M's!

From home, thanks to my sister Christel and to my friends (Juanito the Banana, Nacho the Rufa, Coque the Apricot, Jaime the Missile-Head, Jorge the Cave-Man, Jon the Terrorist, Javi the Pilot and Cesar the Coconut) for all of the good years and *fiestas* before I came to London.

Finally, I would like to thank PPARC for their financial support they have given me for three years.

Bibliography

[1] D. Kant. QCD Studies in the Breit Frame at HERA. *Nucl. Phys.* **B71** (1997) 31.

[2] D. Kant, Ph.D. thesis, A Study of the Fragmentation of Quarks in $e^{-}p$ Collisions at HERA using the H1 Detector. (1996).

[3] G. D. Lafferty et al., A Compilation of Inclusive Particle Production Data in $e^{+}e^{-}$ Annihilation. *J. Phys. G: Nucl. Part. Phys.* **21** (1995) A1-A151.

[4] R. P. Feynman. QED: The strange theory of light and matter. Princeton University Press. (1986).

[5] C. Adloff et. al., H1 Collaboration. Measurement of the Inclusive DIS Cross Section at Low Q^2 and High x using Events with Initial State Radiation. **ICHEP04**, Beijing. (2004).

[6] F. Halzen and A.D. Martin. Quarks & Leptons: An Introductory Course in Modern Particle Physics. John Wiley & Sons. New York. (1984).

[7] D. H. Perkins. Introduction to High Energy Physics. Addison-Wesley Publishing co., London. (1987).

[8] G. D. Coughlan and J.E. Dodd., The Ideas of Particle Physics, Cambridge U.P., 117.

[9] R. P. Feynman. Very High-Energy Collisions of Hadrons. *Phys. Rev. Lett.* **23** (1969) 1415-1417.

[10] M. Bloom et al., M. Breidenbach et al., *Phys. Rev. Lett.* **23** (1969) 935.

[11] W Marciano, H Pagels. Quantum Chromodynamics. Elsevier. *Phys. Rep.* **36** (1978) 137-276.

[12] G. Sterman et al., Handbook of perturbative QCD 28. (2000).

[13] W. A. Bardeen et al, Deep Inelastic Scattering beyond the Leading Order in Asymptotically Free Gauge Theories. *Phys. Rev.* **D18** (1978) 3998.

[14] A. D. Martin et al., *J. Phys. G: Nucl. Part. Phys.* **19** (1993) 1425-1427.

[15] A. Dubak, Ph.D. thesis, Measurement of the e^+p Neutral Current DIS Cross Section and the F_2, F_L, xF_3 Structure Functions in the H1 Experiment at HERA 112. (2003).

[16] C. Adloff et. al., H1 Collaboration. Deep-Inelastic Inclusive ep Scattering at Low x and a Determination of α_s. *Eur. Phys. J.* **C21** (2001) 33.

[17] A. C. Benvenuti et. al., BCDMS Collaboration, A High Statistics Measurement of the Proton Structure Functions $F_2(x, Q^2)$ and R from Deep Inelastic Muon Scattering at High Q^2. *Phys. Lett.* **B223** (1989) 485.

[18] M. Arneodo et. al., MNC Collaboration, Measurement of the Proton and the Deuteron Structure Functions F_2^p and F_2^d. *Phys. Lett.* **B364** (1995) 107-115.

[19] T. Ahmed et al., H1 Collaboration. *Phys. Rev. Lett.* **439** (1995) 471.

[20] I. Abt et al. H1 Collaboration. *Phys. Rev. Lett.* **407** (1993) 515.

[21] H. L. Lai et al., Global QCD Analysis of Parton Structure of the Nucleon: CTEQ5 Parton Distributions. CTEQ Collaboration. *Eur. Phys. J.* **C12** (2000) 375.

[22] A. D. Martin, W. J. Stirling and R. G. Roberts. MRS Parton Distributions. *RAL-93-077.* (1993).

[23] A. Kwiatkowski *Compt. Phys. Commun.* **69** (1992) 155.

[24] G. Ingelman. *Compt. Phys. Commun.* **101** (1997) 108.

[25] T. Sjostrand. *Compt. Phys. Commun.* **82** (1994) 74.

[26] L. Lonnblad. *Compt. Phys. Commun.* **71** (1992) 35.

[27] W. Buchmuller and G. Ingelman. Monte Carlo Generators. Workshop on Physics at HERA, Vol. 3. DESY. (1991).

[28] G. Grindhammer et al., Monte Carlo Generators for HERA Physics. DESY-PROC-1999-02. (1998-1999).

[29] G. Gustafson and U. Pettersson. *Nucl. Phys.* **B306** (1988) 746.

[30] L. Lonnblad. *Compt. Phys. Commun.* **71** (1992) 15.

[31] G. Altarelli and G. Parisi. *Nucl. Phys.* **126** (1977) 297.

[32] T. Sjostrand and M. Bengtsson. *Compt. Phys. Commun.* **43** (1987) 367.

[33] I. Abt et al., H1 Collaboration. *Nucl. Instr. Meth.* **A386** (1997) 310.

[34] H. Bethe and W. Heitler. On the Stopping of Fast Particles and on the Creation of Positive Electrons. *Proc. Roy. Soc. Lond.* **A146** (1934) 83.

[35] C. Wissing, A. Beglarian, P. Biddulph, M. Fleischer, The H1 ToF System in 1996 and 1997. Internal Report, H1-IN-533. (1998).

[36] C. Adloff et. al., H1 Collaboration. Luminosity Measurement in the H1 Experiment at HERA. **ICHEP96**, Warsaw. (1996).

[37] B.Reisert. Electron Proton Scattering at High Momentum Transfers at the H1 Experiment at HERA. MPI-PHE-200-26.

[38] C.Beigbeder. Level2 Topological Trigger (L2TT) Hardware. H1-Note H1-07/98-547. (1998), DESY.

[39] J. K. Köhne et al. Realisation of a second level neural network trigger for the H1 experiment at HERA. *Nucl. Instr. Meth.* **A389** (1997) 128-133.

[40] M. Kausch-Blecken v. Schmeling, Ph.D. thesis, The Silicon Microvertex Detector of the H1 Experiment: Readout, Event Reconstruction and Studies on Heavy Quark Decays. (1998).

[41] W. Eick et al., *Nucl. Instr. Meth.* **A386** (1997) 81.

[42] J. Burger et al., *Nucl. Instr. Meth.* **A279** (1989) 217.

[43] H. Drumm et al., *Nucl. Instr. Meth.* **176** (1980) 333.

[44] I. Abt et al., H1 Collaboration. *Nucl. Instr. Meth.* **A386** (1997)348.

[45] B. Andrieu et al. (H1 Calorimeter Group), The H1 Liquid Argon Calorimeter System. *Nucl. Instr. Meth.* **A336** (1993) 460.

[46] R. D. Appuhn et al. (H1 SPACAL Group), The H1 Lead/Scintillating Fibre Calorimeter. *Nucl. Instr. Meth.* **A386** (1997) 397.

[47] W. Buchmuller and G. Ingelman. Proceedings of the Workshop "Physics at HERA", Vol. 1. DESY. (1992).

[48] U. Bassler and G. Bernardi. On the Kinematic Reconstruction of Deep Inelastic Scattering at HERA. DESY pre-print 94-231. (1994).

[49] M. Dirkmann, Internal Note. H1-05/96-477. (1996).

[50] C. Arndt, Ph.D. Thesis.,DESY (1995).

[51] J. Janoth et al., Internal Note. H1-11/95-464. (1995).

[52] J. Katzy. Ph.D. Thesis. Heidelberg. DESY. (1997).

[53] I. Abt et al. H1 Collaboration. *Phys. Rev. Lett.* **328** (1994) 176.

[54] W. von Schlippe. Kinematics of Deep Inelastic Scattering in the HERA Lab Frame. Internal Report. (1992).

[55] J. Meyer. H1 Collaboration. Guide to Simulation Program H1Sim. **1** (1991) 3.

[56] R. Brun et al., GEANT3. CERN-DD/EE/84-1. (1987).

[57] Matti Peez, Benjamin Portheault and Emmanuel Sauvan. An Energy Flow Algorithm for Hadronic Reconstruction in OO: Hadroo2. H1 Internal Note. H1-01/05-616.

[58] C. Adloff et. al., H1 Collaboration. Evolution of *ep* Fragmentation and Multiplicity Distributions in the Breit Frame. *Nucl. Phys.* **B504** (1997).

[59] G. Thompson et. al., *Jet Finding in the Breit Frame, J. Phys.* **G19** (1993) 1575.

[60] D. Traynor. Private communication. Not published.

[61] I. Abt et al., H1 Collaboration, Inclusive Charged Particle Cross Sections in Photoproduction at HERA, *Phys. Lett.* **B328** (1994) 176.

[62] C. Adloff et. al., Evolution of *ep* Fragmentation and Multiplicity Distributions in the Breit Frame. DESY 97-108.(1997).

[63] Martin Hampel, Ph.D. Thesis. Measurement of the Gluon Density from Jet Rates in Deep Inelastic Scattering. DESY.(1997).

[64] David Muller, Ph.D. Thesis. A Measurement of the Gluon Density in the Proton Based on Charm Production at HERA. DESY. (1998).

[65] G. Bernardi et al., Guide to Simulation Program H1Sim. H1 Document. (1995).

[66] H1 Calculator. H1 Fast Navigator, Computing and Software. (*http* : *//www − h1.desy.de/h1/www/general/home/intra_home.html*).

[67] K. Daum. Recent News from the CJC Simulation. Presentation in HFS Working Group Meeting. DESY.(2003).

[68] Durham Database. On-line Parton Distribution Calculator with Graphical Display (*www − spires.dur.ac.uk/hepdata/pdf3.html*).